

November 2017

Spectroscopic Studies of Gas-Phase Transition Metal Complexes of Cations and Cluster Ions with Methane and Water

Christopher Copeland
University of Massachusetts Amherst

Follow this and additional works at: https://scholarworks.umass.edu/dissertations_2

 Part of the [Physical Chemistry Commons](#)

Recommended Citation

Copeland, Christopher, "Spectroscopic Studies of Gas-Phase Transition Metal Complexes of Cations and Cluster Ions with Methane and Water" (2017). *Doctoral Dissertations*. 1058.
https://scholarworks.umass.edu/dissertations_2/1058

This Open Access Dissertation is brought to you for free and open access by the Dissertations and Theses at ScholarWorks@UMass Amherst. It has been accepted for inclusion in Doctoral Dissertations by an authorized administrator of ScholarWorks@UMass Amherst. For more information, please contact scholarworks@library.umass.edu.

Spectroscopic Studies of Gas-Phase Transition Metal Complexes
of Cations and Cluster Ions with Methane and Water

A Dissertation Presented

by

CHRISTOPHER W. COPELAND

Submitted to the Graduate School of the
University of Massachusetts Amherst in partial fulfillment
of the requirements for the degree of

DOCTOR OF PHILOSOPHY

SEPTEMBER 2017

Department of Chemistry

© Copyright by Christopher W. Copeland 2017

All Rights Reserved

**Spectroscopic Studies of Gas-Phase Transition Metal Complexes
of Cations and Cluster Ions with Methane and Water**

A Dissertation Presented

by

CHRISTOPHER W. COPELAND

Approved as to style and content by:

Ricardo B. Metz, Chair

Bret E. Jackson, Member

Michael D. Barnes, Member

David M. Kawall, Member

Richard W. Vachet, Department Head
Department of Chemistry

DEDICATION

To my parents for all their love and support

ACKNOWLEDGMENTS

I would first like to express my most sincere heartfelt thanks to Dr. Ricardo Metz. Without his unending support in and outside of lab I would certainly not be here. I feel truly blessed to have had such an incredibly involved and kind advisor. From teaching me about programming, machining, electronics, optics, and spectroscopy, to even helping me figure out what was wrong with my car, his knowledge and willingness to help his students as well as everyone around him is seemingly endless and truly something to aspire to.

I would like to thank all the members of the Metz group for always keeping the atmosphere in lab lively and full of discussions that went far beyond chemistry and taught me many lessons about life over the years. I would specifically like to thank Affawn, whose endless drive to challenge not only others' beliefs but his own beliefs as well, has had a strong impact on me and my way of thinking over the years. I would like to thank Lee Pearson, for being a true mentor to me at the beginning of my time here, and for guiding me through the great early works of science fiction. I would like to thank Dave for being a great friend, tennis partner, for keeping the lab full of laughter, and for always being willing to eat the spiciest of foods with me.

I would also like to thank all my friends over the years here from inside and outside of the chemistry department, for making my time here truly enjoyable, and making me a part of a fantastic community of not just colleagues but friends.

Finally, I would like to express my gratitude to my parents and family for their endless love and support. Their help and encouragement has been a true blessing to me during my time at UMass Amherst.

ABSTRACT

SPECTROSCOPIC STUDIES OF GAS-PHASE TRANSITION METAL COMPLEXES OF CATION AND CLUSTER IONS WITH METHANE AND WATER

SEPTEMBER 2017

CHRISTOPHER COPELAND, B.S. SIENA COLLEGE

Ph.D., UNIVERSITY OF MASSACHUSETTS AMHERST

Directed by: Professor Ricardo B. Metz

The study of the non-covalent interactions between metals ions and ligands such as water and methane are key to understanding many processes including solvation, homogeneous catalysis and metals in biology. Similarly, the study of interactions between transition metal ions and cluster ions with hydrocarbons is of great importance in the understanding of C-H activation reactions which are involved in generation of fuels. Gas-phase metal complexes are good models for understanding the intrinsic interactions between the metal and the ligand. Understanding the mechanisms behind these interactions can be done by characterizing the structure and bonding in the molecular reactants, products, and intermediates. This characterization is made possible by combining experimental spectroscopy with computational studies to provide insight into molecular geometries and binding characteristics of ions. In this work, we explore two non-covalent interactions involved in solvation and catalysis by studying entrance-channel complexes of the reactions of transition metal ions with water and methane respectively.

The motivations, techniques, apparatus, data acquisition and analysis methods are discussed in Chapters 1 and 2. Chapter 3 discusses the electronic spectroscopy of the 7B_1 and 7B_2 excited states of $Mn^+(H_2O)$ and $Mn^+(D_2O)$ measured using photodissociation spectroscopy. Progressions in the Mn^+-H_2O stretch are observed in both excited states, with the in-plane-bend also observed in the first excited state

of $\text{Mn}^+(\text{H}_2\text{O})$, and the out-of-plane bend observed in the second excited state of both $\text{Mn}^+(\text{H}_2\text{O})$ and $\text{Mn}^+(\text{D}_2\text{O})$. Partially resolved rotational structure in the first excited state is analyzed.

Chapter 4 discusses the vibrational spectroscopy of $\text{Fe}_x^+(\text{CH}_4)_n$. Vibrational spectra are measured for $\text{Fe}_2^+(\text{CH}_4)_n$ ($n=1-3$), $\text{Fe}_3^+(\text{CH}_4)_n$ ($n=1-3$), and $\text{Fe}_4^+(\text{CH}_4)_4$ in the C-H stretching region ($2650-3100\text{ cm}^{-1}$) using photofragment spectroscopy, monitoring loss of CH_4 . All spectra are dominated by an intense peak around 2800 cm^{-1} , due to the symmetric C-H stretch. Density functional theory calculations are used to identify possible structures and geometries and to predict the spectra.

Chapter 5 identifies possible extensions of the Chapter 3 and 4 studies to new first, second, and third-row transition metal-water and metal-methane complexes, as well as complexes of metal cluster ions with water and methane. Lastly, Chapter 5 describes alterations to the instrument.

TABLE OF CONTENTS

	Page
ACKNOWLEDGMENTS	v
ABSTRACT.....	vi
LIST OF TABLES	xi
LIST OF FIGURES	xii
CHAPTER	
1. INTRODUCTION	1
1.1 Introduction	1
1.2 Motivation	1
1.3 Photfragment Spectroscopy	4
2. EXPERIMENTAL	9
2.1 Instrument Overview.....	9
2.1.1 Laser Systems	13
2.1.1.1 Nd:YAG Lasers	16
2.1.1.2 ND6000 Dye Laser	16
2.1.1.3 Laservision IR OPO/OPA	17
2.1.2 Time of Flight and Timing	19
2.2 Data Acquisition	24
2.2.1 Digital Scope.....	25
2.2.2 Breakout Box Dye Laser.....	25
2.2.3 Breakout Box IR Laser.....	26
2.2.4 Data Analysis	26
2.3 Experimental Techniques.....	27
2.3.1 Mass Spectra and Difference Spectra	27
2.3.2 Electronic Photodissociation Spectroscopy	28
2.3.3 Vibrational Spectroscopy	28

	2.3.3.1 IR Single Photon Dissociation (IRPD)	30
	2.3.3.2 IR Multiple Photon Dissociation (IRMPD)	30
	2.3.4 Argon Tagging	31
	2.3.5 Vibrationally Mediated Photodissociation (VMP).....	32
3	NEAR ULTRAVIOLET PHOTODISSOCIATION SPECTROSCOPY OF $Mn^+(H_2O)$ AND $Mn^+(D_2O)$	37
	3.1 Introduction	37
	3.2 Experimental Methods	39
	3.3 Results and Discussion.....	41
	3.3.1 Electronic Spectroscopy.....	41
	3.3.2 Electronic Spectroscopy: Rotations	53
	3.3.3 Vibrational Spectroscopy	60
	3.3.4 Summary and Conclusions.....	62
4.	VIBRATIONAL SPECTROSCOPY OF IRON-METHANE CLUSTERS	67
	4.1 Introduction	67
	4.2 Experimental and Computational Methods.....	68
	4.3 Results and Discussion.....	70
	4.3.1 Calculation Discussion	74
	4.3.1 $Fe_2^+(CH_4)$	77
	4.3.2 $Fe_2^+(CH_4)_2$	79
	4.3.3 $Fe_2^+(CH_4)_3$	82
	4.3.4 $Fe_3^+(CH_4)$	84
	4.3.5 $Fe_3^+(CH_4)_2$	86
	4.3.6 $Fe_3^+(CH_4)_3$	86
	4.3.7 $Fe_4^+(CH_4)_4$	90
	4.4 Summary and Conclusions.....	93
5.	EXTENSIONS AND FUTURE WORK.....	97
	5.1 $M^+(H_2O)$ Systems.....	97
	5.1.1 First-Row Transition Metal-Water Complexes.....	97
	5.1.2 Second-Row and Third-Row Transition Metal-Water Complexes.....	97
	5.1.3 Metal-Water Clusters	98

5.2 $M^+(\text{CH}_4)$	98
5.2.1 $M_x^+(\text{CH}_4)_n$ Clusters	98
5.2.2 First-Row Metal Methane Complexes	99
5.2.3 Second-Row and Third-Row Metal Methane Complexes	99
5.2.4 First-Row Metal-Alkane Complexes	100
5.2.5 Metal Methane Ar Tagging	99
5.3 TOFMS Instrument Modifications	100
5.3.1 Second Mass Gate Introduction	101
5.3.2 Modular Nozzle Assembly and Other Adjustments	105
 APPENDICES	
A. LOWEST ENERGY GEOMETRIES, ENERGIES, VIBRATIONAL FREQUENCIES AND INTENSITIES CALCULATED AT THE M11L/6-311++G(3df,3pd) LEVEL	108
B. COMPARISON OF B3LYP SIMULATIONS WITH AND WITHOUT EMPRICAL DISPERSION FOR MONOLAYER COMPLEXES CALCULATED AT THE M11L/6-311++G(3df,3pd) LEVEL	119
 BIBLIOGRPAHY	 122

LIST OF TABLES

Table		Page
3-1	Calculated and measured vibrational frequencies (cm^{-1}) of $\text{Mn}^+(\text{H}_2\text{O})$ and $\text{Mn}^+(\text{D}_2\text{O})$	47
3-2	Geometries of the ground and excited states of $\text{Mn}^+(\text{H}_2\text{O})$	50
3-3	Rotational Constants for $\text{Mn}^+(\text{H}_2\text{O})$ (cm^{-1}).....	57
4-1	C-H bond dissociation energy (cm^{-1}) of $\text{Fe}_x^+(\text{CH}_4)_n$ clusters calculated with B3LYP, BPW91 and M11L functionals with the 6-311++G(3df,3pd) basis set	75
4-2	Partial Charges on Iron and Methane in Monolayer Complexes (+1 total).....	76
4-3	Experimental and calculated lowest C-H stretching frequencies of $\text{Fe}_2^+(\text{CH}_4)_n$ ($n=1-3$), $\text{Fe}_3^+(\text{CH}_4)_n$ ($n=1-3$) and $\text{Fe}_4^+(\text{CH}_4)_n$ ($n=1-4$)	87

LIST OF FIGURES

Figure	Page
1.1 An Illustration of the photofragmentation process.....	6
2.1 Schematic view of dual time-of-flight reflectron mass spectrometer	14
2.2 Aluminum nozzles and secondary valve holder used in the source region to facilitate cluster formation	15
2.3 Experimental (blue) and simulated (red) HITRAN absorption spectra of methane.	20
2.4 Time delay flowchart for instrument.....	22
2.5 Difference spectrum of $\text{Cu}^+(\text{CH}_4)_4$ with IR laser at 2767 cm^{-1}	29
2.6 Illustration of techniques used in vibrational spectroscopy a) Infrared Predissociation b) Infrared Multiple Photon Dissociation (IRMPD)	34
2.7 Illustration of the depletion double resonance technique, where the UV laser is parked (blue arrow) and the IR laser is scanned (red arrow).....	35
3.1 Photodissociation spectra of $\text{Mn}^+(\text{H}_2\text{O})$ and $\text{Mn}^+(\text{D}_2\text{O})$ from 30,000 to $35,000\text{ cm}^{-1}$	42
3.2 Rotational axis diagram of $\text{Mn}^+(\text{H}_2\text{O})$	43
3.3 Molecular orbital diagram and electron occupancy of $\text{Mn}^+(\text{H}_2\text{O})$ ($X, ^7A_1$).....	44
3.4 Potential Energy curves of the ground and excited electronic states of $\text{Mn}^+(\text{H}_2\text{O})$ along the Mn–O stretch based on experiment.....	49
3.5 Scans along the out-of-plane bend in the ground and 7B_1 excited state showing the vibrational energy levels for $v_3''=0$ and $v_3'=0,1$ and 2 and the corresponding wavefunctions for states with even quanta.....	52
3.6 Photodissociation spectra of the origin band of the 7B_2 state (top) and 7B_1 state of $\text{Mn}^+(\text{H}_2\text{O})$ (bottom) showing the $\Delta K_a = \pm 1$ features characteristic of a perpendicular transition	56
3.7 Vibration action spectrum of $\text{Mn}^+(\text{H}_2\text{O})$ in the O-H stretching region.....	61

4.1	Infrared photodissociation spectra of $\text{Fe}_2^+(\text{CH}_4)_n$ ($n=1-3$) in the C-H stretching region.....	71
4.2	Infrared photodissociation spectra of $\text{Fe}_3^+(\text{CH}_4)_n$ ($n=1-3$) in the C-H stretching region.....	72
4.3	Infrared photodissociation spectra of $\text{Fe}_n^+(\text{CH}_4)_n$ ($n=2-4$) in the C-H stretching region.....	73
4.4	Experimental IR photodissociation spectrum of $\text{Fe}_2^+(\text{CH}_4)$ along with the simulated spectra using the B3LYP, BPW91 and M11L functionals.....	78
4.5	Experimental IR photodissociation spectrum of $\text{Fe}_2^+(\text{CH}_4)_2$ along with the simulated spectra using the B3LYP, BPW91 and M11L functionals.....	81
4.6	Experimental IR photodissociation spectrum of $\text{Fe}_2^+(\text{CH}_4)_3$ along with the simulated spectra using the B3LYP, BPW91 and M11L functionals.....	83
4.7	Experimental IR photodissociation spectrum of $\text{Fe}_3^+(\text{CH}_4)$ along with the simulated spectra using the B3LYP, BPW91 and M11L functionals and the 6-311++G(3df,3pd) basis set.....	85
4.8	Experimental IR photodissociation spectrum of $\text{Fe}_3^+(\text{CH}_4)_2$ along with the simulated spectra using the B3LYP, BPW91 and M11L functionals and the 6-311++G(3df,3pd) basis set.....	88
4.9	Experimental IR photodissociation spectrum of $\text{Fe}_3^+(\text{CH}_4)_3$ along with the simulated spectra using the B3LYP, BPW91 and M11L functionals and the 6-311++G(3df,3pd) basis set.....	89
4.10	Experimental IR photodissociation spectrum of $\text{Fe}_4^+(\text{CH}_4)_4$ along with the simulated spectra using the B3LYP, BPW91 and M11L functionals and the 6-311++G(3df,3pd) basis set.....	92
5.1	Mass spectrum of $\text{Cr}^+(\text{NH}_3)$	102
5.2	Custom mass gate structure before complete assembly.....	103
5.3	Custom mass gate after complete assembly.....	104

CHAPTER 1

INTRODUCTION

1.1 Introduction

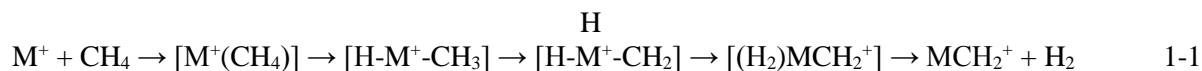
The study of the molecular level interactions between transition metals and water is key to understanding many processes including solvation, homogeneous catalysis and metals in biology. Similarly, the study of interactions between transition metal ions and clusters with hydrocarbons is of great importance in the understanding of C-H activation reactions which are involved in generation of fuels. Some transition metal cations have the ability to activate methane at room temperature, as do some transition metal clusters. Although gas-phase metals aren't practical catalysts, they are good models for understanding the mechanism of the reaction because the reaction conditions are easy to control. This makes gas phase studies ideal for studying the core interaction of C-H bond activating catalysts. An additional advantage of studying gas-phase ion-molecule reactions is that some of the intermediates of these reactions are more stable than the reactants. Thus, understanding the mechanisms behind these reactions can be done by characterizing the structure and bonding in the molecular reactants, products, and intermediates. This characterization is made possible by combining experimental spectroscopy with computational studies to elucidate the state of a system and provide insight into molecular geometries and binding characteristics of ions. In this work, we explore two non-covalent interactions involved in solvation and catalysis by studying entrance-channel complexes of the reactions of transition metal ions with water and methane.

1.2 Motivation

The importance of metal ion-water interactions in solvation, catalysis and biology have long stimulated various experimental and computational investigations with the purpose of better understanding the complexes. By carrying out experiments in the gas phase a detailed examination of ion-solvent interactions and their dependence or correlations to characteristics such as the ions'

electron configuration, geometry and cluster size can become clearer. Techniques such as bimolecular reactions,¹⁰⁸ collision induced dissociation,⁸⁸ vibrational and electronic spectroscopy,^{27, 64-65} have been used to characterize structure and bonding in metal-water complexes by measuring their binding energies and vibrational frequencies.^{11, 27, 64-65} In Chapter 3 we explore the metal-water interaction between manganese cation and a single water molecule, utilizing electronic and vibrational spectroscopy to examine the frequencies of vibrational modes in the ground and excited states.

Catalytic activation of methane has long been studied in hopes of finding an efficient and selective route for conversion of methane to a liquid fuel such as larger hydrocarbons or methanol. The ability to convert the abundant feedstock of natural gas to a liquid transportation fuel would clearly be of great benefit to the energy industry, and this has made methane activation a major goal in the field of catalysis.⁶ The basic mechanism for the activation of methane by metal ions in the gas phase is as follows.



This reaction is exothermic and occurs under thermal conditions for most third-row transition metals, although is endothermic for the first and second row metals.^{42, 49, 89, 93} Due to these gentle conditions, reactions of gas-phase metal ions are an ideal model system with desired reactivity that can be studied extensively through experiment and supported through calculations to gain a much clearer understanding of these reactions. The feasibility of approach has been shown by multiple reaction studies of the activation of methane by gas-phase metal atoms and ions.^{7, 71, 90, 97} As the metal-methane interaction involves varying degrees of covalency which often depends on the metal and number of methanes, many different metal-methane systems have been examined using vibrational spectroscopy to characterize the structure and bonding of intermediates and to correlate them to measured reactivities.^{22, 31, 54, 75, 77, 79} Vibrational spectroscopy is particularly useful for these systems due to the C-H stretching frequencies being very sensitive to the structure and M⁺-C bonding / C-H antibonding interactions.

In addition to more general studies of metal-methane complexes, this work examines metal-methane cluster systems, where multiple metals bind varying numbers of methane molecules. Certain metals such as Au_n^+ ⁵⁸ and Rh_n^+ ¹⁸ have been seen to not react with methane when only one metal atom is present (e.g. Au^+), but to increase in reactivity when in a cluster (e.g. Au_2^+). This clustering allows otherwise unreactive metals to react and activate methane. When thinking about catalysis, it is convenient for the metal used as the catalyst to be earth abundant and cheap if it is to be used often and in large amounts. This makes the less abundant but often more reactive third-row metals less lucrative. It would therefore be a great advantage that if by clustering multiple cheap first row metals like Ni into Ni_2 or Ni_3 , one could achieve similar reactivity as a rare or expensive metal. Thus, systems whose reactivity depends strongly on cluster size, such Pt_x^+ , or abundant first row metals, have been suggested to be a good candidate for a material that may make a good heterogenous catalyst.^{56, 85}

These methane-cluster studies generally aim at expanding our understanding of strong non-covalent metal-ion ligand interactions. Although methane binds by ~ 100 kJ/mol, classifying it as non-covalent due to the large electrostatic component which typically dominates the binding energy is not the whole picture. There may also be electron density donation from bonding orbitals on the ligand to empty orbitals on the metal, as well as back donation to anti-bonding orbitals on the ligand which contribute to metal-ligand binding. This importantly weakens the bonds in the ligand. By examining this weakening by varying the amount of metals and ligands in the cluster, a greater understanding of the binding interaction and catalytic activation of C-H bonds in the ligand can be brought about. Study of the clusters in the C-H stretching region by vibrational spectroscopy of the fairly intense IR frequencies can determine the most likely structures and bonding motifs of the clusters as they increase in numbers of metals and ligands. In addition, comparison of experimental spectra to electronic structure calculations using multiple density functionals will help to identify possible isomers, the most likely structure and geometry of each cluster, and what functionals are most appropriate to use for different sized clusters. In Chapter 4 we investigate metal-methane clusters of iron and methanes.

1.3 Photofragment Spectroscopy

The main experimental technique employed in this work to measure electronic and vibrational spectra of ions is photofragment spectroscopy. In this technique, a cloud of mass selected ions is irradiated by a laser, and the yield of fragment ions (at a different mass) is monitored. This is especially effective for ions that are mass selected because the parent ions and fragment ions of different masses separate in time and can therefore be easily detected. This photodissociation of cations leads to charged fragments which are easily detectable by a micro-channel plate (MCP) detector, giving the signal, which is the main data for the experiment. Using a time-of-flight mass spectrometer, the parent and fragment ions can be efficiently detected and readily distinguished. This allows us to detect photofragmentation even with dissociation yields of $\leq 1\%$. The photofragment mass spectrum allows us to identify which photofragments are produced at a particular wavelength and their yield. The total photodissociation spectrum is compiled by monitoring parent and fragment ion yields while scanning the energy of the dissociation laser over a spectral region. For photofragmentation to occur three requirements must be met. First, the molecule of interest must absorb a photon, that photon then must have enough energy to break a bond in the molecule, and lastly the quantum yield for dissociation must not be zero. The photodissociation spectrum is thus the product of the absorption spectrum and photodissociation quantum yield. For most molecules we study the photodissociation spectrum mirrors the absorption spectrum because the photodissociation quantum yield is 100%. Clearly if enough energy to break a bond is not supplied by the photon, dissociation will not occur. The onset of photodissociation thus gives an upper bound to the bond strength of the molecule.

This technique has the potential to reveal a great deal of information. By design, the photon with the smallest possible energy that still causes the molecule to dissociate upon absorption sets the upper limit to the bond strength of the bond broken to cause fragment formation. Due to the nature of transition metal complexes, many electronic states tend to be present, often causing metals to absorb

widely. Thus, metal containing complexes tend to absorb near the dissociation limit, making the upper bounds found in experiments close to or at the true bond strength of the molecule.

After absorbing a photon, target molecules tend to dissociate easily, resulting in a photofragment spectrum that closely resembles the absorption spectrum above the dissociation energy. In this case photofragment spectroscopy provides a sensitive way to measure the absorption spectrum, which is necessary because we do not produce enough ions to measure the absorption spectrum directly. The information typically obtainable from an absorption spectrum is also discernable here. This includes directly measured quantities such as the positions of excited electronic states and their vibrational frequencies, as well as partially resolved rotational structure in some cases. Indirect measurements include spectroscopic constants, bond lengths, molecular geometries and other properties such as excited state lifetimes based on breadth of a peak. Depending on the potential energy surface (PES), the molecule of interest may completely dissociate in a shorter time than is needed to observe molecular vibrations. This process is known as direct dissociation (seen in **Figure 1.1**). In a different, more beneficial case to this work, a molecule may undergo predissociation, in which case the dissociation occurs slowly enough for vibrations or even rotations to be observed. This typically is a result of the molecule becoming trapped in a well of the PES, and only dissociate because of internal conversion or intersystem crossing. Predissociation characteristically results in a much sharper spectrum allowing for better analysis of spectroscopic and rotational constants, revealing important vibrational and rotational information about the molecule. Gaining access to this information is a large benefit in using photodissociation spectroscopy to study molecules in the gas-phase.

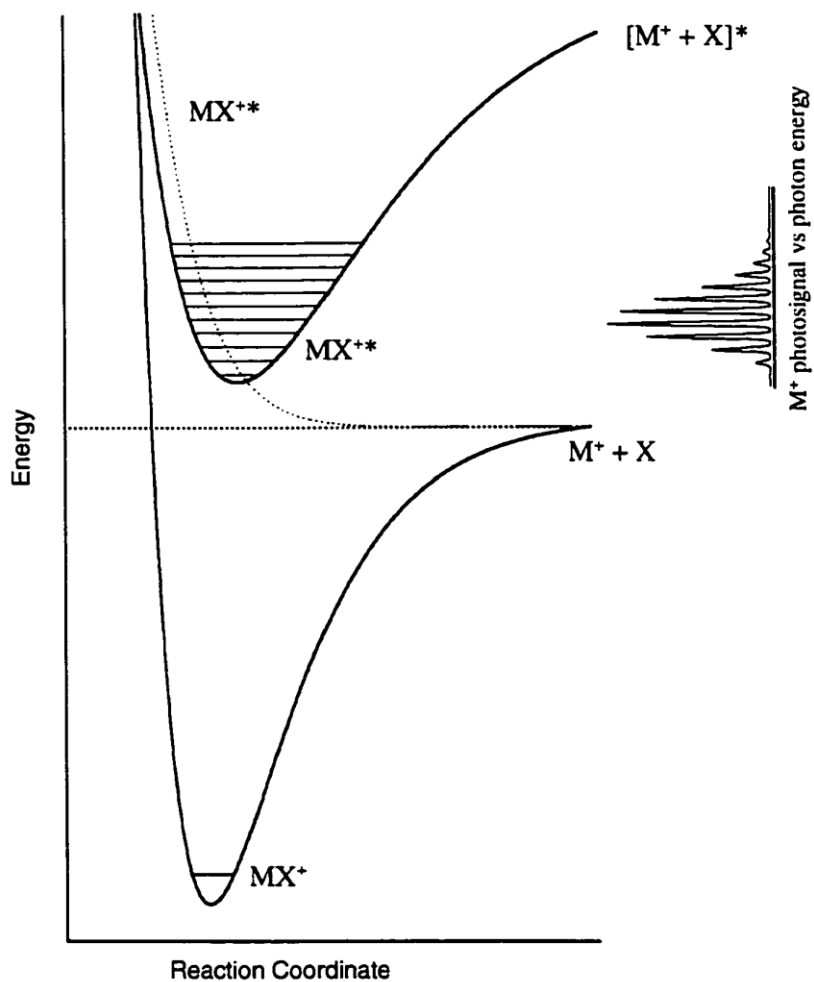


Figure 1.1 An illustration of the photofragmentation process. The consequence of absorption of a photon is dissociation of the ion. An ion can absorb a photon and be excited to a repulsive excited state (dotted line) resulting in direct dissociation and a broad unstructured photodissociation spectrum. Absorption to a diabatically bound excited state (solid line) leads to predissociation via internal conversion or intersystem crossing. If this process is sufficiently slow then the spectrum will show vibrationally and even rotationally resolved structure.

References

1. Weis, P.; Kemper, P. R.; Bowers, M. T. *J. Phys. Chem. A* **1997**, *101*, 2809-2816.
2. Schröder, D.; Schwarz, H.; Hrusák, J.; Pyykkö, P. *Inorg. Chem.* **1998**, *37*, 624-632.
3. Dalleska, N. F.; Honma, K.; Sunderlin, L. S.; Armentrout, P. B. *J. Am. Chem. Soc.* **1994**, *116*, 3519-3528.
4. Magnera, T. F.; David, D. E.; Michl, J. *J. Am. Chem. Soc.* **1989**, *111*, 4100-4101.
5. Marinelli, P. J.; Squires, R. R. *J. Am. Chem. Soc.* **1989**, *111*, 4101-4103.
6. Beyer, M. K. *Mass Spectrom. Rev.* **2007**, *26*, 517-541.
7. Alvarez-Galvan, M. C.; Mota, N.; Ojeda, M.; Rojas, S.; Navarro, R. M.; Fierro, J. L. G. *Catal. Today* **2011**, *171*, 15-23.
8. Irikura, K. K.; Beauchamp, J. L. *J. Phys. Chem.* **1991**, *95*, 8344-8351.
9. Schwarz, H. *Angew. Chem. Int. Ed. Engl.* **1991**, *30*, 820-821.
10. Shayesteh, A.; Lavrov, V. V.; Koyanagi, G. K.; Bohme, D. K. *J. Phys. Chem. A* **2009**, *113*, 5602-5611.
11. Hofstetter, T. E.; Armentrout, P. B. *J. Chem. Phys. A* **2013**, *117*, 1110-1123.
12. O'Hair, R. A. J. *Int. J. Mass Spectrom.* **2015**, *377*, 121-129.
13. Schwarz, H. *Angew. Chem. Intl. Ed.* **2011**, *50*, 10096-10115.
14. Armentrout, P. B. *Catal. Sci. Tech.* **2014**, *4*, 2741-2755.
15. Tonkyn, R.; Ronan, M.; Weisshaar, J. C. *J. Phys. Chem.* **1988**, *92*, 92.
16. Rodriguez, O.; Lisy, J. M. *Chem. Phys. Lett.* **2011**, *502*, 145-149.
17. Poad, B. L. J.; Thompson, C. D.; Bieske, E. J. *Chem. Phys.* **2008**, *346*, 176-181.
18. Dryza, V.; Bieske, E. J. *Int. J. Mass Spectrom.* **2010**, *297*, 46-54.
19. Citir, M.; Altinay, G.; Austein-Miller, G.; Metz, R. B. *J. Phys. Chem. A* **2010**, *114*, 11322-11329.
20. Kocak, A.; Sallese, Z.; Johnston, M. D.; Metz, R. B. *J. Phys. Chem. A.* **2014**, *118*, 3253-3265.
21. Roithova, J.; Schröder, D. *Chem. Rev.* **2010**, *110*, 1170-1211.
22. Lang, S. M.; Bernhardt, T. M.; Barnett, R. N.; Landman, U. *ChemPhysChem* **2010**, *11*, 1570-1577.

23. Chen, Y. M.; Armentrout, P. B. *J. Phys. Chem.* **1995**, *99*, 10775-10779.
24. Schlangen, M.; Schwarz, H. *Catal. Lett.* **2012**, *142*, 1265-1278.
25. Kummerlowe, G.; Balteanu, I.; Sun, Z.; Balaj, O. P.; Bondybey, V. E.; Beyer, M. K. *Int. J. Mass Spectrom.* **2006**, *254*, 183-188.

CHAPTER 2

EXPERIMENTAL

2.1 Instrument Overview

The Dual Time-Of-Flight Reflectron Mass Spectrometer (D-TOF-R-MS) (shown in **Figure 2.1**) is the instrument used for photofragmentation studies of ions in this work. It is also described in detail elsewhere.⁴³ It is helpful when thinking about the instrument to separate it into three main sections, each with their own purpose and possible alterations depending on the specific experiment. The first section is the source, where the ions of interest are formed. The second is the differentially pumped region, where ions are accelerated and mass separated to focus on the ion of interest. The last section of the instrument is the photodissociation and detection region where one or two lasers are used to induce photodissociation, then the ions are turned in the reflection, to mass separate fragment and parent ions. The ions are detected with microchannel plates (MCP) at the detector. The instrument and important components and interchangeable parts will now be described, with letters referring to approximate locations in the instrument seen in **Figure 2.1**.

A: Ablation laser. Either a Minilite (Continuum) or Surelite (Continuum) Nd:YAG laser is used to ablate a metal rod. The 1064 nm output is doubled to produce 15mJ/pulse at 532 nm, which is focused with a 1m focal length lens to form a ~0.15 mm diameter spot on the metal rods surface. The laser power can be altered to produce varied amounts of a given ion. In principle, increasing the power of the ablation laser will provide more metal ions. However, since the ablation laser hits the metal rod after the precursor is introduced, higher powers result in decomposition of the precursor molecules in the intense plasma formed by the ablation laser. An ablation energy slightly higher than typical tends to increase signal of larger metal cluster ions(M_x^+), while lower power settings often help in making clusters with more ligands attached.

B: Metal rod. To create ions or clusters a metal rod of the desired metal (Typically 99.8% pure) is then machined to instrument specifications. To ablate a fairly fresh portion of the rod on each shot, the rod is rotated at an adjustable speed (typically at ~ 2 min/rev) and translated ($1/80''$ /rev). This allows for a $2''$ rod to be run for ~ 7 hours before the same spot is reached twice. Depending on the metal and precursor gas, the same spot can be run several times before the rod needs to be polished, which is useful if certain areas of the rod produce a more stable signal as sometimes occurs. The metal rods are typically $\leq 0.250''$ diameter.

C: Precursor gas, pulsed valves and nozzles. The $M_x^+(\text{CH}_4)_n$, $M^+(\text{H}_2\text{O})$, and $M^+(\text{D}_2\text{O})$ complexes are formed by clustering the ligand onto M^+ produced by laser ablation. However very different source conditions and configurations are used for metal cluster ions than for complexes with a single metal atom. For studies of $\text{Mn}^+(\text{H}_2\text{O})$ and isotopomers a home-built piezoelectric pulsed valve⁷⁶ introduces the precursor gas into the source chamber at a backing pressure of 35 psi. The valve opening time is adjustable from 250-550 μs . This gives a duty cycle of $\sim 1\%$, which allows us to have high gas densities in the source region for efficient clustering and cooling while using vacuum pumps of modest size. The gas mixture is primarily helium and flows over a bubbler containing H_2O , resulting in $\sim 0.7\%$ H_2O in the gas mixture. A small amount (2-10%) of H_2 is also added to enhance vibrational cooling. Collisions with the bath gas in the source block cool the ions to ~ 300 K, then supersonic expansion into vacuum ($\sim 10^{-4}$ - 10^{-5} Torr) further cools ions to rotational temperatures of ~ 15 K as shown in the rotational structure of the spectrum. Much higher backing pressures are required to efficiently make metal clusters. The piezoelectric pulsed valve does not work past 60 psi, therefore we substitute it with a solenoid valve (Parker General Valve Series 9). In the iron cluster studies, the primary valve has 0.1-2% CH_4 . Typical backing pressures are 80 psi for $\text{Fe}_2^+(\text{CH}_4)_n$, 120 psi for $\text{Fe}_3^+(\text{CH}_4)_n$ and 160 psi for $\text{Fe}_4^+(\text{CH}_4)_n$. We find that pure He does not produce significant amounts of metal clusters, while the high ablation laser powers used to create clusters can fragment the methane, leading to a congested mass spectrum. To minimize this issue, we limit the percentage of

methane introduced by the primary valve and add a second valve to introduce methane downstream of ablation, after ions have cooled. The secondary valve carries 100% methane at a backing pressure of 5-20 psi. This design has the advantage of giving independent control over the methane concentration (to optimize production of clusters containing the desired number of methane ligands), as well as reducing the possibility of the ablation laser and resulting plasma from fragmenting methane. The nozzles are made from ½-13 aluminum threaded rod so that nozzles of different lengths are convenient to make and sections can be joined easily using nuts. The aluminum nozzles vary in length from 5-50 mm and have 2.5 mm ID, as shown in **Figure 2.2**. Various nozzle configurations of different final total lengths are used to produce different ions, with longer sections typically forming larger clusters due to more time for collisions to take place. The sections are usually finished with a short 10° cone ~10 mm in length.¹⁰¹

D: Skimmer. The molecular beam formed in the source passes through a 3 mm diameter cone-shaped skimmer before entering the first differential chamber. The purpose of the skimmer is to intercept the center of the supersonic gas expansion, while limiting gas flow into the differential chamber, which is at $\sim 10^{-6}$ Torr.

E: Acceleration region. Here, ions are accelerated in two stages (Wiley-McLaren¹¹¹ type accelerator). The first acceleration stage is called the extraction and is typically + 80 V and is pulsed. In the second stage, the ions are accelerated from ground to a potential of -1800 V, and gain an equal amount of kinetic energy. Since $KE = \frac{1}{2} mv^2$, ion of different masses will have different velocities, allowing separation based on their mass to charge ratios.

F: Re-referencing tube. To avoid floating the flight tube at -1800 V, ions are rereferenced

to ground potential.⁶⁴ When they enter this 10 cm long, 5 cm dia. tube, the potential is -1800 V, before they exit it is rapidly pulsed to ground, so their kinetic energy is not changed, but now they are at ground potential.

G: Einzel lens. Upon exiting the re-referencing tube, ions are cylindrically focused by this charged particle lens that does not affect the energy of the beam.

H: Deflectors. A set of vertical deflectors sandwiched by two sets of horizontal deflectors are used to guide ions into the detector chamber. Each deflector is a pair of plates, one of which is grounded and a small voltage (<15 V) can be applied to the other plate to shift ion flight paths to find the optimal flight path for ions of interest.

I: Mass gates. The mass gate deflects the ions by the $\sim 5^\circ$ angle that allows them to successfully traverse the reflectron region and hit the detector. This deflector works with a constant or pulsed voltage of 30-60 V. If the voltage is constant all the ions make it through to the detector. If it is pulsed, only those ions in the deflector during the pulse will reach the detector. By adjusting the time of the pulse, we can discriminate against ions that may otherwise congest the spectrum and overlap the photofragment signal. Depending on the width of the pulse, only ions within ~ 2 amu of the target mass are transmitted. This is sufficient for most studies to avoid interference from parent ions for most complexes we study. However, in studies of larger $\text{Fe}_x^+(\text{CH}_4)_n$ clusters, combinations and isotopes often lead to peaks 1-2 μs before the parent ions, which interferes with the observation of the loss of one methane from heavier clusters. To help alleviate this problem a second mass gate was positioned further down the flight tube, beneath the turbo pump. As this was built after the studies described in this work, details of its implementation are given in Chapter 5.

J: Reflectron. Ions entering the reflection region are decelerated in an electric field, so they come to rest for a moment at the point where the potential in the reflectron is equal to their initial

kinetic energy. Ions are dissociated at the turning point of the reflectron. The ions of a particular mass can be dissociated over a ~100 ns laser firing time window. The ions are then re-accelerated such that they exit with the same kinetic energy as when they entered. This reacceleration is the primary benefit of the reflectron, as it means that fragment ions will have different velocities and flight times than the parents, allowing them to separate in time before reaching the detector.

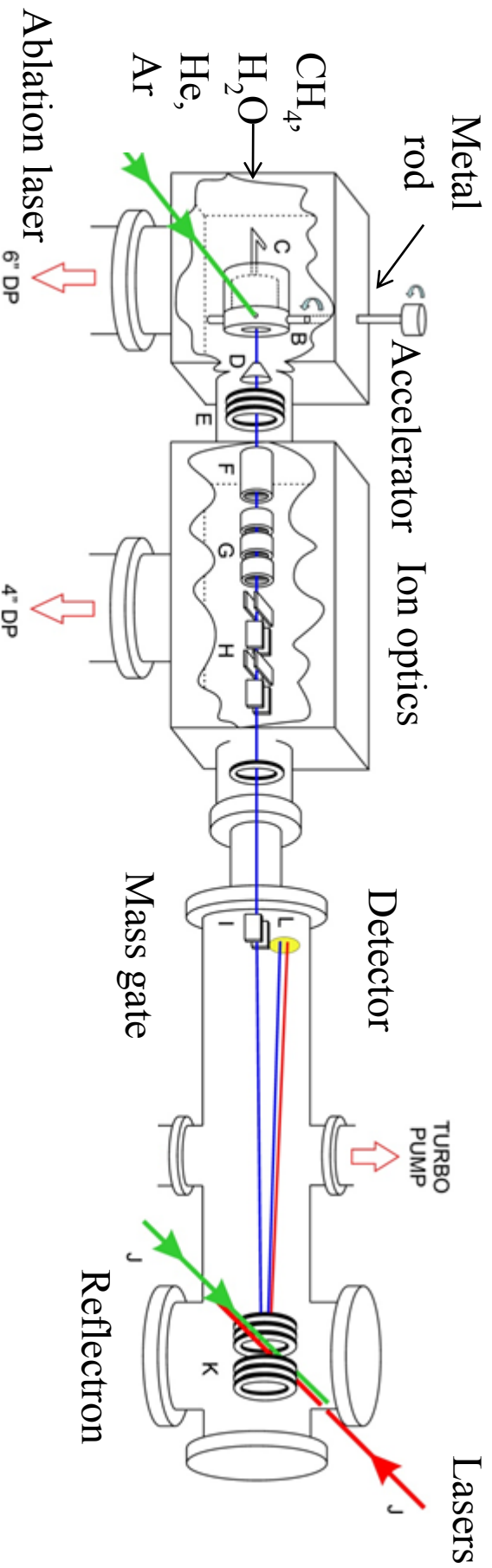
K: Dissociation laser(s). The mass selected ions of interest are photodissociated at the turning point of the reflectron by a pulsed laser (the particular lasers used will be discussed later). Multiple lasers can be overlapped for double resonance studies.

L: Multipass mirror: To help improve the photodissociation yield we use a Perry type multipass mirror setup.⁶ This consists of two concave spherical, silver coated mirrors, bracketing the reflectron plates. Alignment using a HeNe laser shows that the laser makes up to 21 passes through the ion beam. Silver is used for its high reflectivity in the IR. However, it does not reflect in the UV, and the dye laser must be attenuated to ≤ 10 mJ/pulse to avoid burning the mirror.

M: Detector: The detector consists of two 40 mm diameter microchannel plates (MCPs) and a solid stainless anode. When a charged particle strikes the surface near the entrance of a channel, electrons are ejected. A bias voltage accelerates these electrons, which strike the sides of the channel, ejecting more electrons. The MCPs have a net gain of 10^6 . This current pulse is converted to a voltage pulse using a 50 ohm resistor and is amplified 10 times to give a 2 ns wide, 20 mV pulse for each ion.

2.1.1 Laser Systems

Lasers are used for ion production (ablation) and for photodissociation spectroscopy. These are fixed wavelength Nd:YAG lasers, or are tunable lasers that are pumped by a Nd:YAG. The lasers that are used for the experiments include a Continuum Minilite I (for ablation), Continuum Surelite I



R. B. Metz, *Adv. Chem. Phys.* **138**, 331 (2008)

Figure 2.1 Schematic View of Dual Time-Of-Flight Reflectron Mass Spectrometer. Labels are explained in the text along with possible modifications for different experiments.

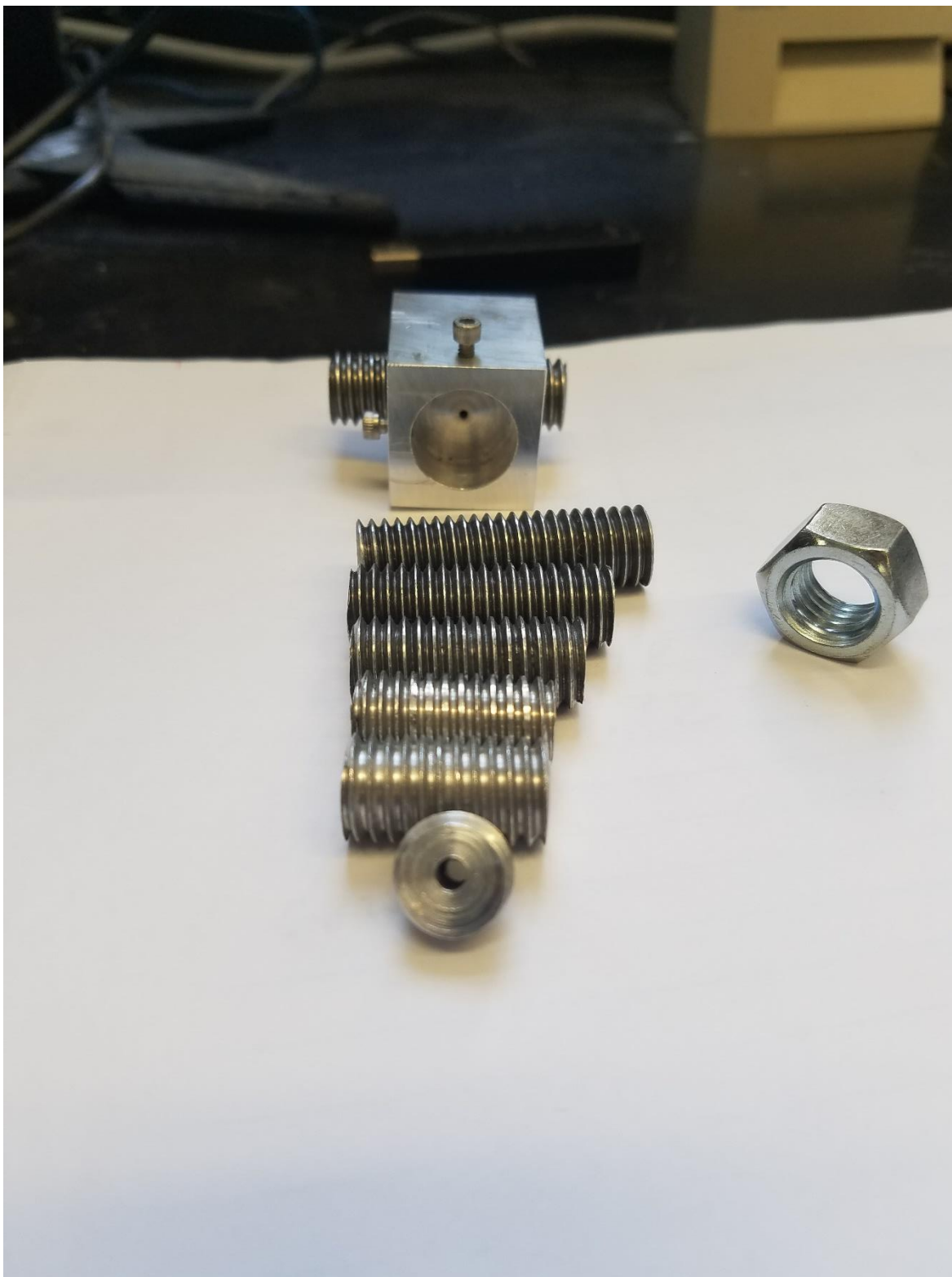


Figure 2.2 Aluminum nozzles and secondary valve holder used in the source region to facilitate cluster formation. Nozzles range in length from 5-50 mm and can be connected in series by nuts to make a custom collision tube. The smaller piece facing forward is the 10° cone typically attached at the end of the assembly.

(for ablation and as a pump laser for a ND6000 dye laser), Continuum Powerlite 8020 and SpectraPhysics QuantaRay GCR-190 (as pump lasers for a Laservision IR OPO/OPA system).

2.1.1.1 Nd:YAG Lasers

For the studies with manganese the ablation laser used was a Continuum Minilite I Nd:YAG laser operating at a repetition rate of 20 Hz. Its 1064 nm output is frequency doubled to give ~10-15 mJ/pulse at 532 nm with a pulse width of 5-7 ns and a linewidth of 1 cm^{-1} . For studies involving methane, the ablation laser used was a Continuum Surelite I-20, also an internally Q-switched Nd:YAG. The Surelite I produces ~100-135 mJ at 532 nm at a rep. rate of 20 Hz with 4-6 ns pulse width. This power is reduced by ~90% via a beam splitter to provide 10-16 mJ/pulse of power for ablation. In the manganese studies, the Surelite was used as a pump laser for a ND6000 dye laser. To pump the IR OPO/OPA system we used a QuantaRay GCR-190. It produces ~900 mJ/pulse at 1064 nm with 10 Hz rep. rate. With an attenuator, the power is reduced to 550-700 mJ/pulse before entering the IR OPO/OPA system in order not to damage the IR OPO/OPA crystals.

2.1.1.2 ND6000 Dye Laser

The electronic spectroscopy studies ($\text{Mn}^+(\text{H}_2\text{O})$ and $\text{Mn}^+(\text{D}_2\text{O})$) used a Continuum ND6000 dye laser for photodissociation. The core of the ND6000 dye laser is a dye oscillator and two dye amplifier cells, which are pumped by the Powerlite 8020 series ND-YAG laser. The input pump energy for the dye laser is ~300 mJ at 532 nm. A dye solution (various dyes are used to maximize power at different wavelength regions) is circulated to absorb the beam at 532 nm and emit (fluorescence) at higher wavelengths. The wavelength is selected by tuning the angle between the grating and a mirror in the oscillator cavity. The beam power is amplified through two amplifiers. The power output is typically 10-25% of the pump power. The output was doubled to work in the UV region ($28,000\text{-}36,000 \text{ cm}^{-1}$, 278-357 nm). Output power of the final stage was typically 3-15 mJ. The laser line width is $<0.1 \text{ cm}^{-1}$ (typically 0.05 cm^{-1}) for the dye fundamental and $<0.2 \text{ cm}^{-1}$ for the frequency-doubled output. This value can be checked experimentally using absorption lines in iodine.

An external computer controls the grating mirror angle to tune the wavelength. The wavelength of the fundamental output of the laser is calibrated using the photo-acoustic spectrum of water overtones or the atomic absorption lines of neon using optogalvanic spectroscopy.

2.1.1.3 LaserVision IR OPO/OPA

IR studies were conducted on the optical parametric oscillator/optical parametric amplifier (OPO/OPA) LaserVision IR system. This laser system is tunable from 2 to 4.5 μm , producing ~ 6 mJ/pulse near 3100 cm^{-1} and 10 mJ/pulse at 3500 cm^{-1} . The pump laser is the previously mentioned Spectra Physics GCR-190 operating at 10 Hz. The pump beam is 550-700 mJ/pulse at 1064 nm with a ~ 6 ns pulse width. The pump beam is first split in two by a beam splitter, and one part is frequency doubled by a potassium titanyl phosphate (KTP) crystal to produce 532 nm light. This pumps the OPO which also uses nonlinear KTP crystals. In a second order non-linear crystal, if a beam with a frequency of ω_p enters the crystal, two output beams (signal and idler) exit the crystal with frequencies of ω_s and ω_i . The beam with the higher frequency is historically called the signal beam, while the lower frequency beam is called the idler beam. The sum of the output waves' frequency is equal to the input wave's frequency. In our OPO, a pair of KTP crystals is placed in a lasing cavity formed by two end mirrors to improve the efficiency. The beam is also coupled with a grating to improve the efficient conversion to signal and idler.

By changing the angle of the crystals, the signal/idler frequency ratio can be varied. Thus, the beam in the OPO is divided into a visible signal beam (tunable from 712 nm to 880 nm; i.e. 11364 cm^{-1} to 14085 cm^{-1}) and a complementary near-IR idler beam (tunable from 2.1 to 1.35 microns; i.e. 7433 to 4712 cm^{-1}). In the Optical Parametric Amplifier (OPA) stage, four potassium titanyl arsenate KTA crystals (two pairs) use the idler of the OPO and the remainder of the split 1064 nm (9398 cm^{-1}) beam to produce mid-IR light at 2200 cm^{-1} (1 mJ/pulse) to $> 4000\text{ cm}^{-1}$ (15 mJ/pulse) using difference frequency generation. The IR linewidth is typically $\sim 1.8\text{ cm}^{-1}$, and all spectra simulations use this value. This linewidth can be checked experimentally using the absorption spectra of H_2O or CH_4 . Also

of note is the dissociation cross-section, which is an indicator of how large of a target the molecule is for the laser to photodissociate. For example, the cross section for dissociation of $\text{Fe}_3^+(\text{CH}_4)_3$ at 2800 cm^{-1} is $\sim 8 \times 10^{-19}\text{ cm}^2$. This is based on 20% parent photodissociation at an IR laser power of 7 mJ/pulse and a beam area of 0.5 cm^2 . This is a typical result with values from 10^{-18} - 10^{-19} being in line with cross-sections of similar ions.³⁶

A computer controls the angles of all six crystals using a servo motor (motor #2 – motor #7). There is also one servo motor for controlling the grating-mirror angle, which determines the wavelength (motor #1). This motor acts as the leading device to initiate the other motors' movements and maintain calibration. Calibration of the motor is of course critical to assure that the wavelength where the computer thinks the laser is parked is where it really is. The calibration is typically made using a glass cell filled with CH_4 or H_2O vapor and comparing the IR absorption spectrum obtained with literature standards.⁸² At each wavelength, all the crystals need to be positioned correctly to maximize the output power. To do this as best as possible, implementation of a calibration curve in which the optimum motor position is fit to a polynomial as a function of wavelength is needed. Due to the calibration curves provided by the vendor only covering a small range of $\sim 100\text{ cm}^{-1}$ and our spectra often covering up to 600 cm^{-1} , custom curves were needed. To create a custom calibration curve, at 50 cm^{-1} intervals, each motor was adjusted to maximize power. The resulting motor positions vs. wavelength values are fit to a polynomial. This equation roughly follows the form of (Position = $C_0 + C_1(\lambda - L_0) + C_2(\lambda - L_0)^2 + C_3(\lambda - L_0)^3 + \dots$ up to 10th order is possible). Ideally, the motor positions can be calibrated in a way that the wavelength scans will cover the whole IR region (2500 - 4000 cm^{-1}) without recalibrating.

In general, the higher order the polynomial, the better fit to the motor positions. On the other hand, if the calibration curve uses a smaller order polynomial, it will likely maintain power even outside the calibration range it is calibrated whereas the higher order polynomials lose power rapidly once outside the range. Due to the symmetric and antisymmetric C-H stretching frequencies for

$M^+(\text{CH}_4)_n$ complexes laying from $\sim 2500\text{ cm}^{-1}$ to 3100 cm^{-1} , the range is small enough that only one calibration curve was needed for the Fe^+ studies presented here. A separate curve was used for the $\text{Mn}^+(\text{H}_2\text{O})$ studies. Vibrational frequencies of O-H symmetric and antisymmetric stretches lie from ~ 3500 to 3800 cm^{-1} . Thus, for $M^+(\text{H}_2\text{O})$ studies, we can calibrate motor positions for only a 300 cm^{-1} range (from 3500 cm^{-1} to 3800 cm^{-1}). As studies utilizing the IR in the O-H stretching region and C-H stretching region were done far apart in time, the polynomials did not need to cover both ranges simultaneously.

The wavenumber calibration is made using the rotationally resolved IR absorption spectrum of H_2O vapor from $3100\text{-}3800\text{ cm}^{-1}$ and CH_4 gas from $2600\text{-}3200\text{ cm}^{-1}$. Known spectra of these molecules are available from the high-resolution transmission molecular absorption database (HITRAN).⁸² To obtain absorption spectrum we use a glass cell with sapphire entrance and exit windows. The cell is filled with the desired gas at 0.025 to 1 atmosphere of pressure and a power meter is placed after the exit window of the cell. When the IR is tuned to an absorption line, the power reading will be reduced. Since the P, Q, and R branches are obvious and very sharp, it is therefore straightforward to calibrate the laser wavelength (see **Figure 2.3**).

2.1.2 Time of Flight and Timing

To collect data successfully for pulsed photodissociation experiments the timing of the lasers and pulses from other components is vital. The ion production, selection and photolysis all involve voltage or light pulses. The relative times of each component are adjusted frequently on a microsecond or sub-microsecond time scale to maximize signal. To begin, the pulsed valve is triggered at $t=0$. After that, the ablation laser flash lamp, extraction, rereferencing, mass selection, and dissociation laser flash lamp and Q-switch all need to be triggered in turn, at the proper times. A pair of DG 535 digital delay generators from Stanford Research Systems controls the timing. Each generator can produce four different pulses, or two channels can be combined to produce a pulse with a specific start time and width. Rather than using two channels to set the start and end time, a simple external one-shot circuit

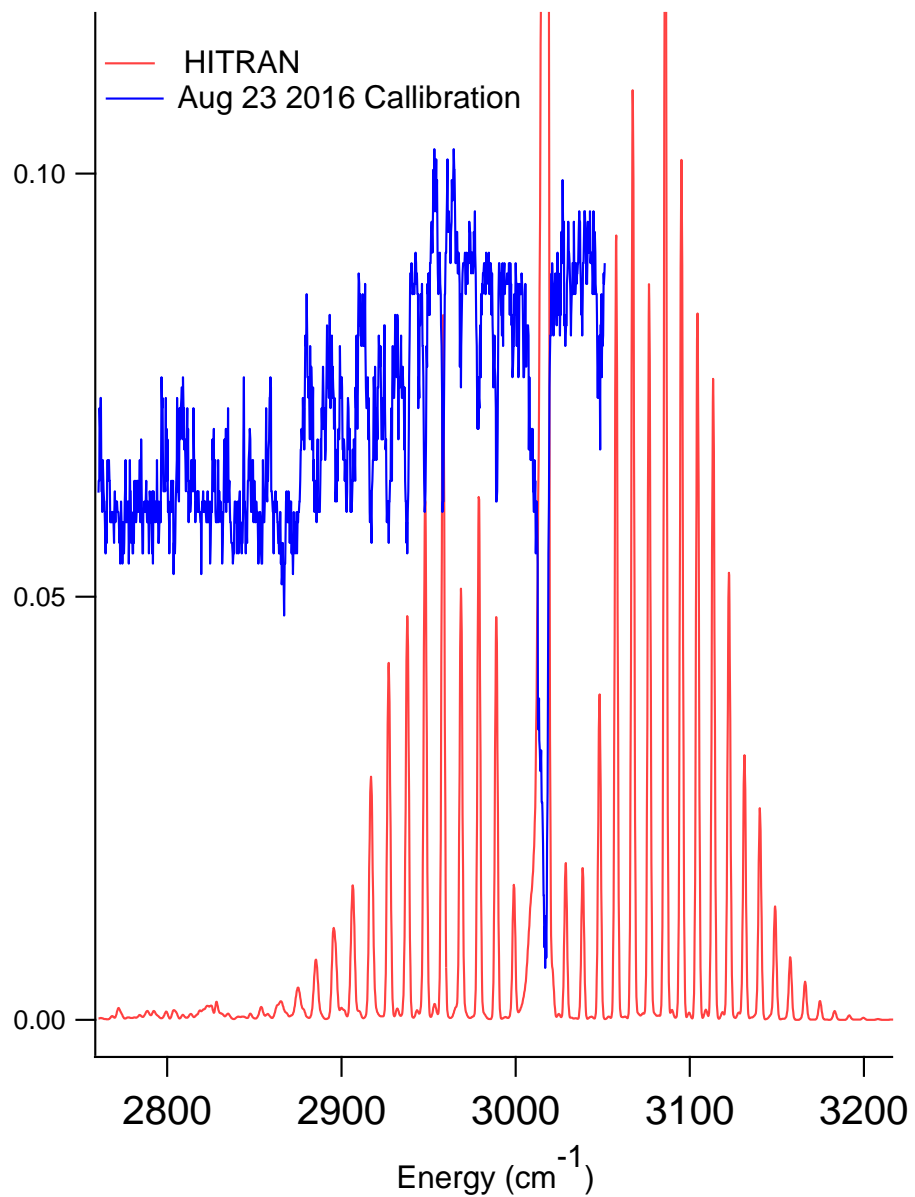


Figure 2.3 Experimental (blue) and simulated HITRAN (red) absorption spectra of methane. The experimental spectrum was shifted by $+1.0 \text{ cm}^{-1}$ to match the HITRAN data. The spectrum was measured at low pressure so that the Q branch line at 3016 cm^{-1} is not saturated.

is often used. It takes a pulse from the DG 535 and produces a pulse of the appropriate but fixed width. The general procedure for how the timings operate with each other is shown in **Figure 2.4** and described below.

First, the digital delay generator triggers the pulsed valve (at $t=T_0$), as it takes time for the valve to physically open and for gas to flow to the rod. The flashlamps on the ablation laser fire after a $\sim 200 \mu\text{s}$ delay. The laser Q-switch delay is set internally to $185 \mu\text{s}$, and light comes out $<0.1 \mu\text{s}$ later. The ablation laser time is frequently adjusted in order to overlap with the gas and optimize the yield of ions. The ions are extracted after a $\sim 200\text{-}250 \mu\text{s}$ delay, depending on the gas mixture and to a lesser extent the cluster size. The re-referencing pulse is $\sim 2.0\text{-}4.5 \mu\text{s}$ after the extraction. A shorter time will allow only lighter ions to make it through, while a longer time will select only heavier ions. Finally, ions are mass selected with the pulsed mass gate, at typical delays of $15\text{-}25 \mu\text{s}$ (according to the mass of the desired ions) with respect to extraction time. By adjusting the timings mentioned above, parent ions can be successfully chosen.

For the photofragments, photodissociation laser timings also need to be adjusted. For the photodissociation lasers (both dye laser and IR laser), the flashlamp firing time and external Q-switch delay time are controlled by a second digital delay generator which is triggered from the extraction pulse from the first generator. For these lasers, the Q-switch time is triggered to overlap with the ions of interest. This is typically 20 to $50 \mu\text{s}$ after the extraction, depending on the mass of the ion. The flashlamp-Q switch delay is kept constant for best power and beam quality, and is about $400 \mu\text{s}$. Thus, the flashlamp fires $\sim 350 \mu\text{s}$ before the extraction and depending on the ion, might fire before the pulsed valve. Since the digital delay generator cannot apply negative time delays, we use the fact that the experiment runs at exactly 20 Hz repetition rate, controlled by the digital delay generator. This means that each cycle repeats after exactly 50 ms (with better than 1 ns precision). So, a delay of $-400 \mu\text{s}$ is equivalent to $+49,600 \mu\text{s}$ (49.6 ms).

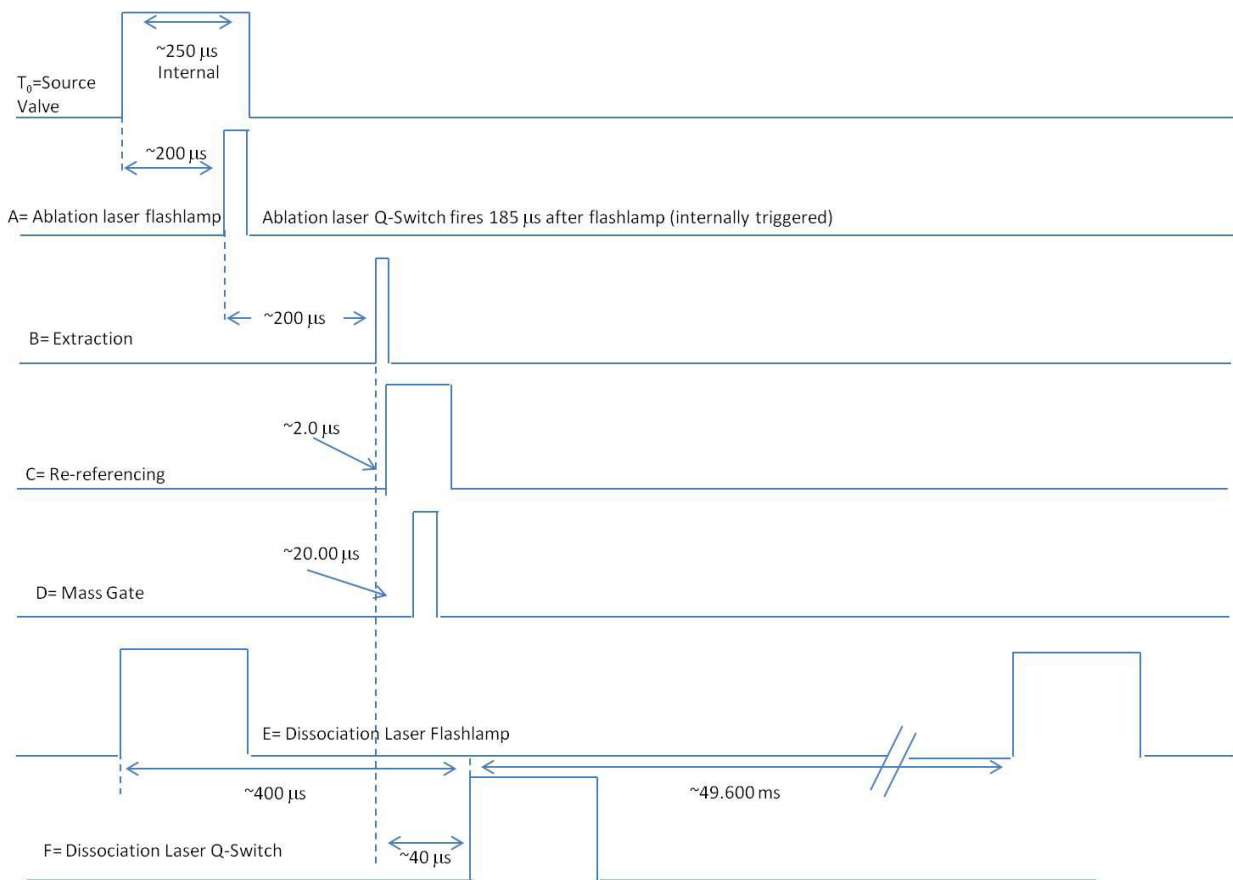


Figure 2.4 Time delay flowchart for instrument. Repetition rate of 20 Hz.

The SpectraPhysics QuantaRay GCR 190 operates at 10 Hz, meaning IR data should be collected at 10 Hz, synchronously with the firing of the IR laser. This is done by building an additional box that takes one pulse from the digital delay generator and sends it to trigger the YAG. Simultaneously, it generates a long blanking pulse. Any trigger pulses received during the blank pulse are skipped, reducing the number of pulses by ½. Because the ablation portion of the instrument works at 20 Hz, this presents a useful opportunity to do difference spectroscopy. In this situation, the ‘IR laser on’ pulses are used as the real data, and the ‘IR laser off’ pulses are treated as the background, with the difference between them giving the net fragment signal. This offers a much higher degree of sensitivity.

To estimate timings a few equations are used. For the time of flight of singly charged ions:

$$KE = \frac{1}{2} mv^2 \quad 2-1$$

Since v can be considered L/τ , where L is the length of the flight tube and τ is the ions flight time

$$\tau = \sqrt{\frac{L^2}{2}} \sqrt{\frac{m}{KE}} \quad 2-2$$

More precisely we use

$$\tau = c\sqrt{m} + \tau_0 \quad 2-3$$

where c (proportionality) and τ_0 (a small time correction) are constants and m is the mass of the desired ion. Once we produce M^+ ions (of known mass), we first assume $\tau_0 = 0$ and find a rough c value (which is $\sim 5.88 \mu\text{s}/\text{amu}^{1/2}$). Next, we predict a second ion and find real τ_0 and c values. After that, we apply this equation to find all the ions that we produce. The precision of the constants can be further improved by graphing the known masses and predicted times for ions that span a range of masses. The re-referencing time, mass gate time, and photolysis laser firing time all depend on mass of the ion. This means that when a new ion is studied or a serious change to the instrument is made it can be very helpful in orienting ourselves as to where the ions should be appearing before trying to tune up for them. Once timing for one ion is found, the timing for the second ion can be calculated and so on. Using equation 2-2 (with $\tau_0=0$),

$$\tau_2 = \tau_1 \sqrt{\frac{m_2}{m_1}} \quad 2-4$$

Thus, it simple to change between ions of interest using the related times when one ion is already known.

The flight times are different for parent ions than the photofragments. Parent ions fly down the entire flight tube to the reflectron where they decelerate and are irradiated, then the resulting parent and fragment ions reaccelerate and then fly a shorter distance to the detector. Their total flight time is

$$\tau_f = a\sqrt{m_p} + b\sqrt{m_f} + \tau_0 \quad 2-5$$

where m_p and m_f are the masses of the parent and fragment ions respectively. This equation also applies to un-dissociated parent ions, using $m_p = m_f$, and $a + b = c$. Subtracting equation 2-5 from equation 2-3, we can arrive at the flight time of the fragment ions relative to the corresponding parent,

$$\begin{aligned} \Delta\tau &= \tau_p - \tau_f = c\sqrt{m_p} - (a\sqrt{m_p} + b\sqrt{m_f}) \\ &= (c-a)\sqrt{m_p} - b\sqrt{m_f} \\ &= b\sqrt{m_p} - b\sqrt{m_f} \\ \Delta\tau &= b(\sqrt{m_p} - \sqrt{m_f}) \end{aligned} \quad 2-6$$

Due to the distance the ions travel $b \approx c(1/3) \approx 2.02 \mu\text{s}/\text{amu}^{1/2}$.

2.2 Data Acquisition

As discussed previously, when parent and fragment ions hit the detector they produce a voltage at a specific time according to their m/z ratio. This is either collected as a voltage vs. time trace on an oscilloscope and is read using the *Digital Scope Labview* program (typically for qualitative examination of data) or collected on the gated integrator with the total signal at a specific time window (mass) and recorded using the *Breakout Box Labview* program (This is how almost all data presented in this work is collected). This program is used for spectroscopy and there are two versions: *Breakout*

Box Dye Laser and *Breakout Box IR Laser*. The details of both programs have been previously described.^{23, 44}

2.2.1 Digital Scope

The *Digital Scope* program is used to measure time of flight (TOF) mass spectra or difference mass spectra at a fixed wavelength. This *Labview* program reads the voltage vs. time waveform information from a digital oscilloscope (Tektronix TDS 524A). As previously mentioned a difference spectrum is generated by recording the TOF spectra with the photodissociation laser on and subtracting the spectrum with the laser off. The laser is blocked/unblocked with a mechanical chopper wheel (used in Mn^+ studies) or a smart shutter in later studies (Lambda 10-B/Smart Shutter from Sutter Instruments). The program allows the user to decide the number of laser shots in each on/off cycle and the number of cycles to average. We typically use 100 shots in each cycle and average 20 cycles. Thus, each file includes 2000 shots averaged, for each on and off. This provides a very precise value when compared to data taken while scanning the laser over multiple wavelengths where we typically average 20 points per wavelength in each file. The only difference from the previous studies is that when working with the 10 Hz IR laser, the oscilloscope is triggered at 10 Hz.

2.2.2 Breakout Box Dye Laser

This program is used for electronic spectroscopy, as it controls the dye laser. The program communicates with the remote computer which controls the dye laser and allows the user to input parameters such as scanning range and step size. The program starts by sending the dye laser to the starting wavelength. Then the *Breakout Box* program reads data from up to 4 gated integrators, typically averaging the results for 20 laser shots, then the program sends a pulse to the dye laser to move to the next wavelength step. After getting a response from the dye laser, the cycle is repeated and in the end a spectrum is recorded. The gated integrators (Stanford Research Systems SR250) measure the area under the voltage vs. TOF waveform, over a specific period of time (the gate) and produces a DC value, which is sent to an A/D converter and the resulting value is read by *Breakout*

Box. The user sets these gates to measure the signal for the parent and fragment ion(s) as needed and occasionally a gate is used for background at a time where fragment ions should never be present.

2.2.3. Breakout Box IR Laser

This program is used for vibrational spectroscopy as it controls the IR laser. The working principle is similar to the dye laser program with roles slightly reversed. The program still communicates with a remote computer which scans the IR wavelengths, but here it acts as slave to that remote master computer. The user inputs the parameters into the main computer (starting and ending wavenumber and scan speed), and the parameters are then sent to the remote computer. The remote computer starts the scan and the *Breakout Box* program collects data and asks the master (remote) computer to tell it the current wavenumber. It then assigns the gated integrator value to that wavelength. The gated integrators are triggered at 10 Hz when working with the 10 Hz IR laser.

2.2.4 Data Analysis

The collected data is analyzed using the *Igor Pro* program. This analysis includes the averaging of ~5-20 sets of data (scan files) per wavelength region depending on stability and reproducibility for both parent and fragment ions. The fragment ions are normalized to the amount of parent and then to laser power. Multiple scans ensure that the results are reproducible and it significantly helps to reduce noise or abnormal oscillations especially when the fragment yield is small. The normalization is done by assuming the absorption cross section is equal to photodissociation cross section (i.e. dissociation quantum yield=1) the number of excited molecules is linearly dependent on laser power, and only a small percentage of molecules absorb. Although care is taken through polynomial curves in the IR and by changing dyes in the dye laser to keep the laser power during scans as stable and constant as possible, small variations are inevitable in different wavelength regions. To account for this, laser power scans are taken over the same region scans were taken in after the laser has warmed up for a fair amount of time in case power drops. The fragment yield is then divided by laser power over the scan range. This normalization assumes that the

fragmentation is proportional to laser power. This works well for one photon dissociation, but historically for IRMPD we find that the fragment yield is proportional to (laser power)ⁿ, with n=1.2 to 1.5, although this has not been looked into extensively in this work as most ions only required one photon to dissociate.⁵¹

2.3 Experimental Techniques

Using the experimental setup and instrumentation described in the previous sections, we use several techniques to perform studies with photodissociation spectroscopy. For any of the techniques discussed below to work, there are three requirements: 1) the molecule has to absorb the photon(s), 2) the absorbed photon energy is sufficient to break a bond, and 3) the photodissociation yield is non-zero.

2.3.1 Mass Spectra and Difference Spectra

In the case of a simple mass spectra, we optimize signal for the parent ion of interest and use a constant voltage on the mass gate (I in section 2.1) so that all the ions make it to the detector. Because ions with different m/z ratios have different flight times, this produces a TOF spectrum, which can be converted to a parent ion mass spectrum using equation 2-3. After getting the mass spectra, we can now pulse the mass gate to allow only the desired ions to make it to the detector. As described earlier, the mass gate delay time is calculated from a known ion with equation 2-4. When the photodissociation laser is off (or blocked), only parent ions are collected at the corresponding time calculated by 2-3. When the dissociation laser is on (or unblocked), parent ions still arrive at the same time but in decreased amounts, and fragment ions (with the time given by equation 2-5) appear if photodissociation occurs. By subtracting the spectrum of laser-off from laser-on, the difference spectrum is measured and the percent dissociation at a given wavelength can be determined more accurately.

From the difference spectra, we can get information about the dissociation products that are formed. **Figure 2.5** shows a sample difference spectrum of Cu⁺(CH₄)₄ at 2767 cm⁻¹. The spectrum

showcases that dissociation occurs by loss of one or two CH₄ ligands, and that shows that parent ions with similar masses (the ⁶³Cu and ⁶⁵Cu isotopes) are dissociated.

2.3.2 Electronic Photodissociation Spectroscopy

Upon observation of dissociation products at a fixed wavelength (usually using an oscilloscope to confirm photodissociation is occurring), we use the *Breakout Box Laser* program (Section 2.2.2) to scan the photodissociation laser to measure the photodissociation spectrum. As mentioned in Chapter 1, we typically study molecules that undergo indirect photodissociation (predissociation). This usually leads to a vibrationally and sometimes even rotationally resolved spectrum. When this is the case, the electronic spectrum can give information about the vibrational modes, quantum numbering, and bond energies. In addition, a partially rotationally resolved spectrum can give useful information about rotational constants and the molecular geometry. Thus, electronic photodissociation spectroscopy provides information about the excited electronic states and the symmetry of the excited state, as well as the upper limits for binding energies. Sometimes, it may even provide binding energies with high precision as in the case of our group's study of Co⁺(H₂O) and its isotopomers.⁵³ Electronic spectroscopy of Mn⁺(H₂O) is discussed in detail in Chapter 3.

2.3.3 Vibrational Spectroscopy

IR spectroscopy primarily gives information about ground electronic states, such as the bonding characteristics and geometries of ions/clusters. The IR photodissociation laser is scanned in the C-H or O-H stretching region and when the laser wavelength is in resonance with a stretch the molecule will absorb the light. If the absorbed energy is enough to break any bond in the molecule, photodissociation occurs and fragment ions can be measured. Due to single IR photons only having relatively low

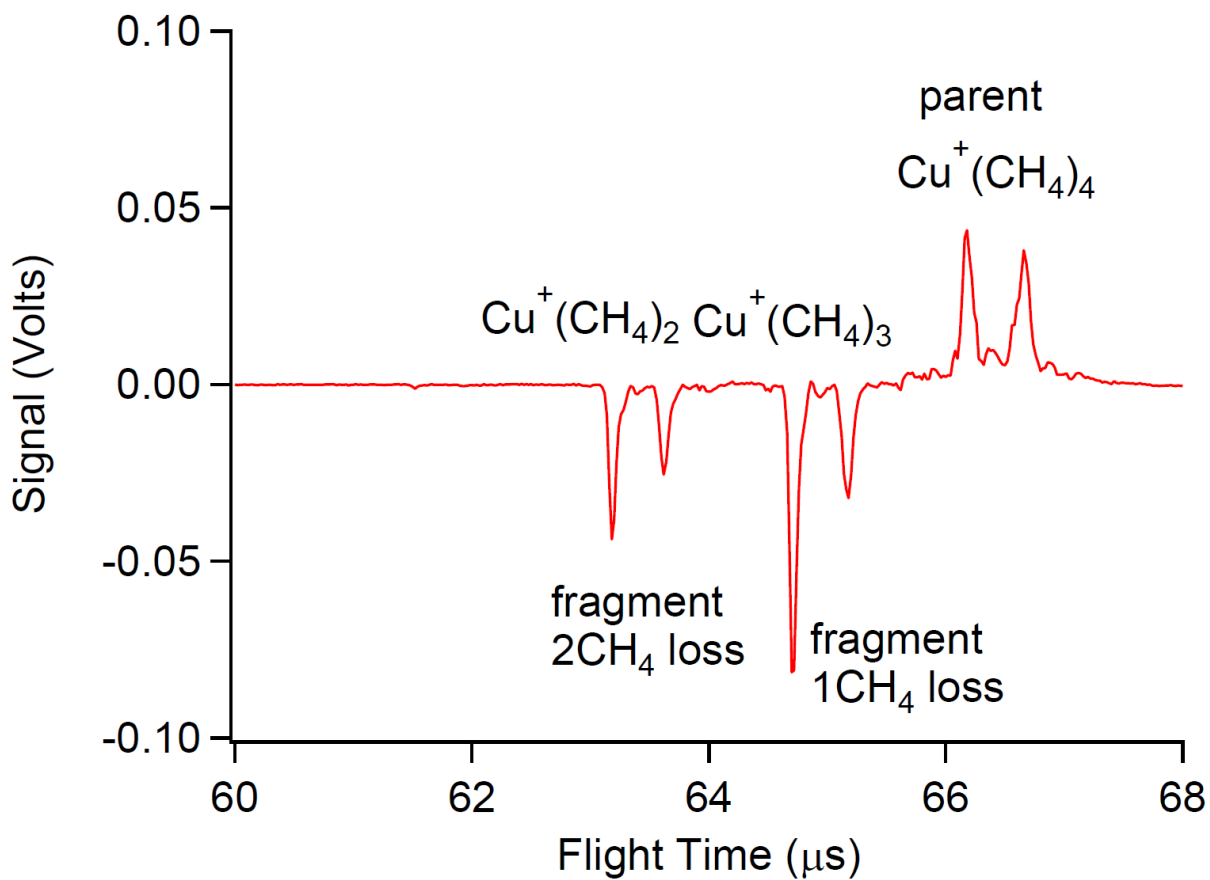


Figure 2.5 Difference Spectrum of $\text{Cu}^+(\text{CH}_4)_4$ with IR laser at 2767 cm^{-1} . Signal above zero indicates depletion (loss of parent here) and signal below zero indicates gain (fragment gain here). The doublets are due to the naturally occurring ^{63}Cu and ^{65}Cu isotopes.

energy ($\sim 3000 \text{ cm}^{-1} = 36 \text{ kJ/mol}$), photodissociation becomes less efficient if the bond strength is too great, as it requires infrared multiple photon dissociation (IRMPD). There are however, methods to overcome this limitation as vibrational spectroscopy can be applied in a couple of different ways.

2.3.3.1 IR Single Photon Dissociation (IRPD)

IRPD is the basic way technique used to measure vibrational spectra. In this method, the molecule's binding energy is weaker than the IR photon energy, so the molecule absorbs the light when the photon energy is in resonance with one of the vibrational frequencies and predissociates (**Figure 2.6**). Photodissociation does not necessarily occur at the bond that is absorbing the light. Instead, intramolecular vibrational redistribution (IVR) can occur on a sub-microsecond (and often sub-nanosecond) timescale, depending on the size of the molecule. In this case, photon energy is redistributed throughout the molecule, and the weakest bond breaks (predissociation). The photodissociation yield is generally high for IRPD if the vibration has a reasonable oscillator strength ($>5\%$ if oscillator strength $\approx 50 \text{ km/mol}$).

2.3.3.2 IR Multiple Photon Dissociation (IRMPD)

For molecules that have binding energies greater than that of a single IR photon, ($>\sim 3000 \text{ cm}^{-1}$) it will take more than one IR photon to photodissociate. However, several groups have developed or employed techniques to measure vibrational spectra of strongly bound molecules.³² One way to study them is through IR Multiple Photon Dissociation, in which several photons are absorbed by the molecule and thus the molecule can dissociate. (**Figure 2.6b**)⁵¹ In order for a molecule to photodissociate it must absorb enough photons so that their total combined energy is enough to break the weakest bond. IRMPD also requires the energy absorbed in the vibrational mode being excited to be easily distributed to other modes otherwise anharmonicity will lead to higher excitations of that vibration being out of resonance with the laser. A high density of vibrational states and anharmonicity enable the efficient Intramolecular Vibrational Redistribution (IVR) process. During our experiments, the vibrational spectrum of $\text{Fe}_3^+(\text{CH}_4)$ is measured with IRMPD (simply as a result of it not falling

apart from a single photon). Small molecules are expected to have lower density of vibrational states and hence low IVR rates. For these reasons, for small molecules with big binding energies, the IRMPD yield is very small, in most cases it is zero (<1%). In addition to low dissociation yield, power broadening and preferential dissociation of hotter ions often lead to a broad and unresolved IRMPD spectrum, which does not usually provide useful structural information. Use of the multi-pass mirror greatly improves the IRMPD yield. In our studies, the yield from the only ion that was too strong bound for single photon photodissociation, $\text{Fe}_3^+(\text{CH}_4)$, had a IRMPD yield of ~0.3%, as compared to single photon photodissociation yields which are typically 8-20%.

2.3.3 Argon Tagging

Another method of measuring the IR spectra of molecules with large binding energies is to tag them with an inert, weakly bound atom or molecule that does not greatly perturb the target molecule's vibrations. Since the atom is weakly bound, the absorption of a single photon will cause dissociation by loss of the atom or tagging molecule. The tagged molecule in most cases is argon and so the technique is called Argon-tagging.^{4, 26, 33, 72} There are two main requirements that make this technique effective vs standard IRMPD. The first is to have an Ar binding energy that is smaller than the IR photon energy so that it dissociates with one photon and doesn't require IRMPD, which is the main advantage. The second point is that the molecular vibrations are not greatly perturbed by the Ar, so the spectrum is mostly representative of the untagged molecule. Since in most cases, Ar binds very weakly, producing Ar-tagged ions requires that the ions be cold. Recall that the ions are produced and cooled to rotational temperatures of 8-15 K in the laser ablation source and subsequent expansion into vacuum. However, the vibrational temperature can be significantly higher. So, Ar-tagging also ensures that the ions' vibrations are very cold. Thus, the Ar-tagging spectrum gives much sharper and more intense peaks than IRMPD. Although Ar-tagging typically shifts vibrational frequencies by <10 cm^{-1} , it completely changes the rotational constants of the molecule, so its use precludes obtaining bond lengths and angles from the spectrum.

In our experiments, we tried Ar-tagging to measure vibrational spectra of $\text{Fe}_3^+(\text{CH}_4)$, but it was ineffective in this case due to lack of parent and thus the lack of tagged parent. The technique is very effective when many ions are available, as you typically tag ~10% of the parent. The high photodissociation yield of tagged molecules makes up for the reduced parent signal.

2.3.5 Vibrationally Mediated Photodissociation (VMP)

Now that we have discussed vibrational spectroscopy, which provides information about the vibrations of the ground state of a molecule, and electronic spectroscopy which details information about the vibrational and rotational information in the excited electronic states of a molecule, we can understand the combination of both techniques. By combining electronic and vibrational spectroscopy, a molecule's ground and excited states can be looked at in further detail. It also provides a means to measure the vibrational spectra of small, strongly bound molecules without tagging. The combination of these two types of spectroscopy is called Vibrationally Mediated Photodissociation (VMP) spectroscopy, and can be carried out in a few ways.⁸⁰ The general idea of these experiments is to change the molecule of interest's population in one state (from one ground state vibrational level to another), and then to observe the change in another state (excited state vibrational level).

One example of these double resonance experiments, and the one carried out in this work, is IR-UV hole burning or depletion spectroscopy shown in **Figure 2.7**. In this technique, the UV laser is parked on a wavelength that is in resonance with a transition to an electronic excited state of the molecule/ion. With the UV wavelength constant, the IR laser is scanned. The IR laser is fired slightly before (~20-40 ns) the UV laser. This is because the ions must be vibrationally excited before photodissociation occurs for this method to work.

If the IR laser is not in resonance with a vibration, a certain amount of photodissociation is observed due to the UV laser. When the IR is in resonance with a vibration, molecules are excited from $v''=0$ to $v''=1$ depleting the $v''=0$ population. This will lead to less total photodissociation, as the molecules in $v''=1$ are typically in resonance with an upper state at the UV laser frequency. This

leads to less dissociation at the wavelengths where ground state transitions occur (are in resonance) without having to do a vibrational photodissociation spectroscopy experiment to find them. Another VMP experiment would scan the UV laser while the IR laser is parked on a transition, to measure vibrational frequencies in the excited electronic state. However, as depletion is the simplest case and did not provide enticing results in this work, other techniques were not attempted. Vibrationally mediated photodissociation was used to measure O-H stretching frequencies in the ground state of $\text{Mn}^+(\text{H}_2\text{O})$ in Chapter 3.

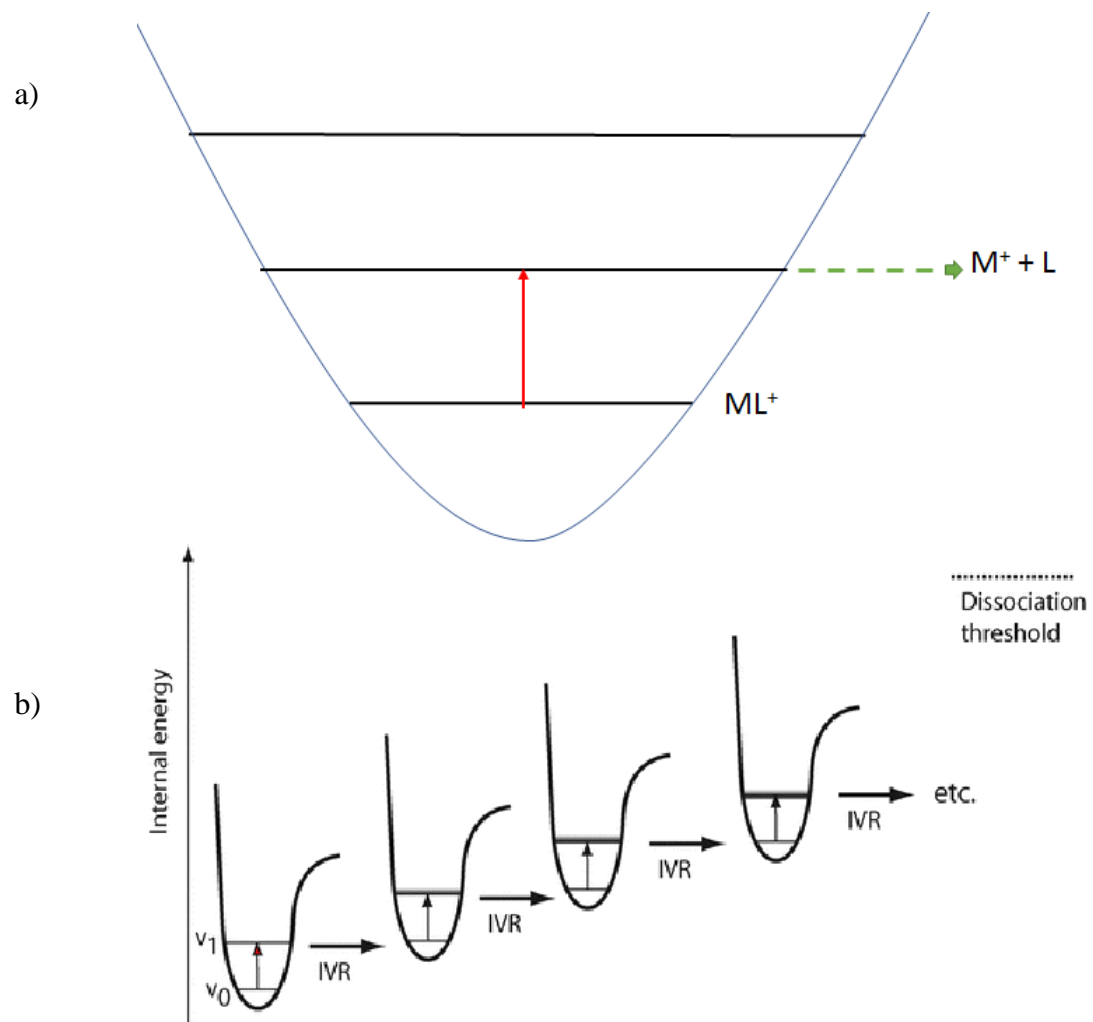


Figure 2.6: Illustration of techniques used in vibrational spectroscopy a) Infrared Predissociation b) Infrared Multiple Photon Dissociation (IRMPD)⁵¹

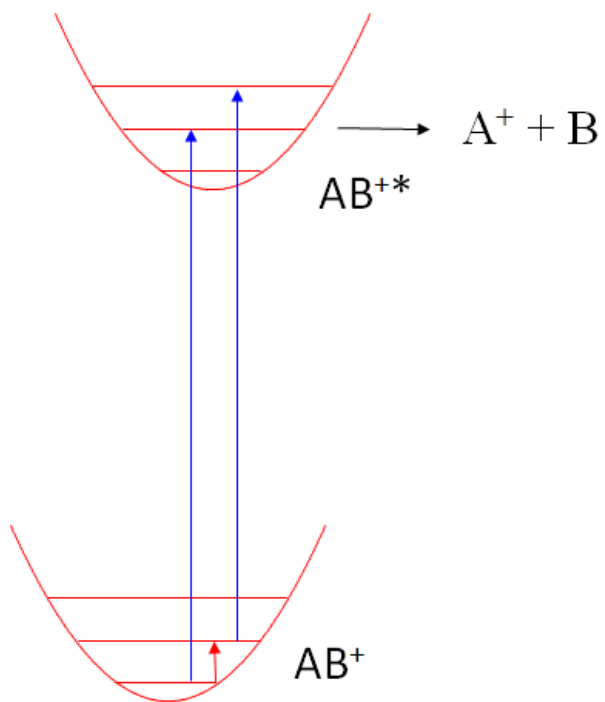


Figure 2.7 Illustration of the depletion double resonance technique, where the UV laser is parked (blue arrow) and the IR laser is scanned (red arrow). This causes depletion of the excited state when the IR laser is in resonance with a ground state transition.

References

1. Husband, J.; Aguirre, F.; Ferguson, P.; Metz, R. B. *J. Chem. Phys.* **1999**, *111*, 1433-1437.
2. Proch, D.; Trickl, T. *Rev. Sci. Instrum.* **1989**, *60*, 713-716.
3. Vučković, S.; Svanqvist, M.; Popok, V. N. *Rev. Sci. Instrum.* **2008**, *79*, 073303.
4. Wiley, W. C.; McLaren, I. H. *Rev. Sci. Instrum.* **1955**, *26*, 1150-1157.
5. Magnera, T. F.; David, D. E.; Michl, J. *J. Am. Chem. Soc.* **1989**, *111*, 4100-4101.
6. Alvarez-Galvan, M. C.; Mota, N.; Ojeda, M.; Rojas, S.; Navarro, R. M.; Fierro, J. L. G. *Catal. Today* **2011**, *171*, 15-23.
7. Gallagher, J. W.; Brion, C. E.; Samson, J. A. R.; Langhoff, P. W. J. *Phys. Chem. Ref. Data* **1988**, *17*, 9-153.
8. Rothman, L. S.; Jacquemart, D.; Barbe, A.; Benner, D. C.; Birk, M.; Brown, L. R.; Carleer, M. R.; Chackerian, C.; Chance, K.; Coudert, L. H.; Dana, V.; Devi, V. M.; Flaud, J. M.; Gamache, R. R.; Goldman, A.; Hartmann, J. M.; Jucks, K. W.; Maki, A. G.; Mandin, J. Y.; Massie, S. T.; Orphal, J.; Perrin, A.; Rinsland, C. P.; Smith, M. A. H.; Tennyson, J.; Tolchenov, R. N.; Toth, R. A.; Vander Auwera, J.; Varanasi, P.; Wagner, G. J. *Quant. Spec. Radiat. Transfer* **2005**, *96*, 139-204.
9. Citir, M.; Altinay, G.; Metz, R. B. *J. Phys. Chem. A* **2006**, *110*, 5051-5057.
10. Husband, J.; Aguirre, F.; Thompson, C. J.; Metz, R. B. *Chem. Phys. Lett.* **2001**, *342*, 75-84.
11. Kocak, A. Ph.D., University of Massachusetts. 2014.
12. Kocak, A.; Geoff, A.; Pearson III, W.; Altinay, G.; Metz, R. *J. Phys. Chem. A* **2013**, *117*, 1254-1264
13. Duncan, M. A. *Int. J. Mass Spectrom.* **2000**, *200*, 545-569.
14. Okumura, M.; Yeh, L. I.; Meyers, J. D.; Lee, Y. T. *J. Chem. Phys.* **1986**, *85*, 2328-2329.
15. Altinay, G.; Citir, M.; Metz, R. B. *J. Phys. Chem. A* **2010**, *114*, 5104-5112.
16. Corcelli, S. A.; Kelley, J. A.; Tully, J. C.; Johnson, M. A. *J. Phys. Chem. A* **2002**, *106*, 4872-4879.
17. Duncan, M. A. *Int. Rev. Phys. Chem.* **2003**, *22*, 407-435.
18. Rosenwaks, S., *Vibrationally Mediated Photodissociation*. Royal Society of Chemistry: Cambridge, UK, 2009; p 204.

CHAPTER 3

NEAR ULTRAVIOLET PHOTODISSOCIATION SPECTROSCOPY OF $\text{Mn}^+(\text{H}_2\text{O})$ AND $\text{Mn}^+(\text{D}_2\text{O})$

3.1 Introduction

These results have been published in *The Journal of Chemical Physics*.⁴⁶ As mentioned in Chapter 1, the importance of metal-water interactions in solvation, catalysis and biology has helped promote the study of metal-water complexes.¹¹ Due to the complexity of solution phase chemistry, the study of the intrinsic interaction between the metal and water is simplified by gas phase analysis. In particular with regard to this work, gas phase electronic spectroscopy experiments can reveal information about the effects on the metal's electronic configuration on the structure and bonding in the metal-water complex.

Magnera, David, and Michl⁶⁴ and Marinelli and Squires⁶⁵ first measured the binding energies of gaseous water molecules to first-row transition metal cations using collision induced dissociation (CID) in a triple-quadrupole mass spectrometer. Magnera et al. determined the binding energy of $\text{Mn}^+\text{-H}_2\text{O}$ to be 11400 cm^{-1} , while Marinelli and Squires found it to be 12900 cm^{-1} . These systems have been revisited in a guided-ion beam (GIB) measurement by Dalleska, Honma, Sunderlin and Armentrout, who obtained a binding energy of $9900 \pm 500\text{ cm}^{-1}$, making $\text{Mn}^+(\text{H}_2\text{O})$ the most weakly bound first-row transition metal water complex.²⁷ In fact, along the periodic table from left to right, the binding energies of the 1st row transition metals to water follow a slight downward trend from Ti^+ to a minimum at Mn^+ , before trending upward to Ni^+ and decreasing slightly to Cu^+ . This is primarily because the $3d^5 4s^1$ septet ground state of $\text{Mn}^+(\text{H}_2\text{O})$ is the highest spin state possible for these complexes. This leads to a less strongly bound complex than metals without electrons in the $4s$ orbital. An occupied $4s$ orbital leads to more metal-ligand repulsion than occupied $3d$ orbitals because the $4s$ is larger than the $3d$ and is spherical. Excitation of the $4p \leftarrow 4s$ transition results in strongly bound $3d^5 4p^1$ excited states. This differs from most $\text{M}^+(\text{H}_2\text{O})$ complexes, whose low lying excited states are

formed by $4s \leftarrow 3d$ transitions, and thus have excited states that are more weakly bound than the ground state. Due to the large difference in the $4s$ and $4p$ orbital energies, the excited states of $Mn^+(H_2O)$ are well above the dissociation energy, resulting in the clean observation of the transitions by photodissociation spectroscopy.

Electronic spectroscopy of $M^+(H_2O)$ facilitates the measurement of ground and excited state bond dissociation energies and rotational constants, and the excited electronic state vibrational frequencies. This information is used to determine the ground and excited electronic state's geometries, bonding characteristics, etc. There have been many spectroscopic studies of $M^+(H_2O)$ complexes including electronic spectroscopy of hydrated alkaline earth cations $Mg^+(H_2O)$,⁶⁸ $Ca^+(H_2O)$,^{50, 92} $Sr^+(H_2O)$ ³⁰ and transition metal cations $V^+(H_2O)$,^{60, 84} $Ni^+(H_2O)$,²⁸ $Co^+(H_2O)$ ⁵³ and $Zn^+(H_2O)$.¹ Vibrational spectra of $M^+(H_2O)$ reveals information about the metal ion's effect on O-H bonds in the H_2O ligand and can elucidate hydrogen-bonding networks in larger water clusters. Duncan and co-workers have used argon tagging to measure vibrational spectra of $M^+(H_2O)_n$ ($n=1-4$) ($M = Sc$,¹⁵ V ,¹⁰² Cr ,¹³ Mn ,¹⁴ Fe ,¹⁰⁴ Ni ,¹⁰⁵ Cu ,¹⁶ Zn)¹⁰ and $M^{2+}(H_2O)$ ($M = Sc$,¹⁵ V ,⁹ Cr ,¹³ Mn)¹⁴) in the O-H stretching region. Likewise, Nishi and co-workers measured vibrational spectra of $M^+(H_2O)_n$ for $M = V$,⁸³ Co ,³⁵ Cu and Ag ,⁴⁷ while Zhou and co-workers have used argon tagging to measure the vibrational spectra of $Au^+(H_2O)_n$ ($n=1-8$).⁶¹

In addition, van der Linde and Beyer have examined water activation in larger clusters of $M^+(H_2O)_n$ ($n < 40$) ($M = V, Cr, Mn, Fe, Co, Ni, Cu, Zn$) in a FT-ICR mass spectrometer, with particular emphasis on water activation in $Mn^+(H_2O)_n$.⁹⁹ O'Brien and Williams used vibrational spectroscopy to observe similar effects in smaller divalent clusters ($n=5-8$).⁷⁰ Rosi and Bauschlicher have investigated binding energies of $M^+(H_2O)_n$ ($n=1-4$) for transition metals from V to Zn .⁸¹ They calculate the structure of $Mn^+(H_2O)$ to be planar, with C_{2v} symmetry and note that due to the absence of $3d-4s$ hybridization, metal-water repulsion is reduced by polarization of the $4s$ orbital away from the water by $4s-4p$ hybridization. This structure has been confirmed in subsequent calculations by Trachtman et

al.⁹⁸ and Irigorias et al.⁴⁸ who also noted that the septet Mn^+ ion is not likely to accept donations from the water due to its highly stabilized exchange energy due to six matching spins. Calculations carried out in support of the vibrational spectra of $\text{Mn}^+(\text{H}_2\text{O})$ predict a binding energy of $10,600 \text{ cm}^{-1}$.¹⁴

The vibrational spectra of $\text{Mn}^+(\text{H}_2\text{O})$ and $\text{Mn}^{2+}(\text{H}_2\text{O})$ have been measured by Duncan and coworkers via argon tagging.¹⁴ Although the argon typically only slightly perturbs the O-H stretching frequencies, it strongly affects the rotational constants. Our group has used photodissociation spectroscopy and vibrationally mediated photodissociation (VMP) to measure the electronic spectra and O-H stretching frequencies of untagged $\text{Ni}^+(\text{H}_2\text{O})$ and $\text{Co}^+(\text{H}_2\text{O})$.^{28, 53} Those studies also measured the rotational constants ϵ and A for the ground and excited electronic states. These experiments extend electronic and vibrational spectroscopy studies to $\text{Mn}^+(\text{H}_2\text{O})$ and $\text{Mn}^+(\text{D}_2\text{O})$ complexes.

3.2 Experimental Methods

Experiments were carried out on a laser ablation dual time-of-flight reflectron mass spectrometer described in earlier papers,^{43, 67} with all programs and instruments involved described extensively in Chapter 2 of this work. Manganese ions are produced by ablating a manganese rod with the 532 nm second harmonic of a pulsed Nd:YAG laser operating at 17 mJ/pulse at a repetition rate of 20 Hz. The Mn^+ interacts with a gas mix of 2-10% H_2 and 90-98% He at a pressure of 35 psi, that runs through a bubbler filled with purified H_2O or D_2O . The mixture is introduced through a piezoelectric valve into the chamber resulting in the formation of $\text{Mn}^+(\text{H}_2\text{O})$ and larger clusters. The molecules then expand into vacuum forming a beam with a rotational temperature of $\sim 15\text{K}$.⁵³ The ion beam passes through a skimmer into the time-of-flight mass spectrometer, where the ions are accelerated, re-referenced to ground potential and mass selected. At the turning point of the reflectron, the frequency-doubled output of a tunable dye laser is used to photodissociate the ions. The fragment and remaining parent ions are reaccelerated and strike a microchannel plate detector in the final stage of the time-of-flight mass spectrometer. The signal is amplified and collected on an oscilloscope and gated integrators (controlled by an inhouse *LabView* program for data acquisition) and mass analyzed. A

photodissociation spectrum is formed by plotting the ratio of Mn^+ fragment ions to $\text{Mn}^+(\text{H}_2\text{O})$ or $\text{Mn}^+(\text{D}_2\text{O})$ parent ions and normalizing it to laser power as a function of the wavelength.

Although loss of H_2O is expected and observed to be the primary photodissociation pathway, loss of H atom and H_2 are energetically accessible above 23800 and 27400 cm^{-1} respectively. Difference (laser on - laser off) mass spectra of $\text{Mn}^+(\text{H}_2\text{O})$ taken at several wavelengths show that H atom loss is $\leq 20\%$ of H_2O loss while no H_2 loss is detected. Loss of D from $\text{Mn}^+(\text{D}_2\text{O})$ is even smaller, $< 5\%$ of D_2O loss. Photodissociation spectra are obtained by monitoring loss of water (Mn^+), as the other channels are too small and too close to the parent.

These electronic spectroscopy studies utilize the frequency-doubled output of a Continuum ND6000 dye laser at a line width of 0.1 cm^{-1} using a variety of laser dyes to scan the 270-360 nm range. The photodissociation yield is linear with laser power, up to $\sim 2\text{-}3$ mJ/pulse. As a result, the unfocused UV laser beam is attenuated to < 3 mJ/pulse to reduce power broadening and faithfully reproduce spectral intensities. The dye laser wavelength is calibrated using the optogalvanic spectrum of neon.¹¹³ The infrared spectroscopy experiments employ a Laser Vision IR OPO/OPA tunable from 2200 cm^{-1} to > 4000 cm^{-1} . This laser produces 10 mJ/pulse at ~ 3500 cm^{-1} , with a line width of ~ 2 cm^{-1} . It is calibrated using the absorption spectrum of water vapor in this case. A multipass mirror arrangement allows the IR laser to make up to 11 passes through the ion cloud. However the UV beam only makes one pass through the ion cloud due to absorption by the mirrors.²² The computations use the *Gaussian 09* suite of programs.³⁴ The geometries, energies, and vibrational frequencies of the ground and excited states of $\text{Mn}^+(\text{H}_2\text{O})$ and $\text{Mn}^+(\text{D}_2\text{O})$ are calculated with the B3LYP hybrid density functional with the 6-311++G(3df,3pd) basis set. The ground state geometry is also calculated at the CCSD(T)/aug-cc-pVTZ level.

3.3 Results and Discussion

3.3.1 Electronic Spectroscopy

Photodissociation spectra of $\text{Mn}^+(\text{H}_2\text{O})$ and $\text{Mn}^+(\text{D}_2\text{O})$ are measured from 30000 to 35000 cm^{-1} as shown in **Figure 3.1**. A full scan of 27000-38000 cm^{-1} revealed no additional dissociation. The photodissociation spectrum has transitions to two excited electronic states, each with well-structured vibrational features. In addition, the spectrum of $\text{Mn}^+(\text{H}_2\text{O})$ shows partially resolved rotational structure.

To assign the spectra, the possible motions of the complex are first considered. $\text{Mn}^+(\text{H}_2\text{O})$ has six vibrations, three of which essentially belong to H_2O : the symmetric and antisymmetric O-H stretches and the H-O-H bend. There are also three low frequency vibrations: the $\text{Mn}^+-\text{H}_2\text{O}$ stretch and two $\text{Mn}^+-\text{H}_2\text{O}$ bends. The vibrational modes and their quantum numbers are assigned with the aid of the spectrum of the deuterated molecule. Deuteration should significantly alter the frequency of the water stretches and bend, and of the intermolecular bends, but should have little effect on the metal-ligand stretching frequency, as this vibration primarily involves heavy atom motion. The primary vibrational progression shows very similar frequencies of $\sim 460 \text{ cm}^{-1}$ in $\text{Mn}^+(\text{H}_2\text{O})$ and $\sim 440 \text{ cm}^{-1}$ in $\text{Mn}^+(\text{D}_2\text{O})$. This confirms that the primary vibration observed is due to the metal-water stretch (ν_3).

Isotopic substitution also confirms the assignment of the band origins for the two excited electronic states: at $\sim 30250 \text{ cm}^{-1}$ and $\sim 32300 \text{ cm}^{-1}$ respectively. These excited state progressions are due to $\text{Mn}^+(\text{H}_2\text{O})$ with the metal in its $3d^5 4p^1$ state. The manganese ion's interaction with H_2O splits the degeneracy of the $4p$ orbital into three components: p_x , p_y and p_z . **Figure 3.2** shows the molecular axis system and **Figure 3.3** shows the relevant molecular orbitals. Looking at the available orbitals, one would expect the electronic spectrum of $\text{Mn}^+(\text{H}_2\text{O})$ to consist of three bands, transitions to the nearly degenerate p_x and p_y , along with a transition to the p_z orbital at significantly higher energy. This is supported by TD-DFT calculations, which predict vertical excitation energies of 32600 cm^{-1} to the ${}^7\text{B}_2$ (p_y) state, 34330 cm^{-1} to the ${}^7\text{B}_1$ (p_x) state and 38360 cm^{-1} to the ${}^7\text{A}_1$ (p_z) state. The p_y orbital is least

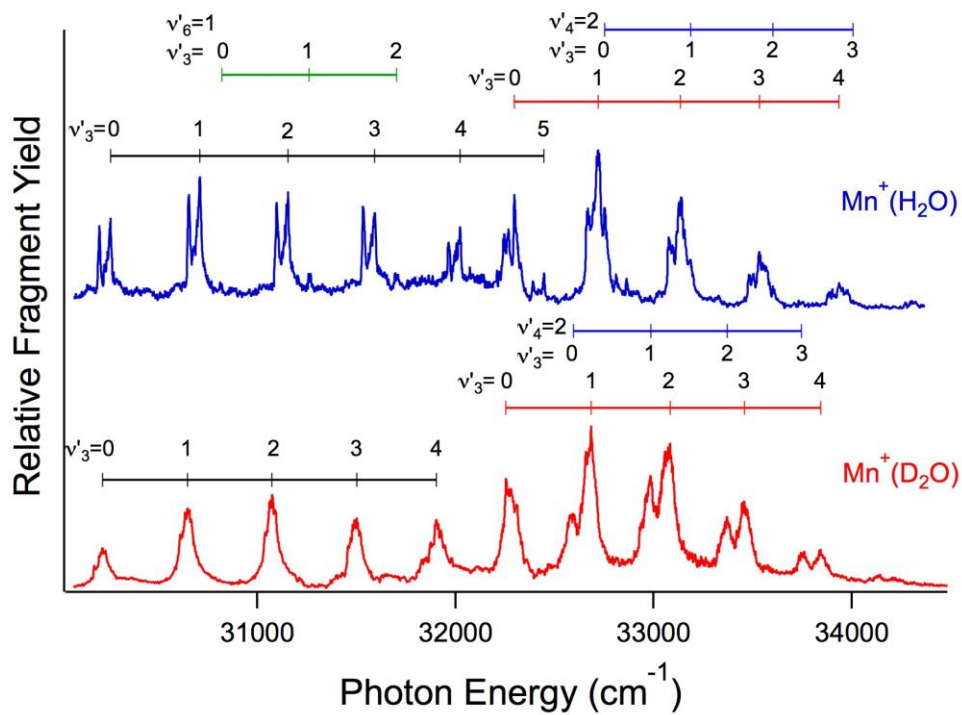


Figure 3.1 Photodissociation spectra of $\text{Mn}^+(\text{H}_2\text{O})$ and $\text{Mn}^+(\text{D}_2\text{O})$ from 30,000 to 35,000 cm^{-1} . An extended progression is observed in the Mn-ligand stretch (v_3'), in conjunction with short progressions in the in-plane bend (v_6') and out-of-plane bend (v_4'). The $v_6'=1$ progression is minor in intensity compared to the other vibrational modes.

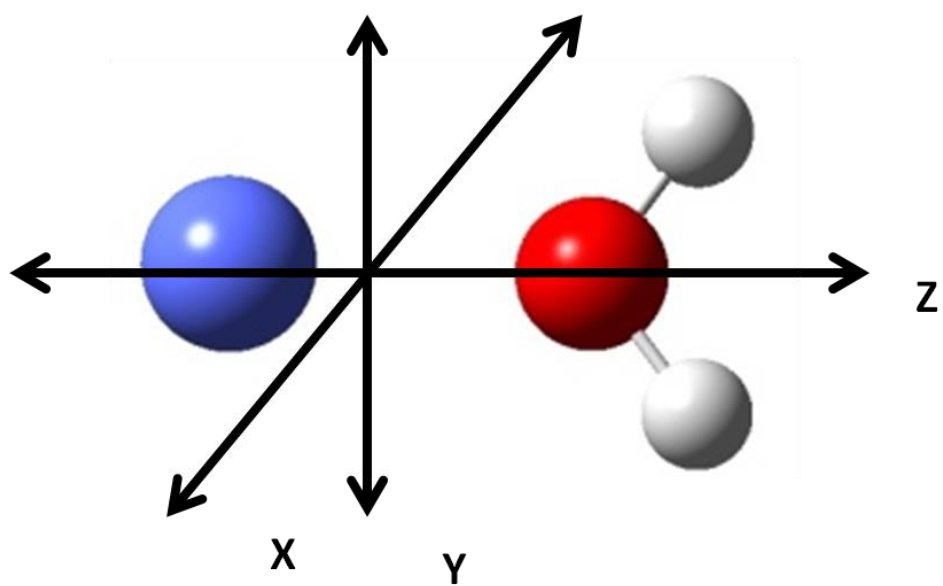


Figure 3.2 Rotational axis diagram of $Mn^+(H_2O)$

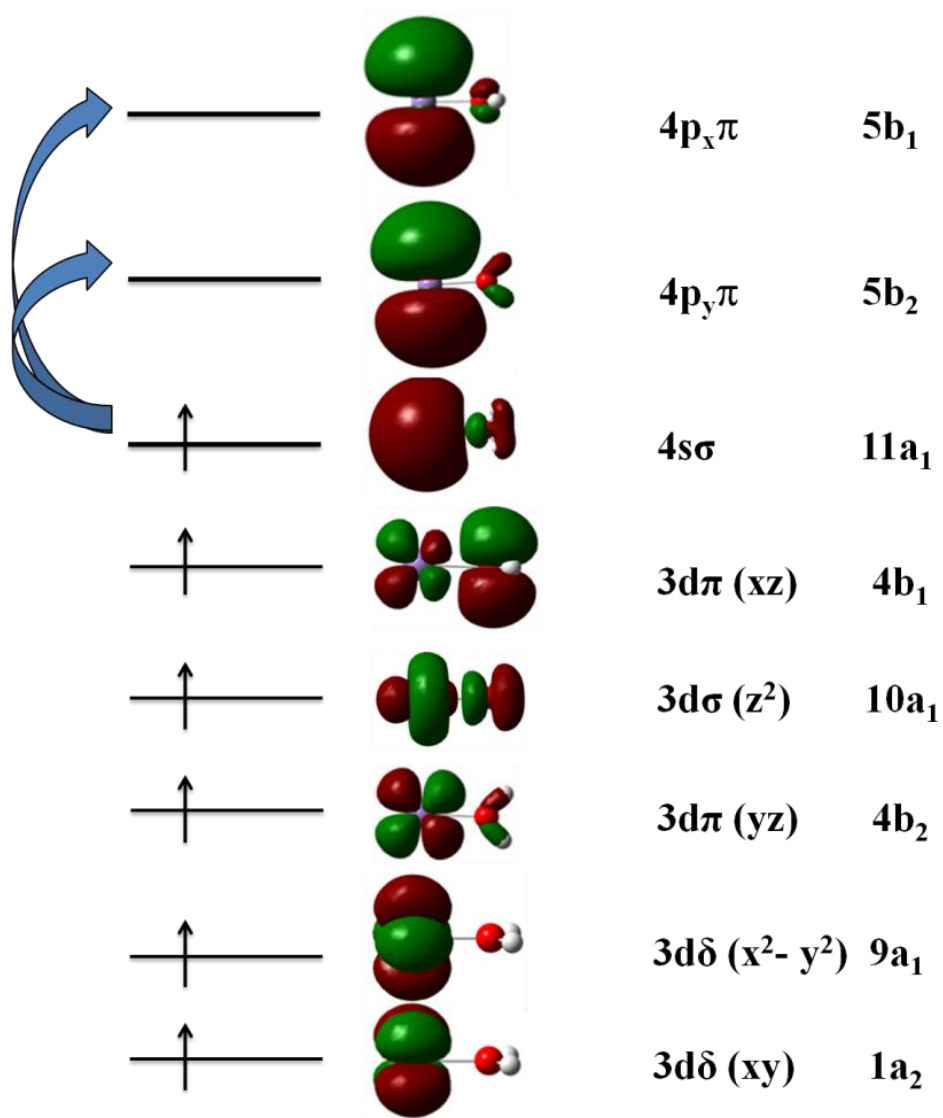


Figure 3.3 Molecular orbital diagram and electron occupancy of $Mn^+(H_2O)$ ($X, ^7A_1$)

repulsive. Thus, the lowest energy band is due to a transition from the ${}^7A_1(3d^54s)$ ground state to the ${}^7B_2(3d^54p_y)$ excited state. The p_x is slightly more repulsive as it overlaps the lone pair orbital on the oxygen. This transition ${}^7B_1(3d^54p_x) \leftarrow {}^7A_1(3d^54s)$ is responsible for the second band seen in Figure 3.1. Lastly, the p_z orbital is the most repulsive as it points directly at the ligand. Therefore, it is expected that the transition will have the highest energy. However, this transition is not observed, due to either being at a higher energy than 38000 cm^{-1} or a large change in geometry leading to very broad spectra. Although similar $p_x, p_y \leftarrow s$ transitions have been observed in $Mg^+(H_2O)$, $Ca^+(H_2O)$ and $Zn^+(H_2O)$, the $p_z \leftarrow s$ has not.^{1, 92, 112} This may be because the transition is too broad, or too high in energy.

In the spectra, there are also short progressions in two other intermolecular vibrations. Their assignment is facilitated by considering the rotational structure. The electronic transition moment from the $4s$ to the $4p_x$ and $4p_y$ orbitals lies perpendicular to the Mn-O axis. $Mn^+(H_2O)$ is a near prolate symmetric top, with a very small moment of inertia for rotation about the Mn-O axis (and hence relatively large rotational constant $A \approx 14\text{ cm}^{-1}$); the B and C constants are nearly equal and much smaller ($\sim 0.25\text{ cm}^{-1}$). So, transitions to final states that have A_1 vibrational symmetry will show perpendicular rotational structure, with $\Delta K_a = \pm 1$. At the $\sim 15\text{K}$ temperature of the molecular beam, three main peaks in the rotational substructure are expected, corresponding to $K_a' = 1 \leftarrow K_a'' = 0$ and $K_a' = 0, 2 \leftarrow K_a'' = 1$. This is observed for the metal-ligand stretch progression. Small features with parallel rotational structure ($\Delta K_a = 0$) due to the in-plane bend (ν_6) alone and in combination with the M^+-H_2O stretch are observed in the 7B_2 state starting at 30816 cm^{-1} . The out-of-plane bend (ν_4) is seen in the 7B_1 state of both $Mn^+(H_2O)$ and $Mn^+(D_2O)$ starting at 32753 and 32591 cm^{-1} respectively and also in combination with the M^+-H_2O stretch. Each of the three observed vibrations will be analyzed in turn.

To better characterize the metal-ligand stretching interaction, the peak positions are fit to the energy levels of a Morse oscillator (Equation 3-1).

$$E = T_e + \omega_3'(v_3' + 1/2) - \chi_3'(v_3' + 1/2)^2 \quad 3-1$$

Here, ω_3' is the fundamental frequency, v_3' the vibrational quantum number, and χ_3' the anharmonicity constant. First and second excited state frequencies of $\omega_3' = 459 \text{ cm}^{-1}$ and 430 cm^{-1} are determined with anharmonicities of $\chi_3' = 3.5 \text{ cm}^{-1}$ and 4.1 cm^{-1} respectively. The ground and excited state values are also obtained at the B3LYP/6-311++G(3df,3pd) level. **Table 3-1** summarizes these vibrational frequencies for $\text{Mn}^+(\text{H}_2\text{O})$ and $\text{Mn}^+(\text{D}_2\text{O})$. To further complete the picture, the binding energies of $\text{Mn}^+(\text{H}_2\text{O})$ excited states are also calculated. The ground state of Mn^+ is $3d^54s^1 (^7S_3)$; the lowest allowed This is mainly due to a different anharmonicity constant being calculated depending on what vibrational states are used to calculate it (e.g. the ones encompassed in first 15% of dissociation energy vs. the last 15% will likely have different constants). It is apparent when looking at equation 3-1 how this change in the anharmonicity constant will affect the resulting calculated dissociation energy.

The relative intensities of the vibrational features in the photodissociation spectrum reflect the change in geometry upon electronic excitation. To quantify this, the one-dimensional Schrödinger equation for the Mn-(H₂O) stretch is solved. Treating the ground and excited electronic states as Morse oscillators, the vibrational (Franck-Condon) overlaps are calculated while varying the upper state Mn-O bond length. For the ground state, these calculations use the B3LYP/6-311++G(3df,3pd) bond length of 2.180 \AA , Mn⁺-O stretching frequency of 309.7 cm^{-1} and experimental dissociation energy. For the excited states, experimental frequencies and anharmonicities are used and the bond length is varied until the calculated intensities match the experiment. The bond length was found to be $r_e = 2.030 \pm 0.015 \text{ \AA}$ for the first excited state of $\text{Mn}^+(\text{H}_2\text{O})$ and $2.040 \pm 0.01 \text{ \AA}$ for the second excited state. The $3p \leftarrow 4s$ excitation leads to a reduction in the Mn-O bond length of $\sim 0.15 \text{ \AA}$. This is slightly larger than the $\sim 0.13 \text{ \AA}$ shortening observed for the analogous transition in $\text{Zn}^+(\text{H}_2\text{O})$ and 0.09 \AA in $\text{Ca}^+(\text{H}_2\text{O})$.^{1,92} The bond length decrease is due to repulsion between the electron in the singly occupied $4s$ orbital and the lone pairs on the oxygen. Promotion of this electron to the $4p_x$ or $4p_y$ orbital, both of which are perpendicular to the ligand, reduces this repulsion and leads to a shorter, stronger Mn⁺-H₂O

Calculated and Measured Vibrational Frequencies (cm ⁻¹) of Mn ⁺ (H ₂ O) and Mn ⁺ (D ₂ O)								
Calculated (B3LYP/6-311++G(3df,3pd))								
			Mn ⁺ (H ₂ O)			Mn ⁺ (D ₂ O)		
mode (v _i)	Vibrational Symmetry	Description	Ground State	⁷ B ₂	⁷ B ₁	Ground State	⁷ B ₂	⁷ B ₁
1	a ₁	O-H symmetric stretch	3720	3744	3723	2680	2695	2684
2	a ₁	H-O-H bend	1644	1624	1650	1206	1193	1210
3	a ₁	M-O stretch (z)	310	463	427	297	443	411
4	b ₁	Out-of-plane bend (x)	320 (361)	357 (257)	280 (106) ^d	245 (270)	269 (183)	213 (55) ^e
5	b ₂	O-H antisymmetric stretch	3802	3799	3790	2789	2788	2779
6	b ₂	In-plane bend (y)	494 (493)	548 (533)	660 (584)	366 (367)	408 (398)	487 (435)
Experimental								
mode (v _i)	Vibrational Symmetry	Description	Ground State	⁷ B ₂	⁷ B ₁	Ground State	⁷ B ₂	⁷ B ₁
3	a ₁	M-O stretch (z)	-	459 ^a	430 ^b	-	436	404
4	b ₁	Out-of-plane bend (x)	-	-	456 ^c	-	-	306 ^c
5	b ₂	O-H antisymmetric stretch	3656	-	-	-	-	-
6	b ₂	In-plane bend (y)	-	559	-	-	-	-

Table 3-1: Calculated and Measured Vibrational Frequencies (cm⁻¹) of Mn⁺(H₂O) and Mn⁺(D₂O). ^aχ₃'= 3.5, ^bχ₃'= 4.1, ^cv=0-2 spacing, ^dThis vibration is anharmonic, the value shown is the 0-1 spacing; the 0-2 spacing is 364 cm⁻¹, ^e The value shown is the 0-1 spacing; the 0-2 spacing is 240 cm⁻¹. Values in parentheses are ν₀ and are obtained by numerically solving the 1D Schrodinger equation, for a scan along this coordinate.

bond. Morse potential curves for the ground and excited states observed are shown in **Figure 3.4**.

As shown in **Table 3-1**, the calculated TDDFT harmonic frequencies for the Mn-H₂O stretch in the excited states are surprisingly close to the experimental frequencies, differing by <1%. In addition, the calculated Mn-O bond lengths are also in good accord with experiment (**Table 3-2**). As previously mentioned, the in-plane bend (ν_6') is observed for Mn⁺(H₂O) in the first excited state, and the out-of-plane bend (ν_4') for Mn⁺(H₂O) and Mn⁺(D₂O) in the second excited state. The in-plane bend is observed due to vibronic coupling, while the out-of-plane bend results from a geometry change along that mode. A consequence of vibronic coupling is that only one quantum of in-plane bend is observed, whereas only transitions to even quanta are seen for the out-of-plane bend. The in-plane bend (ν_6') is observed in the first excited state, starting 559 cm⁻¹ after the origin, and then in combination with the metal-ligand stretch. This result is very close to the calculated harmonic frequency of 548 cm⁻¹. Both the in-plane bend and p_y orbital have B₂ symmetry. Their symmetry product, A₁, indicates a vibronically allowed transition and appears as a parallel band. The analogous, vibronically allowed transition is also observed in Zn⁺(H₂O), at 700 cm⁻¹.¹ In Mn⁺(D₂O) the in-plane bend is predicted to lie at 408 cm⁻¹. It is thus obscured by the much more intense metal-ligand stretch at 436 cm⁻¹.

Transitions to two quanta of the out-of-plane bend (ν_4') are seen in the second excited state of both Mn⁺(H₂O) and Mn⁺(D₂O). Transitions to even number of quanta in ν_4' show perpendicular rotational structure. These peaks are clearly observed in Mn⁺(D₂O) and give $2\nu_4'=306$ cm⁻¹. In the Mn⁺(H₂O) spectrum, $2\nu_4' = 456$ cm⁻¹ is only ~26 cm⁻¹ larger than ν_3' . As a result, the multiplet structure of transitions to states with $\nu_4'=2$ and $\nu_3'=n$ overlap multiplets with $\nu_4'=0$ and $\nu_3'=n+1$ convoluting the spectrum. Transitions to one quantum of ν_4' are vibronically allowed for the second excited state and would show parallel structure, but they are not observed in this case, although they

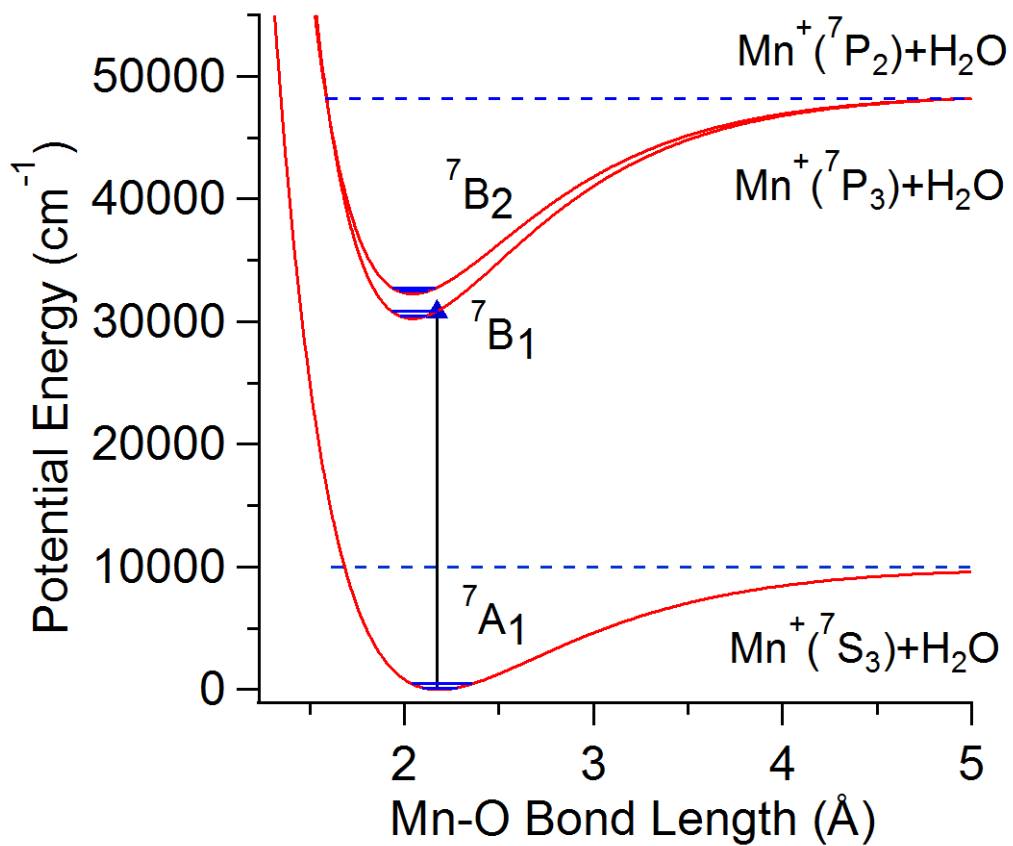


Figure 3.4 Potential energy curves of the ground and excited electronic states of Mn⁺(H₂O) along the Mn-O stretch based on experiment.

Geometries of the Ground and Excited States of Mn⁺(H₂O)				
	Calculated, B3LYP/6-311++G(3df,3pd) or CCSD(T)/aug-cc-pVTZ			Experiment
Mn ⁺ (H ₂ O)	r _{MO} (Å)	<HOH (°)	r _{OH} (Å)	
Ground State	2.180	106.8	0.968	-
Ground State ^a	2.177	106.1	0.967	-
Excited State 1(4p _y) ⁷ B ₂	2.001	109.6	0.967	2.030 ± 0.015
Excited State 2(4p _x) ⁷ B ₁	2.040	107.0	0.969	2.040 ± 0.010

Table 3-2: Geometries of the Ground and Excited States of Mn⁺(H₂O). a) At the CCSD(T)/aug-cc-pVTZ level

are seen in $\text{Zn}^+(\text{H}_2\text{O})$ and $\text{Ca}^+(\text{H}_2\text{O})$.^{1,92} Time-dependent DFT calculations are carried out to further characterize the out-of-plane bend in the ground and excited electronic states of $\text{Mn}^+(\text{H}_2\text{O})$. The potentials are calculated by scanning the out-of-plane angle from 0 to 90° (keeping the Mn-O bond length and H-O-H angle fixed at the equilibrium value in the ground state) and then using TDDFT to find the total energy at that geometry.

As shown in **Figure 3.5**, the out-of-plane bend is harmonic for the ground state, but the second excited state has two equivalent minima at $\pm 38^\circ$, separated by a barrier of 154 cm^{-1} . Energies and wavefunctions of the excited states are calculated by solving the one-dimensional Schrödinger equation. For the second excited state of $\text{Mn}^+(\text{H}_2\text{O})$, $v_3'=1$ is predicted to lie 106 cm^{-1} above $v_3'=0$, with $v_3'=2$ at 364 cm^{-1} . This is slightly lower than the 456 cm^{-1} observed experimentally. The calculated values for $\text{Mn}^+(\text{D}_2\text{O})$ are similarly underestimated as seen in **Table 3-1**. In addition, the Franck-Condon factors calculated for $v_3'=2$ are smaller than is observed. This suggests that the TDDFT calculations underestimate the barrier to planarity.

The vibrational structure in the electronic spectrum of $\text{Mn}^+(\text{H}_2\text{O})$ reveals how the electron occupancy of the metal affects the bonding with the ligand. The ($3d^54s$) ground state of Mn^+ binds to water relatively weakly, forming a planar, C_{2v} complex with a calculated Mn-O bond length of 2.18 Å. The $3d^54p_y$ excited state has a much shorter bond length (2.03 Å) and a metal-ligand stretching frequency of 459 cm^{-1} , and retains the C_{2v} structure. In the second, $3d^54p_x$, excited state the bond is slightly longer (2.04 Å), the metal-ligand stretching frequency drops slightly to 430 cm^{-1} and the complex distorts out-of-plane. The electronic spectrum of $\text{Mn}^+(\text{H}_2\text{O})$ is quite similar to that of $\text{Zn}^+(\text{H}_2\text{O})$. This is not unexpected considering the similar electronic configuration of Mn^+ and Zn^+ : $3d^54s$ and $3d^{10}4s$ respectively. Both have long progressions in the metal-water stretch which are indicative of significant changes in bond length from the ground to the excited state. In the first excited state, both also show a vibronically allowed transition to the in-plane bend and in the second excited state a short progression in the out-of-plane bend, indicating a small barrier to planarity.

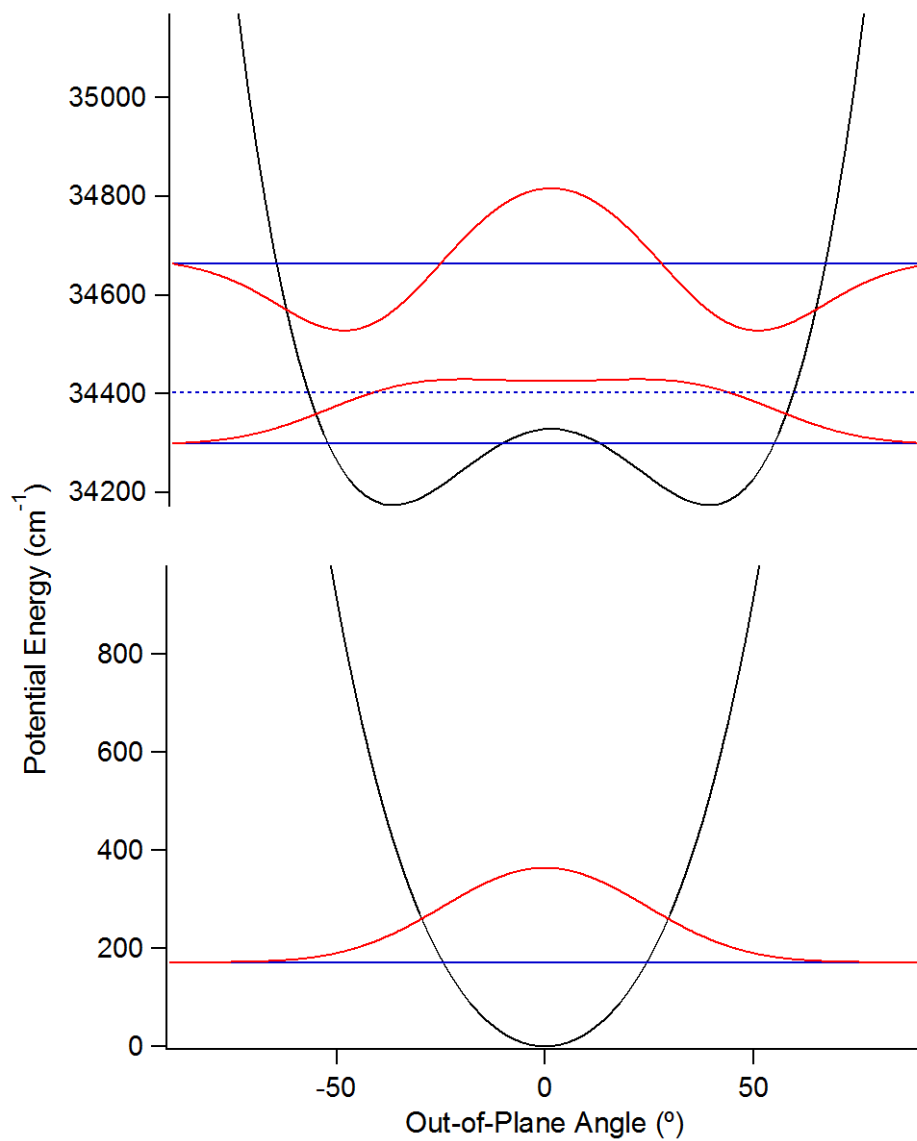


Figure 3.5 Scans along the out-of-plane bend mode in the ground and 7B_1 excited state showing the vibrational energy levels for $v_3''=0$ and $v_3'=0,1$ and 2 and the corresponding wavefunctions for states with even quanta.

The $\text{Zn}^+(\text{H}_2\text{O})$ system does show stronger, shorter bonds in the ground and excited electronic states, as would be expected considering the smaller ionic radius of zinc. For example, the calculated Zn-H₂O bond length of 2.07 Å in the ground state reduces to 1.95 Å and 1.98 Å in the excited states, and the vibrational frequencies of the excited states of $\text{Zn}^+(\text{H}_2\text{O})$ are ~15% higher than the corresponding states in $\text{Mn}^+(\text{H}_2\text{O})$. In the second excited state of $\text{Mn}^+(\text{H}_2\text{O})$, the 4p_x orbital on the metal overlaps the lone pair electrons on the oxygen. This is more repulsive than the interaction in the first excited state in which the 4p_y orbital is perpendicular to the oxygen lone pair. This repulsion leads to the p_x state lying ~2000 cm⁻¹ above the p_y state and having a slightly longer bond. The energy difference between these two states is small; a consequence of the metal's 4p orbitals being much larger than the oxygen atom's lone pair orbitals.

3.3.2 Electronic Spectroscopy: Rotations

Analysis of the rotational structure in the electronic transitions potentially provides information about the geometry of the molecule and the symmetry of the ground and excited states. In this analysis, $\text{Mn}^+(\text{H}_2\text{O})$ and $\text{Mn}^+(\text{D}_2\text{O})$ are treated as nearly symmetric prolate tops. The corresponding spectra's rotational structure are compared to simulations generated by the *spfit* and *spcat* programs⁷⁴ to determine the A', B' (B'≈C') rotational and ϵ_{aa}' and ϵ_{aa}'' spin rotational constants. The rotational Hamiltonian is expressed as the sum of purely rotational and spin-rotation terms:^{12, 96}

$$H = H_{rot} + H_{sr} \quad 3-2$$

with

$$H_{rot} = AN_a^2 + BN_b^2 + CN_c^2 \quad 3-3$$

$$H_{sr} = \frac{1}{2} \sum_{\substack{\alpha=a,b,c \\ \beta=a,b,c}} \epsilon_{\alpha,\beta} (N_\alpha S_\beta + S_\beta N_\alpha) \quad 3-4$$

where A, B and C are rotational constants, N is the rotational angular momentum, S is the spin angular momentum, and $\epsilon_{\alpha,\beta}$ are components of the spin rotation tensor in the inertial axis system (a,b,c). In the

absence of spin-rotational interaction the rotational energies (eigenvalues for H_{rot}) for a near-symmetric top are given by equation 3-5.

$$E_{J,K_a} = \left(A - \left(\frac{B+C}{2} \right) \right) K_a^2 + \left(\frac{B+C}{2} \right) J(J+1) \quad 3-5$$

The quantum numbers associated with rotations are the total angular momentum quantum number J , and K_a , the projection of the angular momentum onto the Mn-O bond (Figure 3.2). Rotation about the Mn-O bond has the smallest moment of inertia and hence the largest rotational constant, calculated to be $A'' \approx 14 \text{ cm}^{-1}$. The B and C constants are much smaller and are degenerate for a prolate top. They are nearly identical: $B'' \approx C'' \approx 0.24 \text{ cm}^{-1}$. As noted earlier, the K structure is apparent in the spectrum, but individual J peaks are not resolved. Although the spin-rotation interaction parameter ϵ has components along all three rotational axes, ϵ_{aa} dominates as the A rotational constant is much larger than B or C . The spin-rotation constant ϵ_{aa} adds two primary terms to the energies in equation 3-5.^{50, 110} One term is proportional to $\epsilon_{aa} K_a \Sigma$, ($\Sigma = -3, -2, -1, 0, 1, 2, 3$ is the projection of the electron spin angular momentum onto the a axis) which broadens peaks with $K_a \geq 1$. The second term is proportional to $\epsilon_{aa} K_a^2$, and affects the apparent A rotational constant. The shape of each $K_a' \leftarrow K_a''$ peak is determined by the spin-rotation constants in the upper and lower states, and to a lesser extent, by the change in the B and C rotational constants (ΔB , ΔC) upon electronic excitation. The simulations are also much more sensitive to ΔB than to the individual values of B' and B'' . Due to the limited resolution of the spectrum, some spectroscopic parameters could not be determined.

Calculated ground state rotational constants are used for the fit. First, equilibrium constants A_e'' , B_e'' and C_e'' are calculated at the CCSD(T)/aug-cc-pVTZ level. These values are then converted to $v=0$ constants A_0'' , B_0'' and C_0'' by adding the difference between equilibrium and $v=0$ constants from an anharmonic frequency calculation at the B3LYP/6-311++G(3df,3pd) level. Excited state terms A' , B' , ϵ_{aa}' and ground state ϵ_{aa}'' are varied until the generated spectrum best approximates the experiment. The temperature in the simulations is held at 15 K, as in the $\text{Ni}^+(\text{H}_2\text{O})$ and $\text{Co}^+(\text{H}_2\text{O})$ studies.^{28, 53} A

Lorentzian line width of 2 cm^{-1} is also used. This corresponds to an excited state lifetime of $\sim 2.5 \text{ ps}$. The results are seen in **Figure 3.6** with corresponding rotational parameters in **Table 3-3**.

Since hydrogen is a fermion, the overall wavefunction for $\text{Mn}^+(\text{H}_2\text{O})$ must be antisymmetric with respect to exchange of the hydrogens (which is equivalent to 180° rotation about the a-axis). The ground state of $\text{Mn}^+(\text{H}_2\text{O})$ is ${}^7\text{A}_1$ (symmetric), as is the vibrational wavefunction for $v''=0$. So, the product of the wavefunction for rotation about the a axis and the nuclear spin must be antisymmetric, which results in a 1:3 even:odd K_a'' population ratio, as molecules do not cool from $K_a''=1$ to $K_a''=0$ in the ion source.⁵³ Thus, the perpendicular bands in the spectrum of $\text{Mn}^+(\text{H}_2\text{O})$ appear as doublets, due to the $K_a'=0 \leftarrow K_a''=1$ and $K_a'=2 \leftarrow K_a''=1$ transitions. The $K_a'=1 \leftarrow K_a''=0$ transition lies between these features, but it is much less intense and, for most bands in $\text{Mn}^+(\text{H}_2\text{O})$, does not give a discrete peak. States with $K_a''>1$ have very low population at 15K and thus contribute little to the spectrum. As deuterium is a boson, $\text{Mn}^+(\text{D}_2\text{O})$ should have a 2:1 even:odd K_a'' ratio.⁵³ The spectrum should thus consist primarily of triplets, with a central $K_a'=1 \leftarrow K_a''=0$ peak bracketed by weaker $K_a'=0, 2 \leftarrow K_a''=1$ peaks (which are bracketed in turn by much weaker $K_a'=1, 3 \leftarrow K_a''=2$ peaks). However, the rotational structure in $\text{Mn}^+(\text{D}_2\text{O})$ is substantially broader than in $\text{Mn}^+(\text{H}_2\text{O})$, so the K structure is barely observable.

Comparing the ground to excited states in **Table 3-3**, the *A* constant decreases and the *B* and *C* constants increase during the transition. This increase in *B* and *C* is the result of the shortening of the Mn-O bond upon electronic excitation. The rotational simulations are relatively insensitive to *B* and *C*, so these constants were set to the values obtained from the intensities in the Mn-O stretch progressions: $\Delta r_{\text{mo}} = 0.15 \pm 0.015 \text{ \AA}$ ($B'=0.279 \pm 0.004 \text{ cm}^{-1}$) and $0.14 \pm 0.01 \text{ \AA}$ ($B'=0.277 \pm 0.003 \text{ cm}^{-1}$). For the planar complexes, the *A* constant depends on the O-H bond length and H-O-H angle. As the calculations predict that electronic excitation has an insignificant effect on r_{OH} (Table 3-2), the change in *A* is largely due to a change in the H-O-H angle. The observed $A' = 12.8 \pm 0.7 \text{ cm}^{-1}$ for the ${}^7\text{B}_2$ state corresponds to $\angle\text{HOH}$

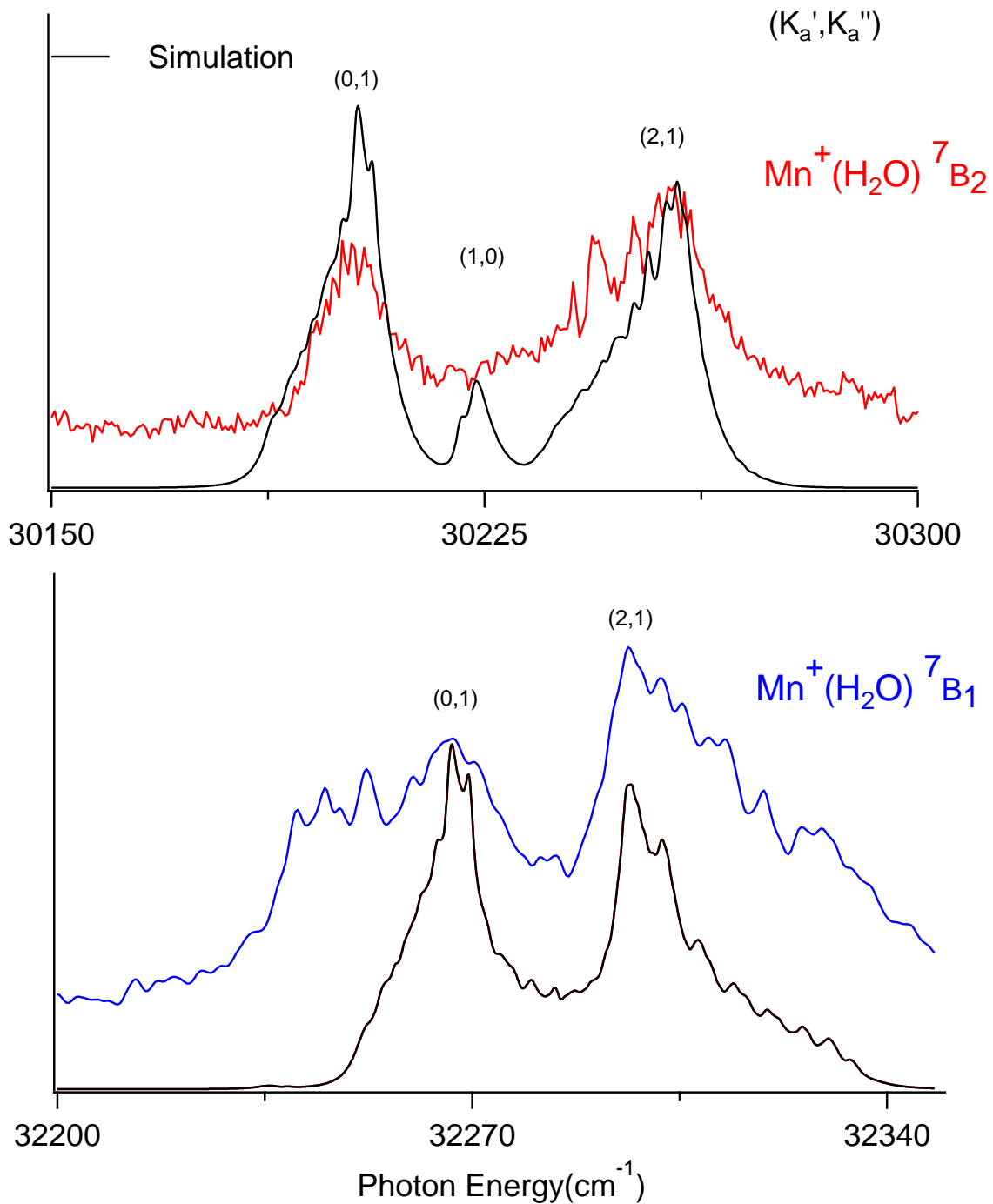


Figure 3.6 Photodissociation spectra of the origin band of the 7B_2 state (top) and 7B_1 state of $Mn^+(H_2O)$ (bottom) showing the $\Delta K_a = \pm 1$ features characteristic of a perpendicular transition. The simulated spectra are also shown, using the spectroscopic parameters in Table 3-3, a rotational temperature of 15 K, and a Lorentzian line width of 2 cm^{-1} .

Rotational Constants for Mn⁺(H₂O) (cm⁻¹)			
Constant	Ground State	⁷ B ₂ State	⁷ B ₁ State
T _o	0	30210	32267
A	13.81 ^a	12.8±0.7	12.8 ^b
B	0.243 ^a	0.279±0.05	0.277±0.05
C	0.239 ^a	0.275±0.05	0.273±0.05
ε _{aa}	-3±1	0.5±0.5	-4.2±0.7

Table 3-3: Rotational Constants for Mn⁺(H₂O) (cm⁻¹). a) Fixed to the calculated value, b) Fixed to the value in the ⁷B₂ state

= $112 \pm 4^\circ$. Fits of A and ϵ_{aa} are correlated as their effect on the energies is proportional to K_a^2 .

Therefore, the relatively large uncertainty in A includes the effects caused by also varying ϵ_{aa}' . For the 7B_1 state, the simulations do not reproduce the very broad $K_a'=0 \leftarrow K_a''=1$ peak in the origin band, and peaks with $v_3' > 0$ overlap those with $v_4'=2$. Given that A' should not differ to an appreciable extent between the two excited states, A' was fixed to its 7B_2 state value. This increase in the H-O-H angle for states with shorter metal ion-oxygen bonds has also been observed in $M^+(H_2O)$ ($M=Mg, Ca, Co, Ni, Zn$).^{1, 28, 53, 92, 112} In bare H_2O , the H-O-H angle is 104.5° . This is smaller than the tetrahedral angle (109.5°), due to repulsion between the O-H bonding electrons and the oxygen lone pairs. When a metal ion binds to water, it removes electron density from the oxygen lone pairs, which increases the H-O-H angle. For a given metal, this effect will be stronger the shorter the M-O bond is.

As seen above, the spin-rotation parameter plays an important role in the simulations. The spin-rotation parameter ϵ is determined by two factors.⁹⁶ For open-shell metal compounds, the dominant contribution is usually second-order interaction between spin-orbit coupling and the Coriolis interaction. There is also some contribution from coupling of the electron spin to the magnetic field due to molecular rotation. Whitham and Jungen developed a pure precession model to predict the spin-rotation interaction in the $p \leftarrow s$ excited states of $CaNH_2$.¹¹⁰ In this model, rotation about the a axis leads to mixing of the p_x and p_y orbitals, and hence of the B_1 and B_2 states. In addition to $CaNH_2$, it has been found to work quite well for $Mg^+(H_2O)$, $Ca^+(H_2O)$ and $Zn^+(H_2O)$. Solving for the resulting energies using perturbation theory, it predicts²⁸

$$\epsilon_{aa} \approx \frac{4AA^{SO}\Lambda^2}{\Delta E} \quad 3-6$$

Here A is the rotational constant, A^{SO} is the effective spin-orbit interaction constant of the metal atom in the molecule (this is typically ~85% of the value in the free atom), $\Lambda=1$ for a p_x or p_y orbital and ΔE is the energy difference between the B_2 and B_1 states.

In the ground states of $\text{Mg}^+(\text{H}_2\text{O})$, $\text{Ca}^+(\text{H}_2\text{O})$ and $\text{Zn}^+(\text{H}_2\text{O})$ the only unpaired electron is in an s orbital, so the corresponding atomic states have no spin-orbit coupling, and equation 3-6 predicts $\epsilon_{aa}''=0$. The measured spectra are consistent with this result.^{1, 92, 107} For $\text{Mn}^+(\text{H}_2\text{O})$ ϵ_{aa}'' is initially set to zero because the ${}^7\text{S}_3$ ground state of Mn^+ has no spin-orbit coupling. However, simulations using $\epsilon_{aa}''=0$ clearly do not reproduce the decreasing intensity to lower energy from 30259 to 30235 cm^{-1} seen in **Figure 3.6** (top) nor the decreasing intensity to higher energy starting at 32300 cm^{-1} as seen in **Figure 3.6** (bottom). Instead, the simulations predict roughly constant intensity in these regions. In addition, the experimental $\text{K}_a'=0 \leftarrow \text{K}_a''=1$ peaks are far too narrow for both states when compared to the simulations. A spin-rotation constant of $\epsilon_{aa}'' = -3 \pm 1 \text{ cm}^{-1}$ gives the best match between simulations and experiment. Septet $\text{Mn}^+(\text{H}_2\text{O})$ is more sensitive to ϵ_{aa} than doublet molecules. New simulations of the spectra of $\text{Ca}^+(\text{H}_2\text{O})$ and $\text{Zn}^+(\text{H}_2\text{O})$, with $\epsilon_{aa}'' = \pm 1 \text{ cm}^{-1}$ are nearly identical to those with $\epsilon_{aa}''=0$ and all are consistent with published experiments.^{1, 50, 92}

For $\text{Mn}^+(\text{H}_2\text{O})$, the spin-orbit interaction constant for the $3d^54p$ states of Mn^+ is 62 cm^{-1} , so $A^{\text{SO}} \approx 53 \text{ cm}^{-1}$, and $|\Delta E| = 2057 \text{ cm}^{-1}$ (from the spectrum). This predicts $\epsilon_{aa}' = \pm 1.3 \text{ cm}^{-1}$ for the ${}^7\text{B}_2$ and ${}^7\text{B}_1$ states, respectively. While not in quantitative agreement with the measured $\epsilon_{aa}' = +0.5$ and -4.2 cm^{-1} for the two states, it is qualitatively correct in predicting that the sign of ϵ_{aa}' will be different in the two states. The most distinctive sign of this is seen in the shapes of the $\text{K}_a'=2 \leftarrow \text{K}_a''=1$ peak, which tails to the red in the ${}^7\text{B}_2$ state and to the blue in the ${}^7\text{B}_1$ state (**Figure 3.6**). The relatively poor performance of the pure precession model for $\text{Mn}^+(\text{H}_2\text{O})$ is probably due to the small indirect spin-orbit contribution to ϵ (the Mn^+ atomic spin-orbit interaction constant is substantially smaller than in Ca^+ and Zn^+), while the high spin of the manganese complex increases the contribution from direct interaction of the electron spin with the magnetic field due to molecular rotation.

The rotational structure in the electronic spectra of the $\text{M}^+(\text{H}_2\text{O})$ complexes measured to date ($\text{M}=\text{Mg}, \text{Ca}, \text{Mn}, \text{Co}, \text{Ni}, \text{Zn}$) are all similar. Focusing on the transition metals, $\text{Mn}^+(\text{H}_2\text{O})$ undergoes

an allowed $p \leftarrow s$ transition, leading to a decrease in bond length, while the $\text{Co}^+(\text{H}_2\text{O})$ and $\text{Ni}^+(\text{H}_2\text{O})$ complexes undergo either $d \leftarrow d$ or $s \leftarrow d$ forbidden transitions, leading to greater repulsion and an increased bond length. Since rotational constants are strongly linked to the change in bond length, the A constant decreases from the ground state to the excited state in $\text{Mn}^+(\text{H}_2\text{O})$ and $\text{Zn}^+(\text{H}_2\text{O})$, with the opposite occurring for the $\text{Co}^+(\text{H}_2\text{O})$ and $\text{Ni}^+(\text{H}_2\text{O})$ systems. Likewise, the B and C constants increase for the Mn^+ and Zn^+ complexes upon electronic excitation and decrease for the Ni^+ and Co^+ systems. The excited electronic states show varying lifetimes for these systems as indicated by observed Lorentzian linewidths ranging from 0.6 cm^{-1} in $\text{Ni}^+(\text{H}_2\text{O})$ to 6 cm^{-1} in $\text{Zn}^+(\text{H}_2\text{O})$. The spin-rotation constant ϵ is zero or negative in the ground electronic state. As noted above, it is zero in $\text{Zn}^+(\text{H}_2\text{O})$, -3 cm^{-1} in $\text{Mn}^+(\text{H}_2\text{O})$, and significantly larger in $\text{Co}^+(\text{H}_2\text{O})$ and $\text{Ni}^+(\text{H}_2\text{O})$, (-6 and -12 cm^{-1} respectively). In the excited states, ϵ can take positive or negative values, with the largest magnitude observed, 10 cm^{-1} , in $\text{Zn}^+(\text{H}_2\text{O})$.

3.3.3 Vibrational Spectroscopy

Infrared spectroscopy studies were carried out to explore the effects of the metal on the O-H bonds in the complex's ground state and to try to provide direct measurement of the ground state ϵ_{aa}'' and A'' rotational constants without the involvement of the excited states. The vibrational spectrum of $\text{Mn}^+(\text{H}_2\text{O})$ has been measured by Carnegie et al. via argon tagging.¹⁴ Argon tagging, while expected to have only a small effect on the O-H stretching frequencies, completely changes the rotational structure. Vibrationally mediated photodissociation (VMP) is a tool which can be used to measure vibrational spectra of small, strongly bound ions without tagging, as detailed in Chapter 2 of this work. Our group has used VMP to measure the O-H stretching frequencies of $\text{Ni}^+(\text{H}_2\text{O})$ and $\text{Co}^+(\text{H}_2\text{O})$.^{28, 53} The simplest way to measure vibrational spectra using VMP is in a depletion experiment explained in greater detail in Chapter 2. A laser operating in the visible or UV is set to an electronic transition which leads to photodissociation of ground state ions, while a second, IR, laser scans across the O-H stretching region. When the frequency of the IR laser corresponds to a vibrational transition, the ions

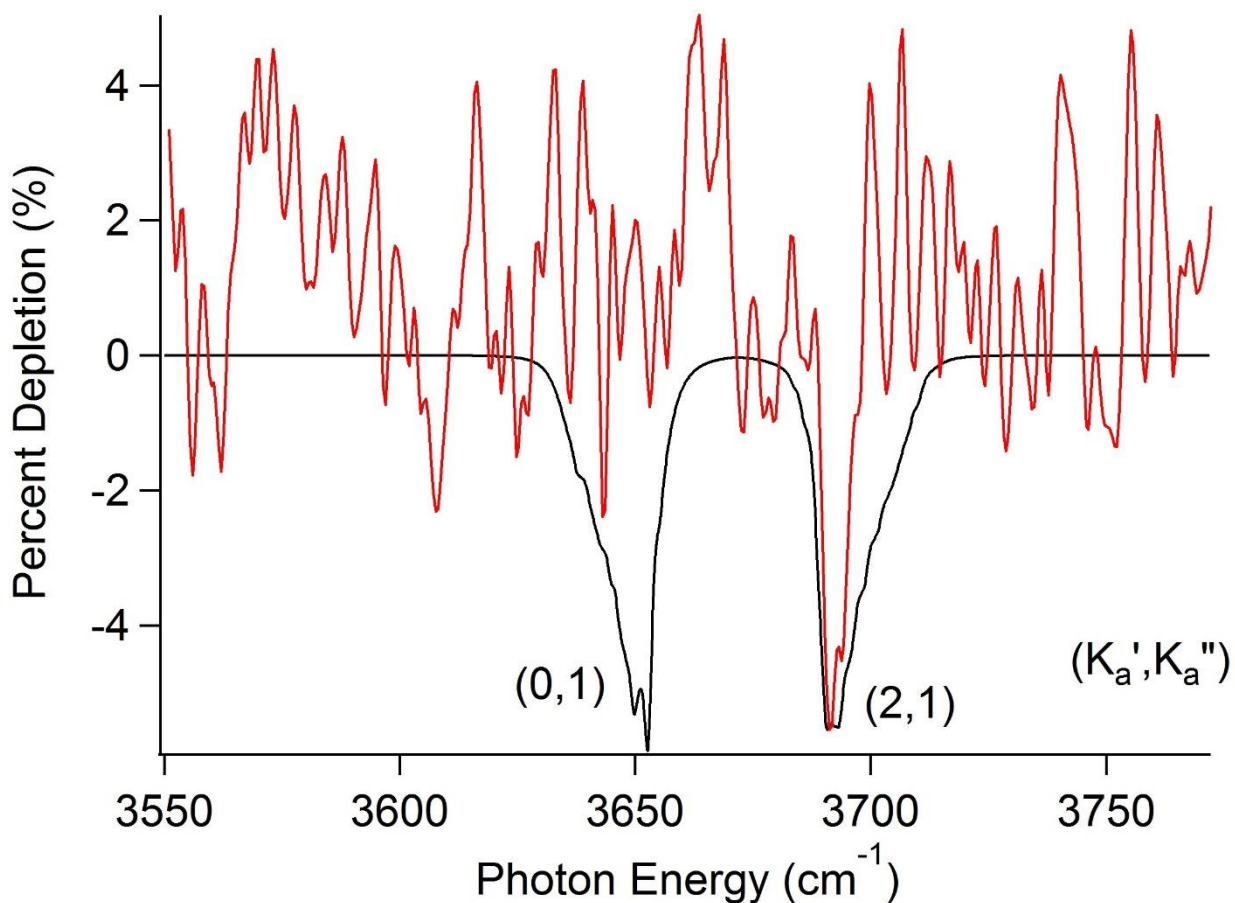


Figure 3.7: Vibration action spectrum of $\text{Mn}^+(\text{H}_2\text{O})$ in the O-H stretching region. The spectrum is obtained by monitoring depletion in the Mn^+ photofragment produced by irradiation of the $({}^7\text{B}_2 v_3'=1, K_a'=0) \leftarrow ({}^7\text{A}_1 v_3''=0, K_a''=1)$ transition at $30,655 \text{ cm}^{-1}$. This monitors molecules with $K_a''=1$. IR absorption removes molecules from $v''=0$, leading to a $\sim 5\%$ reduction in the fragment yield. A transition is observed to the antisymmetric O-H stretch v_5 near 3692 cm^{-1} (perpendicular band, $K_a'=2 \leftarrow K_a''=1$). The corresponding transition with $K_a'=0 \leftarrow K_a''=1$ is not observed, nor is the O-H symmetric stretch. A simulated spectrum is also shown using the spectroscopic parameters in Table 3-3 and with $v_5''=3658 \text{ cm}^{-1}$.

are vibrationally excited. If these vibrationally excited molecules are no longer in resonance with the UV laser, this will lead to less photofragment signal.

Depletion scans were carried out for $\text{Mn}^+(\text{H}_2\text{O})$, with the UV laser set to the $(v_3'=1, K_a'=0) \leftarrow K_a''=1$ transition at $30,655 \text{ cm}^{-1}$. A small amount of depletion ($\sim 5\%$) was consistently seen at $\sim 3692 \text{ cm}^{-1}$ as shown in **Figure 3.7**. Setting the UV to other lines with $K_a''=1$ led to smaller depletion in this region. Unfortunately, this was the only IR wavelength at which depletion was consistently observed, even when the UV laser was tuned to various transitions in the spectrum. The depletion experiment suffers from high background, which combines with shot to shot instability in the photofragment signal to give a noise level of $\sim 2\%$. In order to assign this transition we combine the O-H symmetric and anti-symmetric stretch frequencies measured by Carnegie et al. for $\text{Mn}^+(\text{H}_2\text{O})\text{Ar}$ ($v_1=3584 \text{ cm}^{-1}$ and $v_5=3660 \text{ cm}^{-1}$) with their calculated 2 cm^{-1} shift on argon tagging to predict $v_1=3582 \text{ cm}^{-1}$ and $v_5=3658 \text{ cm}^{-1}$.¹⁴ The VMP experiment monitors depletion from $K_a''=1$, so it is only sensitive to $K_a'=1 \leftarrow K_a''=1$ for the symmetric stretch, which is a parallel band, and to $K_a'=0,2 \leftarrow K_a''=1$ for the antisymmetric stretch, which is a perpendicular band. Simulations of the antisymmetric stretch using these frequencies and the ground state rotational constants in **Table 3-3** predict absorption at 3652 and 3692 cm^{-1} . The observed depletion at 3692 cm^{-1} thus clearly corresponds to $(v_5'=1, K_a=2) \leftarrow (v_5''=0, K_a''=1)$, implying $v_5=3658 \text{ cm}^{-1}$. Thus, binding to Mn^+ produces a 98 cm^{-1} red shift in the O-H antisymmetric stretching frequency of water, from 3756 to 3658 cm^{-1} .

3.3.4 Summary and Conclusions

In summary, the electronic spectra of $\text{Mn}^+(\text{H}_2\text{O})$ and $\text{Mn}^+(\text{D}_2\text{O})$ were measured from $30,000$ to $35,000 \text{ cm}^{-1}$ using photodissociation spectroscopy. The spectra show transitions to two excited electronic states, ${}^7\text{B}_2(3d^54p_y)$ and ${}^7\text{B}_1(3d^54p_x)$ with $T_0=30210$ and 32274 cm^{-1} respectively. The observed vibrations are assigned by comparing isotopic shifts between $\text{Mn}^+(\text{H}_2\text{O})$ and $\text{Mn}^+(\text{D}_2\text{O})$. These bands show long progressions in the Mn-O stretch with a frequency of $\sim 450 \text{ cm}^{-1}$ and partially resolved rotational structure. In combination with the guided ion beam measurement²⁷ of

the ground state $D_0(\text{Mn}^+-\text{H}_2\text{O}) = 9,900 \pm 500 \text{ cm}^{-1}$, a binding energy of $18200 \pm 500 \text{ cm}^{-1}$ for the ${}^7\text{B}_1(\text{p}_y)$ and $16200 \pm 500 \text{ cm}^{-1}$ for the ${}^7\text{B}_2(\text{p}_x)$ states is calculated. Electronic structure calculations at the CCSD(T)/aug-cc-pVTZ and TD-DFT B3LYP/6-311++G(3df,3pd) levels predict $\text{Mn}^+-\text{H}_2\text{O}$ bond lengths in the excited states that are in excellent agreement with experimental results. Progressions in the in-plane and out-of-plane bends are also observed in the ${}^7\text{B}_2$ and ${}^7\text{B}_1$ state's respectively. The observed rotational contours are fitted to give spin-rotation constants $\epsilon_{aa}'' = -3 \pm 1 \text{ cm}^{-1}$ for the ground state and $\epsilon_{aa}' = 0.5 \pm 0.5 \text{ cm}^{-1}$ and $\epsilon_{aa}' = -4.2 \pm 0.5 \text{ cm}^{-1}$ for the first and second excited states of $\text{Mn}^+-\text{H}_2\text{O}$ respectively. Vibrationally mediated photodissociation studies determined the O-H antisymmetric stretching frequency in the ground electronic state to be 3658 cm^{-1} . Overall, the excited states of Mn^+ interact more strongly with water than the ground state, resulting in decreased Mn-O bond length in the excited states, and an increase in the H-O-H angle.

References

1. III, W. L. P.; Copeland, C.; Kocak, A.; Sallese, Z.; Metz, R. B. *J. Chem. Phys.* **2014**, *141*, 204305.
2. Beyer, M. K. *Mass Spectrom. Rev.* **2007**, *26*, 517-541.
3. Magnera, T. F.; David, D. E.; Michl, J. *J. Am. Chem. Soc.* **1989**, *111*, 4100-4101.
4. Marinelli, P. J.; Squires, R. R. *J. Am. Chem. Soc.* **1989**, *111*, 4101-4103.
5. Dalleska, N. F.; Honma, K.; Sunderlin, L. S.; Armentrout, P. B. *J. Am. Chem. Soc.* **1994**, *116*, 3519-3528.
6. Misaizu, F.; Sanekata, M.; Tsukamoto, K.; Fuke, K.; Iwata, S. *J. Phys. Chem.* **1992**, *96*, 8259-8264.
7. Scurlock, C. T.; Pullins, S. H.; Reddic, J. E.; Duncan, M. A. *J. Chem. Phys.* **1996**, *104*, 4591-4599.
8. Ishikawa, H.; Nakano, T.; Eguchi, T.; Shibukawa, T.; Fuke, K. *Chem. Phys. Lett.* **2011**, *514*, 234-238.
9. Donnelly, S. G.; Schmuttenmaer, C. A.; Qian, J.; Farrar, J. M. *J. Chem. Soc.-Faraday Trans.* **1993**, *89*, 1457-1465.
10. Lessen, D. E.; Asher, R. L.; Brucat, P. J. *J. Chem. Phys.* **1990**, *93*, 6102-6103.
11. Scharfschwerdt, B.; van der Linde, C.; Balaj, O. P.; Herber, I.; Schutze, D.; Beyer, M. K. *Low Temp. Phys.* **2012**, *38*, 717-722.
12. Daluz, J. S.; Kocak, A.; Metz, R. B. *J. Phys. Chem. A* **2012**, *116*, 1344-1352.
13. Kocak, A.; Geoff, A.; Pearson III, W.; Altinay, G.; Metz, R. *J. Phys. Chem. A* **2013**, *117*, 1254-1264
14. Abate, Y.; Kleiber, P. D. *J. Chem. Phys.* **2005**, *122*, 084305.
15. Carnegie, P. D.; Bandyopadhyay, B.; Duncan, M. A. *J. Chem. Phys.* **2011**, *134*, 014302.
16. Walker, N. R.; Walters, R. S.; Pillai, E. D.; Duncan, M. A. *J. Chem. Phys.* **2003**, *119*, 10471-10474.
17. Carnegie, P. D.; Bandyopadhyay, B.; Duncan, M. A. *J. Phys. Chem. A* **2008**, *112*, 6237-6243.
18. Carnegie, P. D.; Bandyopadhyay, B.; Duncan, M. A. *J. Phys. Chem. A* **2011**, *115*, 7602-7609.
19. Walters, R. S.; Duncan, M. A. *Aust. J. Chem.* **2004**, *57*, 1145-1148.
20. Walters, R. S.; Pillai, E. D.; Duncan, M. A. *J. Am. Chem. Soc.* **2005**, *127*, 16599-16610.

21. Carnegie, P. D.; McCoy, A. B.; Duncan, M. A. *J. Phys. Chem. A* **2009**, *113*, 4849-4854.
22. Bandyopadhyay, B.; Reishus, K. N.; Duncan, M. A. *J. Chem. Phys. A* **2013**, *117*, 7794-7803.
23. Bandyopadhyay, B.; Duncan, M. A. *Chem. Phys. Lett.* **2012**, *530*, 10-15.
24. Sasaki, J.; Ohashi, K.; Inoue, K.; Imamura, T.; Judai, K.; Nishi, N.; Sekiya, H. *Chem. Phys. Lett.* **2009**, *474*, 36-40.
25. Furukawa, K.; Ohashi, K.; Koga, N.; Imamura, T.; Judai, K.; Nishi, N.; Sekiya, H. *Chem. Phys. Lett.* **2011**, *508*, 202-206.
26. Iino, T.; Ohashi, K.; Inoue, K.; Judai, K.; Nishi, N.; Sekiya, H. *J. Chem. Phys.* **2007**, *126*, 11.
27. Li, Y. Z.; Wang, G. J.; Wang, C. X.; Zhou, M. F. *J. Phys. Chem. A* **2012**, *116*, 10793-10801.
28. van der Linde, C.; Beyer, M. K. *J. Phys. Chem. A* **2012**, *116*, 10676-10682.
29. O'Brien, J. T.; Williams, E. R. *J. Phys. Chem. A* **2011**, *115*, 14612-14619.
30. Rosi, M.; Bauschlicher, C. W., Jr. *J. Chem. Phys.* **1989**, *90*, 7264-7272.
31. Trachtman, M.; Markham, G. D.; Glusker, J. P.; George, P.; Bock, C. W. *Inorg. Chem.* **1998**, *37*, 4421-4431.
32. Irigoras, A.; Fowler, J. E.; Ugalde, J. M. *J. Am. Chem. Soc.* **1999**, *121*, 8549-8558.
33. Metz, R. B. *Adv. Chem. Phys.* **2008**, *138*, 331-373.
34. Husband, J.; Aguirre, F.; Ferguson, P.; Metz, R. B. *J. Chem. Phys.* **1999**, *111*, 1433-1437.
35. Zhu, X.; Nur, A. H.; Misra, P. *J. Quant. Spectrosc. Rad. Trans.* **1994**, *52*, 167-177.
36. Citir, M.; Altinay, G.; Austein-Miller, G.; Metz, R. B. *J. Phys. Chem. A* **2010**, *114*, 11322-11329.
37. Frisch, M. J.; Trucks, G. W.; Schlegel, H. B.; Scuseria, G. E.; Robb, M. A.; Cheeseman, J. R.; Scalmani, G.; Barone, V.; Mennucci, B.; Petersson, G. A.; Nakatsuji, H.; Caricato, M.; Li, X.; Hratchian, H. P.; Izmaylov, A. F.; Bloino, J.; Zheng, G.; Sonnenberg, J. L.; Hada, M.; Ehara, M.; Toyota, K.; Fukuda, R.; Hasegawa, J.; Ishida, M.; Nakajima, T.; Honda, Y.; Kitao, O.; Nakai, H.; Vreven, T.; Montgomery Jr., J. A.; Peralta, J. E.; Ogliaro, F.; Bearpark, M.; Heyd, J. J.; Brothers, E.; Kudin, K. N.; Staroverov, V. N.; Keith, T.; Kobayashi, R.; Normand, J.; Raghavachari, K.; Rendell, A.; Burant, J. C.; Iyengar, S. S.; Tomasi, J.; Cossi, M.; Rega, N.; Millam, J. M.; Klene, M.; Knox, J. E.; Cross, J. B.; Bakken, V.; Adamo, C.; Jaramillo, J.; Gomperts, R.; Stratmann, R. E.; Yazyev, O.; Austin, A. J.; Cammi, R.; Pomelli, C.; Ochterski, J. W.; Martin, R. L.; Morokuma, K.; Zakrzewski, V. G.; Voth, G. A.; Salvador, P.; Dannenberg, J. J.; Dapprich, S.; Daniels, A. D.; Farkas, O.; Foresman, J. B.; Ortiz, J. V.; Cioslowski, J.; Fox, D. J. *Gaussian 09, Revision D.01*, Gaussian, Inc., Wallingford, CT: Pittsburgh PA, 2013.

38. Willey, K. F.; Yeh, C. S.; Robbins, D. L.; Pilgrim, J. S.; Duncan, M. A. *J. Chem. Phys.* **1992**, *97*, 8886-8895.
39. Kramida, A.; Ralchenko, Y.; Reader, J.; NIST ASD Team, NIST Atomic Spectra Database (Version 5.0) <http://physics.nist.gov/asd>. National Institute of Standards and Technology: Gaithersburg, MD, 2012.
40. Mosley, J. D.; Cheng, T. C.; Hasbrouck, S. D.; Ricks, A. M.; Duncan, M. A. *J. Chem. Phys.* **2011**, *135*, 104309-6.
41. Pickett, H. M. *J. Mol. Spectrosc.* **1991**, *148*, 371-377.
42. Tarczay, G.; Gopalakrishnan, S.; Miller, T. A. *J. Mol. Spectrosc.* **2003**, *220*, 276-290.
43. Brown, J. M.; Sears, T. J. *J. Mol. Spectrosc.* **1979**, *75*, 111-133.
44. Whitham, C. J.; Jungen, C. *J. Chem. Phys.* **1990**, *93*, 1001-1008.
45. Watanabe, H.; Iwata, S.; Hashimoto, K.; Misaizu, F.; Fuke, K. *J. Am. Chem. Soc.* **1995**, *117*, 755-763.

CHAPTER 4

VIBRATIONAL SPECTROSCOPY OF IRON-METHANE CLUSTERS

4.1 Introduction

As discussed in Chapter 1, the catalytic activation of methane is of fundamental interest because it involves the reaction of the simplest C-H bond and is of great industrial importance, as it would allow broader utilization of a plentiful natural resource. The study of reactions and reaction intermediates in the gas phase can be useful in clarifying the mechanism of C-H activation due to the advantage of the ions not being affected by solvent molecules.^{7, 71, 78-79, 90-91} Gas phase reaction studies show that several third-row transition metal cations M^+ react with methane at room temperature to produce $MCH_2^+ + H_2$.^{49, 93} In some cases, metal clusters are more reactive than the atoms, for example Rh^+ does not activate methane at room temperature,^{18, 93} while $Rh_x^+Ar_m$ does.³ Similarly, Au_2^+ shows sequential, ligand dependent reactivity with methane, under conditions where Au^+ does not react.^{57, 59} Additionally, reactivity that depends strongly on cluster size, as is observed with Pt_x^+ , has been suggested to be a signature of a good heterogeneous catalyst.^{56, 85}

Guided ion beam studies reveal that Fe_x^+ clusters show interesting size dependent reaction thresholds for the dehydrogenation of methane, with Fe_4^+ being particularly reactive.⁶³ Fe_4^+ also shows unique reactivity amongst smaller clusters and is the only iron cluster observed to react with ethylene at room temperature.⁸⁶ In addition, Fe_4^+ can facilitate C-C coupling, reacting with three molecules of ethylene to produce benzene.^{37, 45, 86-87} The mechanisms for these reactions have also been studied using density functional theory (DFT).²⁰⁻²¹

The first step in the reaction of a metal cluster ion M_x^+ and methane is the formation of a $M_x^+(CH_4)$ entrance channel complex. Interaction with the metal weakens and polarizes the proximate C-H bonds, leading to a substantial red shift in the lowest C-H stretching frequencies, and increasing their IR absorption intensity. Measurement of this interaction has prompted studies of the vibrational spectroscopy of several $M^+(CH_4)_n$ complexes,^{22, 31, 54, 75, 77} of products of sequential reactions of Pt^+

with methane,¹⁰⁹ and of $\text{Pt}_x^+(\text{CH}_4)\text{Ar}_2$ ($x=3-5$).⁴¹ Our group has studied vibrational spectra of $\text{Fe}^+(\text{CH}_4)_n$ ($n = 1-4$)²² in the C-H stretching region. To investigate larger clusters for the aforementioned reasons we extend these works to the iron dimer, trimer and tetramer, presenting the vibrational spectra of $\text{Fe}_2^+(\text{CH}_4)_n$ ($n = 1-3$) and $\text{Fe}_4^+(\text{CH}_4)_4$. This provides an opportunity to investigate the relationship between the reactivity of the cluster and the structure of the entrance channel complex and shifts in its C-H stretching frequencies.

4.2 Experimental and Computational Methods

Iron-methane cluster complexes are produced in a laser ablation source and studied with a dual time-of-flight reflectron mass spectrometer, described in detail in Chapters 2 and 3 as well as elsewhere.^{43, 66} For these studies, the ion source was modified from how it was presented in Chapter 3 in order to promote creation of larger clusters. Ions are formed by laser ablation of an iron rod (Sigma-Aldrich, 99.8% pure) and subsequent clustering in an expansion gas mixture that comes from one or two pulsed valves (Parker, series 9). The primary valve, whose gas mix consists of 1-10% methane in helium at 60-140 psi backing pressure, introduces gas before ablation. This mixture travels through a 2.5 mm ID, 20 mm long tube, then interacts with gas from the secondary valve (1-100% methane in helium at 10-20 psi backing pressure). This fast flow reactor¹⁰³ design has the advantage of giving independent control over the methane concentration, as well as reducing the possibility of the ablation laser and resulting plasma fragmenting methane. The gas then flows through a 50 mm long, 2.5 mm ID aluminum nozzle to help induce more collisions and promote larger cluster formation. Various nozzles are used, mainly consisting of a long straight section followed by a 10° cone in order to promote formation of the desired ions.¹⁰¹

The ions undergo supersonic expansion into vacuum, cooling to a rotational temperature of ~ 10 K.² The ions then pass through a skimmer, into the extraction region of a Wiley-McLaren time-of-flight mass spectrometer.¹¹¹ Ions are all accelerated to 1800 V kinetic energy, re-referenced to ground potential and enter a field free flight tube section. An IR laser system photodissociates the mass

selected ions at the turning point of the reflectron. The parent and photofragment ions are re-accelerated out of the reflectron, traveling through the field-free region where they finally impact upon a 40 mm diameter dual microchannel plate detector. The ion masses are determined from their characteristic flight times. The IR laser system is an optical parametric oscillator/optical parametric amplifier (LaserVision) that is pumped by a Spectra Physics GCR-190 Nd:YAG operating at 10 Hz. The system is tunable from 2200 to 5000 cm^{-1} and produces ~ 6 mJ per pulse near 3100 cm^{-1} . In the reflectron region a multi-pass mirror setup allows for the IR beam to cross the ion beam ~ 15 times.⁵ In order to properly calibrate the laser wavelength, well-known CH_4 absorptions are used.⁸²

The ion signal is amplified, and acquired on a gated integrator or digital oscilloscope. A *LabView* program averages the data and scans the IR laser. The photodissociation spectrum is obtained by measuring the normalized fragment ion signal (fragment ion signal divided by the parent ion signal and IR laser fluence) as a function of wavelength. The photodissociation spectrum is the product of the photodissociation quantum yield and the absorption. The only fragments observed correspond to the loss of one or more intact CH_4 . Depending upon the ion, 0.2% to 20% of the parent photodissociates. For some ions a variant of the ion collection program is used in which the ablation laser operates at 20 Hz, while the photodissociation laser runs at 10 Hz. The gated integrator then collects laser on and laser off signals on alternate shots. This is used for more accurate background subtraction and is particularly useful for some of the heavier ions where the mass gate does not completely remove lighter parent ions with the same flight time as the fragment.

Calculations are carried out with the *Gaussian 09* program package.³⁴ Optimized geometries of the ions are computed using the B3LYP, BPW91 and M11L⁷³ density functionals and the 6-311++G(3df,3pd) basis set. All reported energies include zero-point energy. The calculated vibrational frequencies are harmonic, whereas measured frequencies include anharmonicity. To account for this effect, computed frequencies are scaled by the ratio of the experimental and calculated C-H stretching frequencies of isolated CH_4 ($\nu_1 = 2917 \text{ cm}^{-1}$, $\nu_3 = 3019 \text{ cm}^{-1}$) using the same basis set. The scaling

factor is 0.963 for B3LYP, 0.979 for BPW91 and 0.971 for M11L. For comparison with experiment, calculated spectra are convoluted with a 20 cm^{-1} fwhm Gaussian.

4.3 Results and Discussion

The results of these studies have been published in Physical Chemistry Chemical Physics (focused on Fe_2 clusters) and in The Journal of Physical Chemistry A (focused on the Fe_3 and Fe_4 clusters).^{8, 25} **Figure 4.1** shows the photodissociation spectra of $\text{Fe}_2^+(\text{CH}_4)_n$ ($n=1-3$) and **Figure 4.2** shows the photodissociation spectra of $\text{Fe}_3^+(\text{CH}_4)_n$ ($n=1-3$). Each spectrum consists of a single peak in the C-H stretching region, seen in the $\text{Fe}_2^+(\text{CH}_4)$ spectrum at 2803 cm^{-1} and the $\text{Fe}_3^+(\text{CH}_4)$ spectrum at 2785 cm^{-1} , a red shift of 114 cm^{-1} and 132 cm^{-1} respectively from the symmetric stretch in bare methane. Additional methane ligands reduce this red shift. In addition, we can compare $\text{Fe}_n^+(\text{CH}_4)_n$ ($n=2-4$) complexes for cluster patterns, which have a 1:1 ratio of iron to methane. These correspond to one methane for every surface metal atom. These monolayer complexes are particularly abundant in the mass spectrum. Their vibrational spectra are shown in **Figure 4.3**. The red shift in the lowest frequency C-H stretch is seen to increase with cluster size. At first glance, this seems surprising because the electrostatic interaction between the metal and methane decreases with increasing n due to the charge being spread amongst more iron atoms. The increased red shift thus signals enhanced covalency in the Fe- CH_4 interaction for the larger clusters and parallels the observed^{63, 86} reactivity $\text{Fe}_4^+ > \text{Fe}_3^+ > \text{Fe}_2^+$.

To determine the structure and characterize the vibrations of each $\text{Fe}_x^+(\text{CH}_4)_n$ cluster, we carry out geometry optimization and vibrational frequency calculations for several potential isomers and spin states. This also provides an opportunity to assess the reliability of different functionals in predicting the binding energies and vibrational frequencies of metal cluster ion-ligand complexes. Our previous studies of complexes of methane with atomic metal cations $\text{M}^+(\text{CH}_4)_n$ ($\text{M}=\text{Fe}, \text{Co}, \text{Ni}, \text{Cu}, \text{Ag}$)^{8, 52, 54} have shown that the B3LYP hybrid density functional is fairly accurate in predicting the observed vibrational spectra. Comparison of several DFT methods on neutral and charged iron clusters

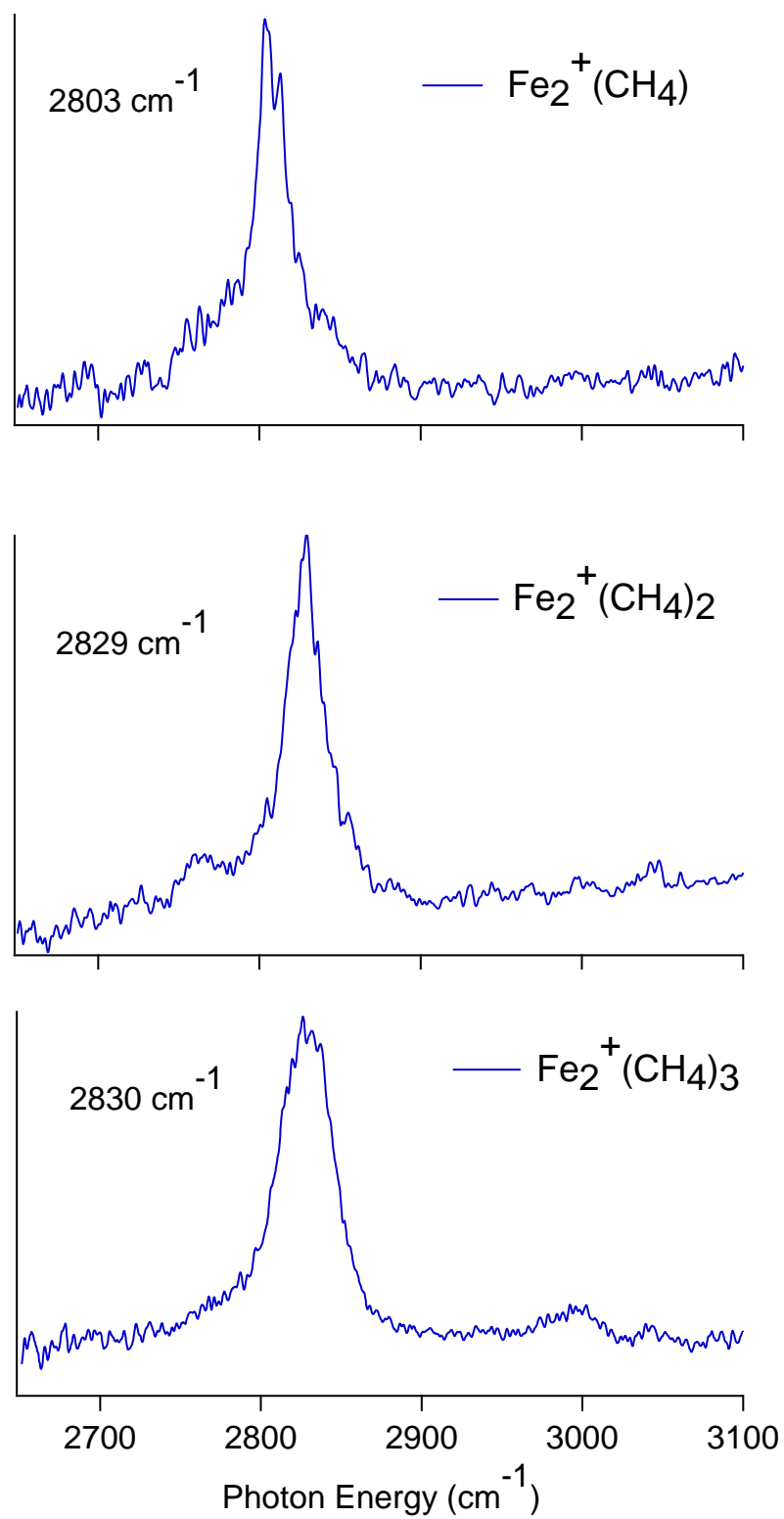


Figure 4.1 Infrared photodissociation spectra of $\text{Fe}_2^+(\text{CH}_4)_n$ ($n=1-3$) in the C-H stretching region. The wavenumbers of the major peak in each spectrum are indicated.

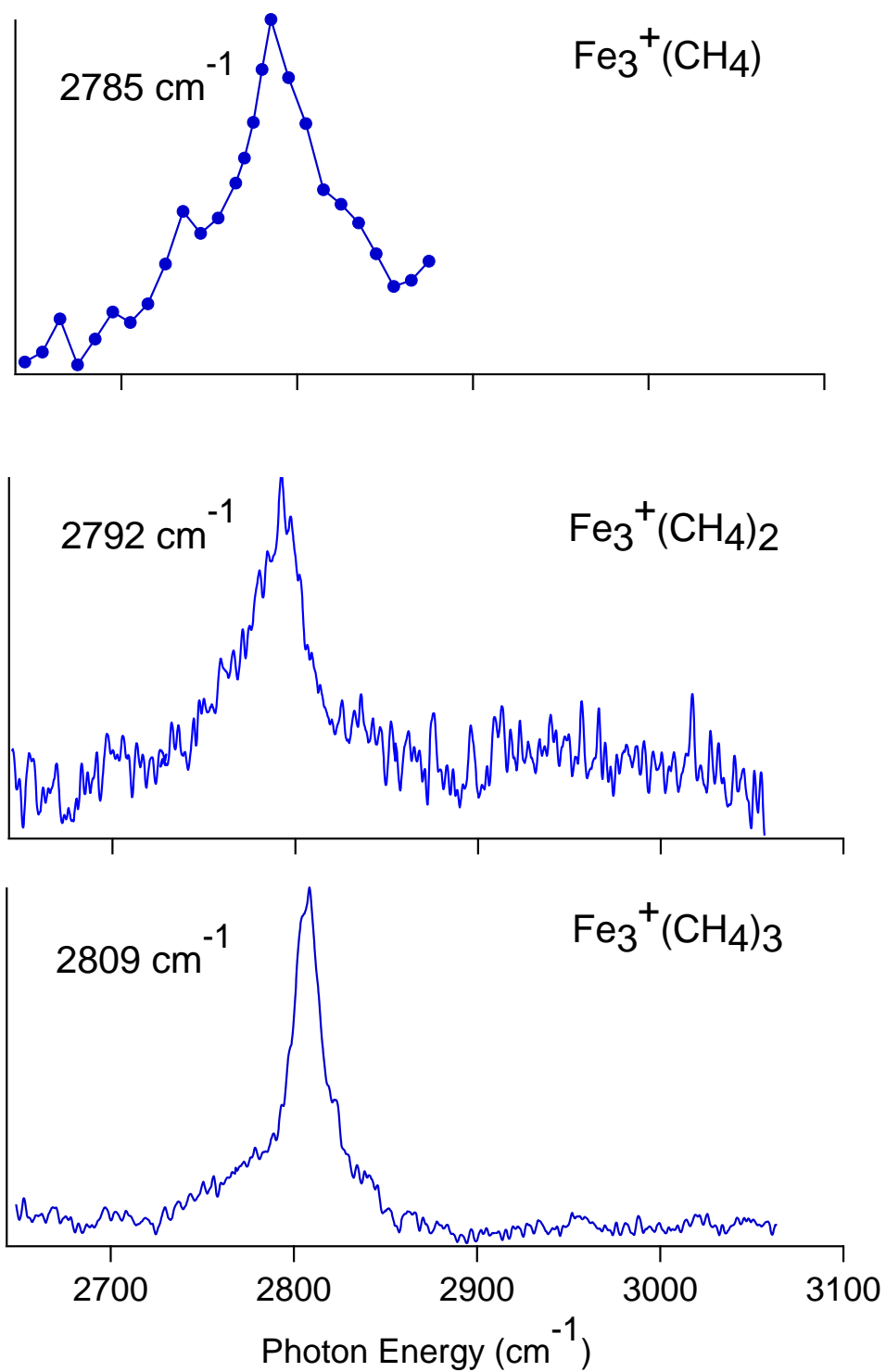


Figure 4.2 Infrared photodissociation spectra of Fe₃⁺(CH₄)_n (n=1-3) in the C-H stretching region. The wavenumbers of the major peak in each spectrum are indicated.

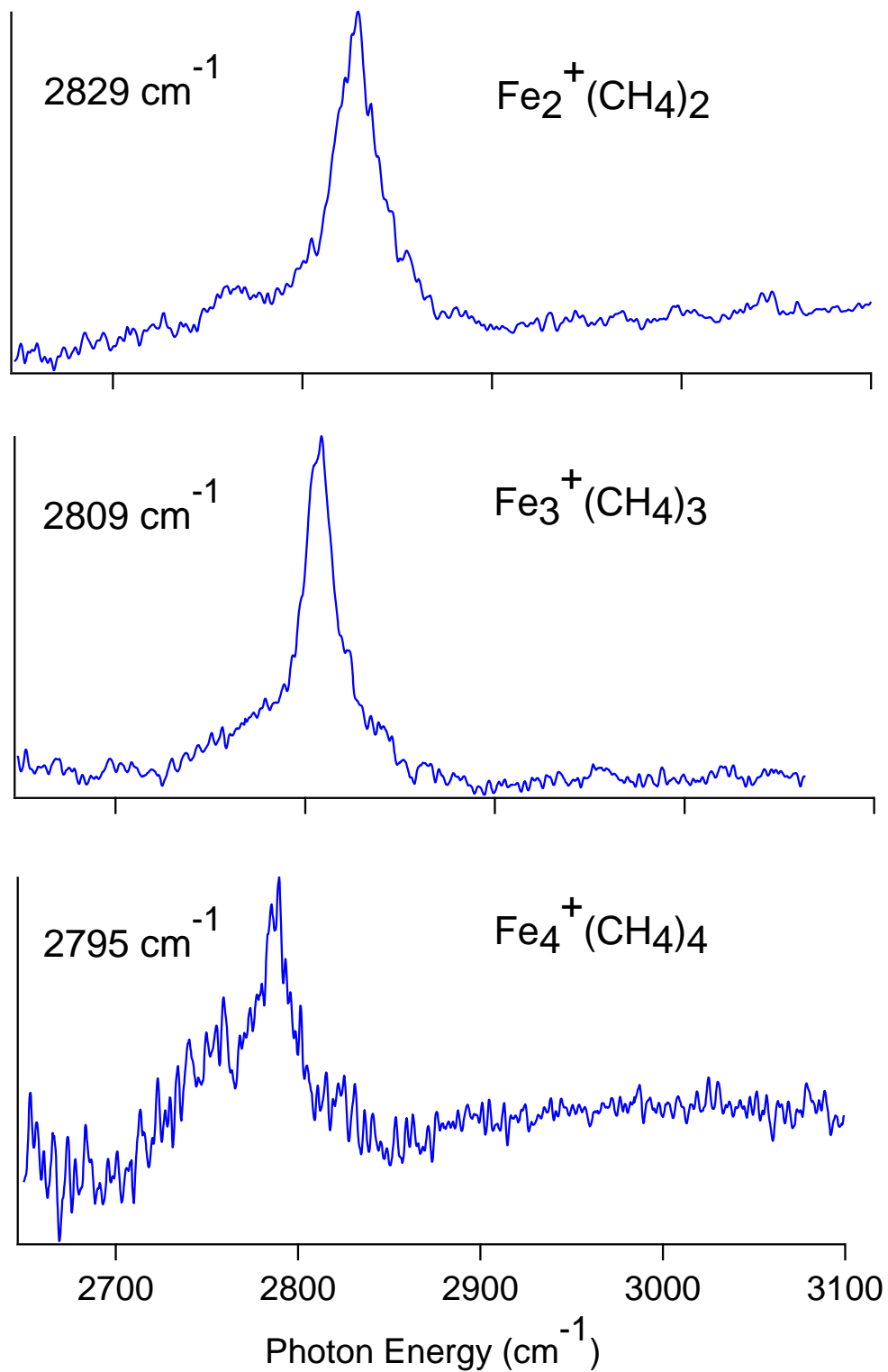


Figure 4.3 Infrared photodissociation spectra of $\text{Fe}_n^+(\text{CH}_4)_n$ ($n=2-4$) in the C-H stretching region. The wavenumbers of the major peak in each spectrum are indicated.

concluded that the non-hybrid BPW91 functional is often preferable over B3LYP.³⁹⁻⁴⁰ In this work we used the generalized gradient approximation (GGA) BPW91 functional, hybrid-GGA B3LYP functional and range separated meta-GGA (with local exchange) M11L functional. M11L was developed to better treat systems with multireference character, which is ideal for metal clusters.⁷³

4.3.1 Calculation Discussion

Calculated geometries, energies, vibrational frequencies and intensities of the lowest energy states of $\text{Fe}_x^+(\text{CH}_4)_n$ at the M11L/6-311++G(3df,3pd) level are presented in **Appendix A**. All three functionals predict that Fe_2^+ is an octet state ($2S+1=8$), Fe_3^+ is a dectet and Fe_4^+ is a duodectet. They also predict that the ground state multiplicity does not change with added methanes. **Table 4.1** summarizes the calculated methane binding energies of the clusters for the three functionals. In addition, all functionals predict that the binding energy of the first methane is in the order $\text{Fe}_2^+ > \text{Fe}_3^+ > \text{Fe}_4^+$. This weaker binding with increasing cluster size is in contrast to the trends in reactivity and redshifts. This is likely due to a decrease in the electrostatic contribution to the binding energy with increasing cluster size that is not completely compensated for by increased covalent contribution.

Looking at B3LYP and M11L calculations for the monolayer complexes, we see the partial charge on the Fe atoms in the cluster decrease as the cluster size gets larger, as one would expect from the same charge (+1 for the total cluster) being spread out amongst more irons (**Table 4.2**). Interestingly however, the partial charge on each methane increases as the cluster size increases. For example, using the M11L functional looking at atomic polar tensor (APT) derived charges results, the charge on methane for $\text{Fe}_2^+(\text{CH}_4)_2$ is (+) 0.0619 on each methane, (+) 0.069 for each methane in $\text{Fe}_3^+(\text{CH}_4)_3$, and (+) 0.073 for each methane in $\text{Fe}_4^+(\text{CH}_4)_4$. Looking at the total charge held by the Fe and CH_4 , we see that in the Mulliken approximation, the combined methanes hold ~14% of the total +1 charge for $\text{Fe}_2^+(\text{CH}_4)_2$, while ATP derived charges predict ~12%. This sum of the charges held by the methanes increases to ~54% and 29% of the charge for $\text{Fe}_4^+(\text{CH}_4)_4$ for the Mulliken and ATP methods respectively, a large increase in charge transfer. This indicates increased charge transfer from

Species	Calculated Fe-CH ₄ ⁺ Bond Dissociation Energy (cm ⁻¹)			
	B3LYP	B3LYP-GD3	BPW91	M11L
Fe ₂ ⁺ (CH ₄)	3304		3344	4229
Fe ₂ ⁺ (CH ₄) ₂	1849	2642	1931	3340
Fe ₂ ⁺ (CH ₄) ₃	809		1566	2565
Fe ₃ ⁺ (CH ₄)	3012		3219	3587
Fe ₃ ⁺ (CH ₄) ₂	2587		2639	3342
Fe ₃ ⁺ (CH ₄) ₃	2145	2928	2130	2907
Fe ₄ ⁺ (CH ₄)	2912		3142	3532
Fe ₄ ⁺ (CH ₄) ₂	2688		2914	3214
Fe ₄ ⁺ (CH ₄) ₃	2407		2400	3102
Fe ₄ ⁺ (CH ₄) ₄	1476	2046	1895	2498

Table 4.1 C-H bond dissociation energy of Fe_x⁺(CH₄)_n clusters calculated with B3LYP, B3LYP-GD3, BPW91 and M11L functionals with the 6-311++G(3df,3pd) basis set.

Partial Charges on Iron and Methane in Monolayer Complexes (+1 total)		
Species	Charge per Fe	Charge per CH ₄
Mulliken Charges		
Fe ₂ ⁺ (CH ₄) ₂	0.432	0.0678
Fe ₃ ⁺ (CH ₄) ₃	0.1848	0.1485
Fe ₄ ⁺ (CH ₄) ₄	0.1155	0.1345
Atomic Polar Tensor Derived Charges		
Fe ₂ ⁺ (CH ₄) ₂	0.4381	0.0619
Fe ₃ ⁺ (CH ₄) ₃	0.2649	0.069
Fe ₄ ⁺ (CH ₄) ₄	0.177	0.073

Table 4.2 Partial Charges on Iron and Methane in Monolayer Complexes (+1 total). Calculated with M11L with the 6-311++G(3df,3pd) basis set.

Fe to CH₄ as the cluster size increases. This may result from a back-bonding interaction between the Fe and CH₄ that grows stronger with cluster size, increasing the covalency character. This increased covalency in Fe-C bonding weakens the proximate C-H bonds, leading to the observed large red shifts. Results for each ion will be discussed in turn.

4.3.1 Fe₂⁺(CH₄)

The spectrum of Fe₂⁺(CH₄) (**Figure 4.4**) shows a single intense peak at 2803 cm⁻¹ with 26 cm⁻¹ fwhm. The photodissociation yield is 9%. Similar photodissociation yields are observed for M⁺(CH₄)Ar₂ (M = Co, Ni, Cu), which have similar calculated C-H absorption intensity for the lowest frequency C-H stretch and where the low Ar binding energy ensures that one photon has sufficient energy to dissociate the complex.^{52, 54} This suggests that photodissociation of Fe₂⁺(CH₄) also has a quantum yield of one and is a single photon process at ~2800 cm⁻¹, suggesting that the calculations slightly overestimate the methane binding energy.

The B3LYP and BPW91 functionals predict similar geometries for Fe₂⁺(CH₄). The hydrogen atoms have connectivity of nearly η^3 , slightly distorted towards η^2 , leading to overall C_s symmetry. The Fe-C distance is calculated to be 2.389 Å (B3LYP), 2.300 Å (BPW91) and 2.26 Å (M11L). Geometry optimizations starting from several η^2 structures and bridged structures all relax to the η^3 ground state. Detailed geometries, energies and vibrational frequencies for all species are given in **Appendix A**. The calculated binding energies and geometries are similar to those obtained by Chiodo *et al.* in their study of the reaction of Fe₂⁺ with methane.¹⁹ They predict the Fe₂⁺-CH₄ binding energy to be 3850 cm⁻¹ and 3532 cm⁻¹ at the B3LYP/DZVP_{opt} and BPW91/DZVP_{opt} level of theory respectively. These binding energies are slightly higher than those obtained using the 6-311++G(3df, 3pd) basis set; all basis sets predict η^3 hydrogen coordination and very similar Fe-C bond distances.

The BPW91 calculation predicts a strong peak at 2798 cm⁻¹; the remaining C-H stretch

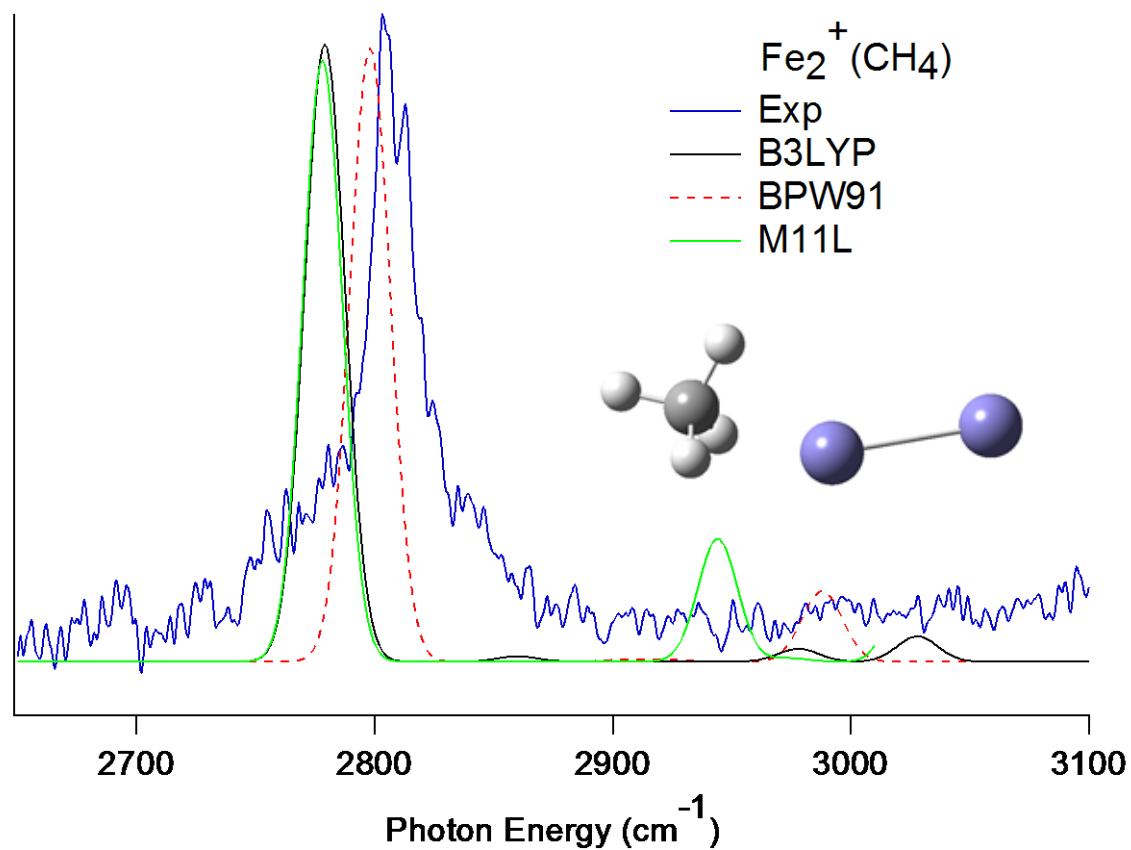


Figure 4.4 Experimental IR photodissociation spectrum of $\text{Fe}_2^+(\text{CH}_4)$ along with the simulated spectra using the B3LYP, BPW91 and M11L functionals. The structure is the octet state of the molecule according to B3LYP.

absorptions are very weak. Thus, the simulated spectrum matches the experiment very well. The B3LYP and M11L calculated spectra are similar, with the major peak at 2779 and 2777 cm^{-1} respectively, about 20 cm^{-1} below the observed peak. The observed 2803 cm^{-1} vibration corresponds to the symmetric C-H stretch, with all C-H bonds stretching in phase, with substantially larger amplitude for the three proximate C-H bonds than the distal.

4.3.2 $\text{Fe}_2^+(\text{CH}_4)_2$

The spectrum of $\text{Fe}_2^+(\text{CH}_4)_2$ (**Figure 4.5**) shows a single intense peak at 2829 cm^{-1} with 25 cm^{-1} fwhm. The photodissociation yield for $\text{Fe}_2^+(\text{CH}_4)_2$ is observed to be 30%, again consistent with single photon photodissociation. The calculated absorption intensity for this vibration is twice that of the corresponding vibration in $\text{Fe}_2^+(\text{CH}_4)$, leading to the increased photodissociation yield. The calculated B3LYP and BPW91 binding energies of $\sim 1900 \text{ cm}^{-1}$ are consistent with single photon dissociation. M11L, at 3340 cm^{-1} , overestimates the binding energy.

Although M11L includes dispersion effects implicitly, B3LYP and BPW91 do not.²⁹ To assess the importance of dispersion, calculations with empirical dispersion were carried using B3LYP. This was done using the D3 version of Grimme's dispersion with the original D3 damping function.³⁸ Calculated binding energies using this method are shown in **Table 4.1** and simulated spectra comparisons are shown in **Appendix B**. Differences between the predicted spectra for the $\text{Fe}_2^+(\text{CH}_4)_2$ and $\text{Fe}_3^+(\text{CH}_4)_3$ complexes are minimal, with the major peak in $\text{Fe}_2^+(\text{CH}_4)_2$ lying $<1 \text{ cm}^{-1}$ apart between the two methods, and the major peak in the $\text{Fe}_3^+(\text{CH}_4)_3$ dispersion calculation lying $\sim 10 \text{ cm}^{-1}$ below the peak in the standard calculation. There are major differences however in calculated spectra of $\text{Fe}_4^+(\text{CH}_4)_4$. For $\text{Fe}_4^+(\text{CH}_4)_4$ using dispersion, the main peak is a singlet, predicted at 2767 cm^{-1} , while it is a doublet with peaks at 2784 and 2813 cm^{-1} in the standard calculation. This mainly results from the doublet predicted in the standard calculation red shifting the peaks to different degrees, resulting in a wider peak with a shoulder in the case of the dispersion calculation. Thus, the main result of including dispersion for the simulations is a moderate redshift of 0-30 cm^{-1} , with its significance increasing with

cluster size. The results of dispersion on calculated binding energies are an increase in binding energy of $\sim 600\text{-}800\text{ cm}^{-1}$, putting the energies of B3LYP-D3 close to those calculated by M11L. This increase in bonding energy makes sense considering that dispersion is an overall attractive force.

The B3LYP calculation predicts two stable structures that can contribute to the spectrum. The ground state has each iron coordinated to one CH_4 . In this structure, both the CH_4 are equivalent, with a 2.462 \AA Fe-C bond. As a result, the predicted spectrum has a single peak at 2814 cm^{-1} , as shown in **Figure 4.5**. The calculations predict hydrogen atom connectivity of nearly η^3 , slightly distorted towards η^2 . There is a second local minimum, $\sim 380\text{ cm}^{-1}$ higher in energy, in which both ligands are bound to one of the iron atoms. The resulting spectrum is calculated to have a doublet at $2803/2833\text{ cm}^{-1}$. As the observed spectrum consists of a single peak, this structure is at most a minor contributor to the experiment. Similar to $\text{Fe}_2^+(\text{CH}_4)$, structures with bridging methanes relax to the ground state terminal structure. Simulated spectra of structures in which each iron is coordinated to one methane are in good accord with the experimental spectrum and reproduce the experimental observation that the addition of the second CH_4 leads to a reduced red shift in the spectrum.

The BPW91 calculation predicts similar structures. In the isomer with each Fe interacting with one CH_4 , the Fe-C distances are 2.405 \AA and 2.512 \AA . As a result of non-equivalent Fe-C interactions, the vibrational spectrum has a peak at 2814 cm^{-1} with a shoulder at 2827 cm^{-1} . This leads to a broader peak centered at 2816 cm^{-1} . The other isomer, in which both CH_4 are bound to one iron, is calculated to be the ground state, 635 cm^{-1} lower in energy. However, the predicted spectrum is red shifted by 200 cm^{-1} , clearly not in accord with the experiment.

The M11L calculations likewise predict two stable structures with similar energies. For the isomer with each Fe interacting with one CH_4 , the Fe-C distances are both 2.305 \AA with the hydrogens in η^3 coordination. In the isomer with both CH_4 bound to one iron, the Fe-C distances are 2.401 \AA and 2.470 \AA , both with η^3 hydrogen coordination. This isomer is predicted to be 680 cm^{-1} higher in energy. Both calculations predict a single main peak, located at 2783 cm^{-1} for the case of one C per Fe, and

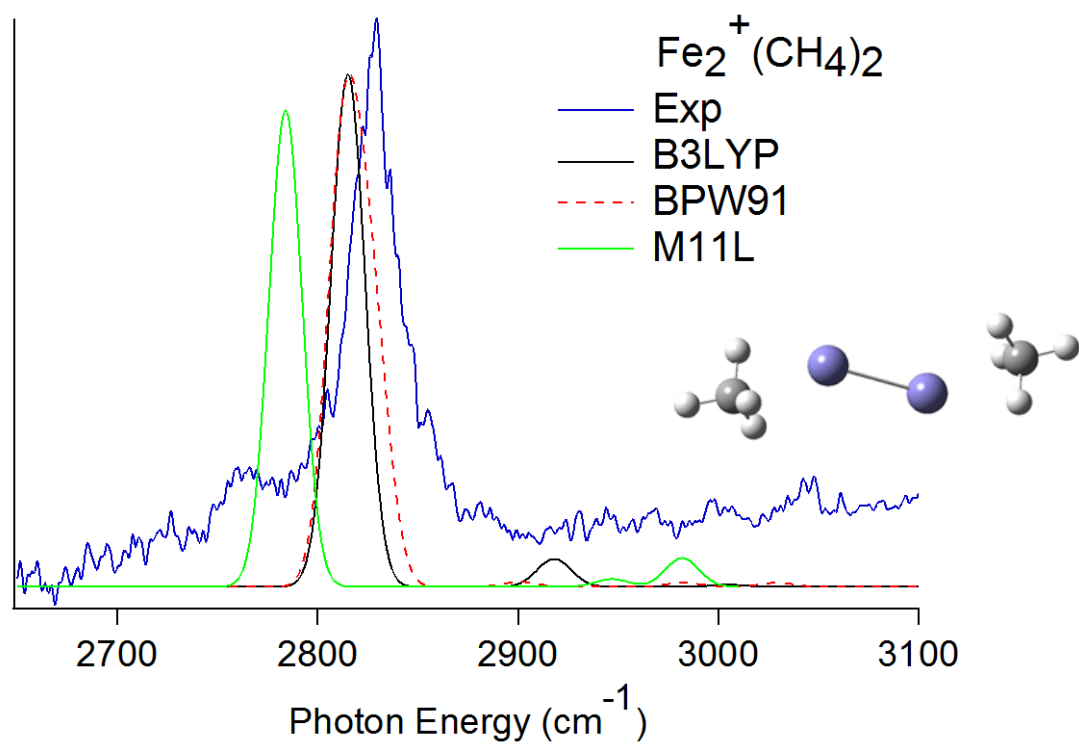


Figure 4.5 Experimental IR photodissociation spectrum of $\text{Fe}_2^+(\text{CH}_4)_2$ along with the simulated spectra using the B3LYP, BPW91 and M11L functionals. The structure is the octet state of the molecule according to B3LYP.

2813 cm^{-1} in the case of both C attached to one Fe. The main peak of the calculated spectrum of the low-energy isomer lies 46 cm^{-1} above experiment, while the high energy isomer lies 16 cm^{-1} above.

4.3.3 $\text{Fe}_2^+(\text{CH}_4)_3$

The spectrum of $\text{Fe}_2^+(\text{CH}_4)_3$ (**Figure 4.6**) shows a peak centered at 2830 cm^{-1} . The peak is significantly broader than those of the smaller clusters for reasons given below, with 36 cm^{-1} fwhm. The spectrum also shows a much smaller peak centered at 3000 cm^{-1} . The BPW91 calculation predicts that the three CH_4 are clearly not equivalent. One of the iron atoms interacts strongly with two CH_4 , resulting in Fe-C bond distances of 2.368 Å and 2.419 Å respectively, with hydrogen atom connectivity of approximately η^2 . The other iron interacts weakly with the CH_4 proximal to it, at a bond distance of 2.640 Å and it has η^3 coordination. As a result of this non-equivalency, the predicted spectrum has three intense peaks at 2725, 2747, and 2860 cm^{-1} . The resulting simulated spectrum clearly disagrees with the observed spectrum.

The B3LYP and M11L calculations disagree with BPW91, predicting the interaction of the three methanes to be very similar. In M11L, two of the CH_4 interact with one iron at a bond distance of 2.50 Å (η^2/η^3 coordination) and 2.38 Å (η^3 coordination), while the third CH_4 interacts with the proximal iron at a bond distance of 2.27 Å with η^3 hydrogen coordination. These non-equivalent interactions result in the M11L calculation predicting multiple peaks with the main peak lying at 2811 cm^{-1} with a shoulder at 2775 cm^{-1} , matching experiment well. Two smaller peaks are predicted at 2924 (not seen) and 3012 cm^{-1} which is slightly higher than the small peak observed at 3000 cm^{-1} .

In the B3LYP calculation, two of the CH_4 interact with one of the irons with Fe-C bond distances of 2.509 Å (η^2/η^3 coordination) and 2.671 Å (η^2 coordination) respectively, while the third

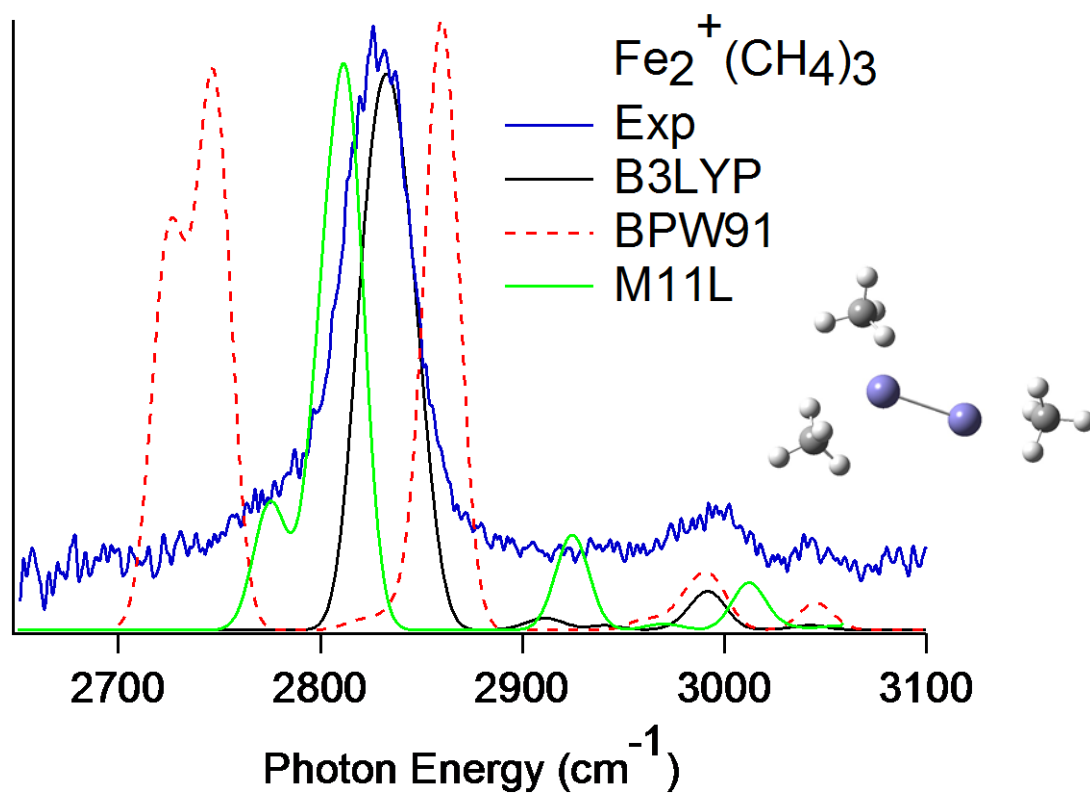


Figure 4.6 Experimental IR photodissociation spectrum of $\text{Fe}_2^+(\text{CH}_4)_3$ along with the simulated spectra using the B3LYP, BPW91 and M11L functionals. The structure is the octet state of the molecule according to B3LYP.

CH₄ interacts with the proximal iron at a bond distance of 2.527 Å, and it has η^3 hydrogen coordination. Thus, the B3LYP calculation predicts three very closely lying peaks at 2822, 2834 and 2846 cm⁻¹. This leads to a single broad peak centered at 2832 cm⁻¹. The close vicinity of these peaks indicates that the three CH₄ have a similar interaction with the iron dimer. The simulated spectrum predicted by the B3LYP calculation is an excellent match to the experimental spectrum. The simulation also suggests that the breadth of the experimental peak is due to nearly degenerate unresolved C-H stretching vibrations, characteristic of a complex with three nearly equivalent CH₄. The calculation also predicts a small peak at 2992 cm⁻¹. For Fe₂⁺(CH₄)₃ the calculations predict that the sextet state does not lie very far above the octet. Because the sextet interacts more strongly with CH₄ than the octet state, it leads to a highly red-shifted spectrum, which is not consistent with the experimental spectrum.

4.3.4 Fe₃⁺(CH₄)

The spectrum of Fe₃⁺(CH₄) (**Figure 4.7**) shows a single peak at 2785 cm⁻¹ with 50 cm⁻¹ fwhm. The photodissociation spectrum was obtained using difference spectra due to the low photodissociation yield of 0.2%. This suggests that photodissociation of Fe₃⁺(CH₄) is a multi-photon process at ~2785 cm⁻¹. This differs from Fe₂⁺(CH₄), which had a photodissociation yield of ~9%, consistent with a single photon process.⁸ These results indicate that, in contrast to the DFT calculations, Fe₃⁺ makes a stronger bond to CH₄ than Fe₂⁺.

The B3LYP and BPW91 functionals predict similar geometries for Fe₃⁺(CH₄), with η^2 hydrogen atom coordination and Fe-C distances of 2.394 Å and 2.377 Å respectively. In M11L the coordination is η^3 and the Fe-C distance is calculated to 2.284 Å. Due to the differing hydrogen atom coordination, B3LYP and BPW91 predict a larger red shift than M11L in the most intense C-H stretch. The B3LYP calculated spectrum is dominated by a peak at 2743 cm⁻¹, ~42 cm⁻¹ below the observed peak. The BPW91 calculation is similar, at 2755 cm⁻¹. The M11L calculations provide the best match to experiment, predicting a peak at 2782 cm⁻¹, only 3 cm⁻¹ below experiment. The observed 2785 cm⁻¹

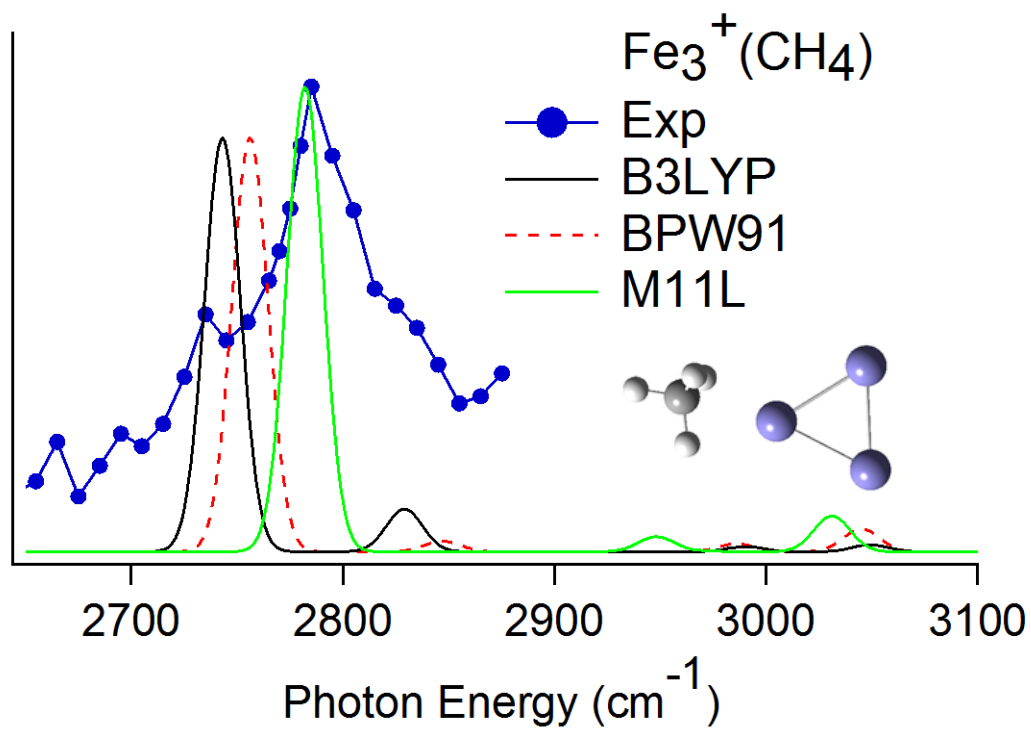


Figure 4.7 Experimental IR photodissociation spectrum of $\text{Fe}_3^+(\text{CH}_4)$ along with simulated spectra using B3LYP, BPW91 and M11L functionals and the 6-311++G(3df,3pd) basis set. The calculated M11L structure is shown.

vibration corresponds to the symmetric C-H stretch, in which all the C-H bonds stretch in phase, with slightly larger amplitude for the three proximate C-H bonds than the distal. Interaction with the metal breaks the degeneracy of the other three C-H stretches in methane. They are predicted to have significantly lower intensity than the symmetric stretch and were not experimentally observed. The symmetric C-H stretch vibration is the lowest frequency and most intense C-H stretch for all of the $\text{Fe}_x^+(\text{CH}_4)_n$ complexes. The calculated and observed frequencies for this vibration are summarized in **Table 4.3**. Calculated frequencies and intensities for all vibrations are listed in **Appendix A**.

4.3.5 $\text{Fe}_3^+(\text{CH}_4)_2$

The spectrum of $\text{Fe}_3^+(\text{CH}_4)_2$ (**Figure 4.8**) shows a single intense peak at 2792 cm^{-1} with 30 cm^{-1} fwhm. The calculated absorption intensity for this vibration is twice that of the corresponding vibration in $\text{Fe}_3^+(\text{CH}_4)$, while the photodissociation yield has increased over fifty-fold, to 14%. This strongly suggests that photodissociation of $\text{Fe}_3^+(\text{CH}_4)_2$ requires only one photon while $\text{Fe}_3^+(\text{CH}_4)$ requires more than one photon. The B3LYP and BPW91 calculations predict a single photon process for photodissociation of $\text{Fe}_3^+(\text{CH}_4)_2$ with binding energies of 2587 and 2639 cm^{-1} respectively. The binding energy with the M11L functional is somewhat higher, 3342 cm^{-1} , suggesting a multiphoton process would occur. All three functionals predict the methane binding in $\text{Fe}_3^+(\text{CH}_4)_2$ and $\text{Fe}_3^+(\text{CH}_4)$ are similar. For B3LYP and BPW91 this is η^2 hydrogen coordination with equal Fe-C bond lengths of 2.404 \AA and 2.423 \AA respectively. The M11L hydrogen coordination is approximately η^3 with Fe-C bond lengths of 2.297 \AA . As a result, the spectrum is dominated by a peak at 2751 cm^{-1} for B3LYP, 2753 cm^{-1} for BPW91 and 2784 cm^{-1} for M11L. Again, the M11L result provides the best match to experiment, shown in **Figure 4.8**.

4.3.6 $\text{Fe}_3^+(\text{CH}_4)_3$

The spectrum of $\text{Fe}_3^+(\text{CH}_4)_3$ (**Figure 4.9**) shows a single peak centered at 2809 cm^{-1} . This peak is narrower than those in the smaller clusters, with 20 cm^{-1} fwhm. The photodissociation yield of 20%

Species	Lowest C-H Stretching Frequency (cm ⁻¹)			
	B3LYP	BPW91	M11L	Experiment
Fe ₂ ⁺ (CH ₄)	2779	2798	2778	2803
Fe ₂ ⁺ (CH ₄) ₂	2814	2814	2783	2829
Fe ₂ ⁺ (CH ₄) ₃	2822, 2834, 2846	2725, 2747, 2860	2775, 2811, 2924, 3011	2830, 3000
Fe ₃ ⁺ (CH ₄)	2743	2756	2782	2785
Fe ₃ ⁺ (CH ₄) ₂	2751	2753	2784	2792
Fe ₃ ⁺ (CH ₄) ₃	2773	2766	2790	2809
Fe ₄ ⁺ (CH ₄)	2850	2721	2801	
Fe ₄ ⁺ (CH ₄) ₂	2844	2727, 2802	2806	
Fe ₄ ⁺ (CH ₄) ₃	2845	2725	2790	
Fe ₄ ⁺ (CH ₄) ₄	2820, 2851	2723	2803	2795

Table 4.3 Experimental and calculated lowest C-H stretching frequencies of Fe₂⁺(CH₄)_n (n=1-3), Fe₃⁺(CH₄)_n (n=1-3) and Fe₄⁺(CH₄)_n (n=1-4). Calculations use the B3LYP, BPW91 and M11L functionals with the 6-311++G(3df,3pd) basis set.

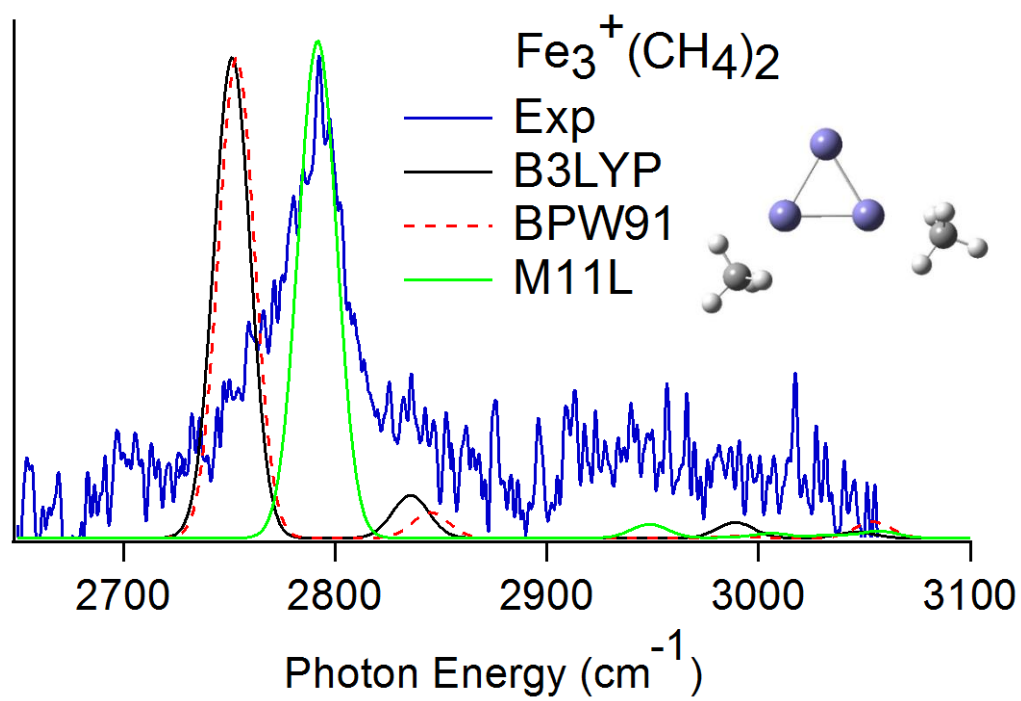


Figure 4.8 Experimental IR photodissociation spectrum of $\text{Fe}_3^+(\text{CH}_4)_2$ along with simulated spectra using B3LYP, BPW91 and M11L functionals and 6-311++G(3df,3pd) basis set. The M11L structure is shown.

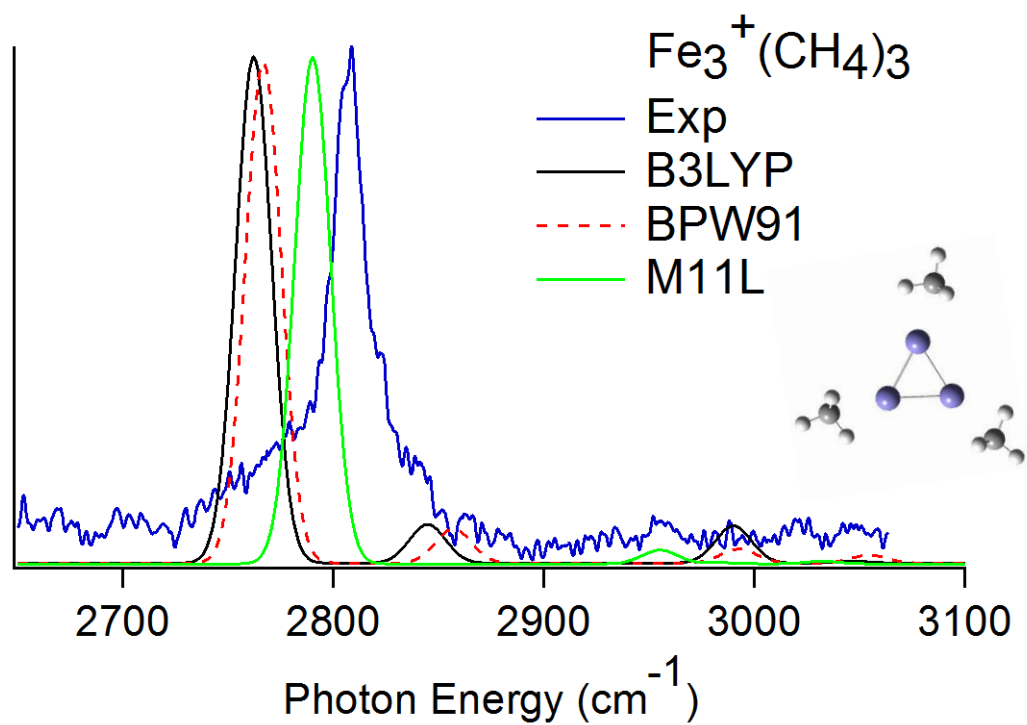


Figure 4.9 Experimental IR photodissociation spectrum of $\text{Fe}_3^+(\text{CH}_4)_3$ along with simulated spectra using B3LYP, BPW91 and M11L functionals and 6-311++G(3df,3pd) basis set. The M11L structure is shown.

is again indicative of a single-photon process. Again, M11L appears to slightly overestimate the binding energy, predicting a binding energy of 2907 cm⁻¹. The calculations predict that the three CH₄ are equivalent, with Fe-C bond lengths of 2.430 Å for B3LYP, 2.469 Å for BPW91 and 2.327 Å for M11L. The B3LYP and BPW91 calculations show hydrogen atom connectivity of η^2 while M11L predicts η^3 . Again, B3LYP and BPW91 predict a similar spectrum, with the major peak at 2773 and 2766 cm⁻¹ respectively. The M11L spectrum has a major peak at 2790 cm⁻¹.

In addition to the major lowest frequency C-H stretch, which dominates the spectrum, the B3LYP and BPW91 simulations also have a small secondary peak ~90 cm⁻¹ higher in energy. This pair of peaks is due to the symmetric and antisymmetric C-H stretches of the proximate hydrogens. This is characteristic of methane complexes with η^2 hydrogen coordination, and is also observed in the calculated and measured spectra of M⁺(CH₄)(Ar)₂ and M⁺(CH₄)₂(Ar) (M=Co, Cu).^{52, 54} The absence of this feature in the Fe₃⁺(CH₄)₃ spectrum, along with a smaller redshift in the lowest frequency C-H stretch, indicates η^3 rather than η^2 hydrogen coordination.

Experimentally, the lowest frequency C-H stretch shows a reduced red shift with increasing number of methanes, moving from 2785 to 2792 to 2809 cm⁻¹ for Fe₃⁺(CH₄)_n (n=1-3). All of the calculations reproduce this trend, but to a varying degree. B3LYP slightly overestimates the observed net shift of 24 cm⁻¹, predicting a change of 30 cm⁻¹. BPW91 and M11L underestimate the net shift, predicting 10 and 8 cm⁻¹ respectively. This trend in the C-H stretching frequency parallels the reduced strength in the metal-methane bond with added ligation, and is due to reduced interaction between the metal and methane. This is also observed in Fe₂⁺(CH₄)_n⁸ and M⁺(CH₄)_n complexes.^{22, 31, 75, 77}

4.3.7 Fe₄⁺(CH₄)₄

The Fe₄⁺(CH₄)_n (n=1-4) clusters are harder to produce than Fe₃⁺(CH₄)_n (n=1-3). Similar to what is observed in the Fe₃⁺(CH₄)_n complexes, the 1:1 Fe₄⁺(CH₄)₄ complex is most abundant, with Fe₄⁺(CH₄) half as intense, and a much smaller yield of Fe₄⁺(CH₄)₂ and Fe₄⁺(CH₄)₃. Fe₄⁺(CH₄) was not observed to photodissociate, which is consistent with the calculated binding energies of >2900 cm⁻¹.

The spectrum of $\text{Fe}_4^+(\text{CH}_4)_4$ (**Figure 4.10**) shows a peak centered around 2795 cm^{-1} with a fwhm of $\sim 30\text{ cm}^{-1}$. The photodissociation yield is 8% at the peak, 4% at the shoulder near 2760 cm^{-1} , and $\sim 2\%$ from 2800 to 3100 cm^{-1} .

The calculations all predict that the ground state of Fe_4^+ has multiplicity $(2S+1) = 12$. With the M11L functional, states with multiplicity of 10 and 14 lie 33 kJ/mol and 55 kJ/mol higher in energy, respectively. This gap changes little with additional methanes. The three functionals predict very different geometries and vibrational spectra for $\text{Fe}_4^+(\text{CH}_4)_4$. The following are the lowest energy geometries obtained even when starting from multiple different starting geometries. The B3LYP structure has three methanes with Fe-C bond lengths of $2.31\text{-}2.32\text{ \AA}$ and η^3 hydrogen coordination and one with an Fe-C bond length of 2.51 \AA and η^2 hydrogen coordination. Because the methanes are not equivalent, the simulated spectrum shows multiple peaks with similar intensity in the $2800\text{-}2900\text{ cm}^{-1}$ region, completely at odds with the measured spectrum. BPW91 calculations predict a very symmetrical structure with Fe-C bond lengths of 2.410 \AA and η^2 hydrogen coordination. These results parallel those of Castro¹⁷ at the BPW91/6-311++G(2d,2p) level. The resulting simulated spectrum is dominated by a peak at 2724 cm^{-1} , which is 71 cm^{-1} below the observed peak.

The M11L calculations also predict a very symmetrical structure, with Fe-C bond lengths of 2.370 \AA and η^3 hydrogen coordination. The resulting spectrum consists of a single peak at 2803 cm^{-1} , in agreement with experiment. The shoulder near 2760 cm^{-1} could be due to a small contribution from higher energy structures with methanes with η^2 hydrogen coordination, or to contribution from bending overtones.⁵² In contrast to $\text{Fe}_3^+(\text{CH}_4)_n$ ($n=1\text{-}3$), the calculations predict that the frequency of the lowest C-H stretch in $\text{Fe}_4^+(\text{CH}_4)_n$ ($n=1\text{-}4$) is nearly independent of the number of methane attached. Thus we would expect that the vibrational spectra of $\text{Fe}_4^+(\text{CH}_4)_n$ ($n=1\text{-}3$) would be very similar to that of $\text{Fe}_4^+(\text{CH}_4)_4$.

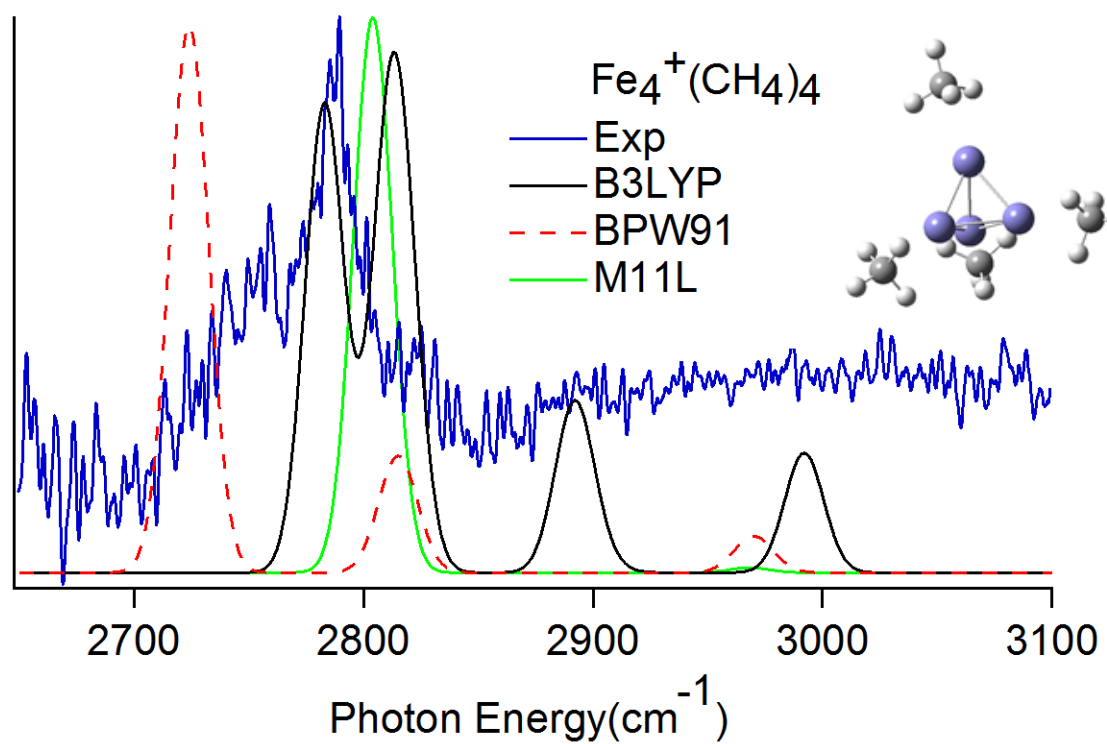


Figure 4.10 Experimental IR photodissociation spectrum of $\text{Fe}_4^+(\text{CH}_4)_4$ along with simulated spectra using B3LYP, BPW91 and M11L functionals and 6-311++G(3df,3pd) basis set. The M11L structure is shown.

4.4 Summary and Conclusions

In summary, the spectra of $\text{Fe}_2^+(\text{CH}_4)_n$ ($n=1-3$), $\text{Fe}_3^+(\text{CH}_4)_n$ ($n=1-3$) and $\text{Fe}_4^+(\text{CH}_4)_4$ are dominated by a single peak corresponding to the lowest C-H stretch. These spectra are all similar to each other. Although all the presented spectra are similar, the $\text{Fe}_3^+(\text{CH}_4)$ spectrum appears to originate from a multiphoton process whereas the other spectra have higher dissociation yields, indicative of a single photon process. The single prominent peak seen in all the spectra suggest a η^3 hydrogen binding configuration, as all calculations predicting a η^2 configuration show a doublet structure which is not seen experimentally. Comparing the different cluster sizes, the monolayer complexes show a trend of an increasing redshift from $\text{Fe}_2^+(\text{CH}_4)_2$ to $\text{Fe}_3^+(\text{CH}_4)_3$ to $\text{Fe}_4^+(\text{CH}_4)_4$, in contrast to what would be expected based on purely electrostatic binding. This suggests increasing covalency in the binding of the larger complexes, which parallels the measured increased reactivity of the bare Fe_x^+ clusters.⁶³ M11L most accurately predicts the experimental spectra of all the larger (Fe_3 and Fe_4) clusters, although it overestimates the methane binding energies to a greater extent than the other functionals.

References

1. Schwarz, H. *Isr. J. Chem.* **2014**, *54*, 1413-1431.
2. O'Hair, R. A. J. *Int. J. Mass Spectrom.* **2015**, *377*, 121-129.
3. Schwarz, H. *Angew. Chem. Intl. Ed.* **2011**, *50*, 10096-10115.
4. Roithova, J. *Chem. Soc. Rev.* **2012**, *41*, 547-559.
5. Roithova, J.; Schröder, D. *Chem. Rev.* **2010**, *110*, 1170-1211.
6. Armentrout, P. B. *Catal. Sci. Tech.* **2014**, *4*, 2741-2755.
7. Irikura, K. K.; Beauchamp, J. L. *J. Phys. Chem.* **1991**, *95*, 8344-8351.
8. Shayesteh, A.; Lavrov, V. V.; Koyanagi, G. K.; Bohme, D. K. *J. Phys. Chem. A* **2009**, *113*, 5602-5611.
9. Chen, Y. M.; Armentrout, P. B. *J. Phys. Chem.* **1995**, *99*, 10775-10779.
10. Albert, G.; Berg, C.; Beyer, M.; Achatz, U.; Joos, S.; Niedner-Schatteburg, G.; Bondybey, V. E. *Chem. Phys. Lett.* **1997**, *268*, 235-241.
11. Lang, S. M.; Bernhardt, T. M.; Barnett, R. N.; Landman, U. *Angew. Chem. Intl. Ed.* **2010**, *49*, 980-983.
12. Lang, S. M.; Bernhardt, T. M.; Barnett, R. N.; Landman, U. *J. Phys. Chem. C* **2011**, *115*, 6788-6795.
13. Schlangen, M.; Schwarz, H. *Catal. Lett.* **2012**, *142*, 1265-1278.
14. Kummerlowe, G.; Balteanu, I.; Sun, Z.; Balaj, O. P.; Bondybey, V. E.; Beyer, M. K. *Int. J. Mass Spectrom.* **2006**, *254*, 183-188.
15. Liyanage, R.; Zhang, X.-G.; Armentrout, P. B. *J. Chem. Phys.* **2001**, *115*, 9747-9763.
16. Schnabel, P.; Irion, M. P. *Ber. Bunsen-Ges. Phys. Chem. Chem. Phys.* **1992**, *96*, 1101-1103.
17. Schnabel, P.; Irion, M. P.; Weil, K. G. *J. Phys. Chem.* **1991**, *95*, 9688-9694.
18. Gehret, O.; Irion, M. P. *Chem. Phys. Lett.* **1996**, *254*, 379-383.
19. Ichihashi, M.; Hanmura, T.; Kondow, T. *J. Chem. Phys.* **2006**, *125*, 133404.
20. Chrétien, S.; Salahub, D. R. *J. Chem. Phys.* **2003**, *119*, 12279-12290.

21. Chrétien, S.; Salahub, D. R. *J. Chem. Phys.* **2003**, *119*, 12291-12300.
22. Rodriguez, O.; Lisy, J. M. *Chem. Phys. Lett.* **2011**, *502*, 145-149.
23. Poad, B. L. J.; Thompson, C. D.; Bieske, E. J. *Chem. Phys.* **2008**, *346*, 176-181.
24. Dryza, V.; Bieske, E. J. *Int. J. Mass Spectrom.* **2010**, *297*, 46-54.
25. Citir, M.; Altinay, G.; Austein-Miller, G.; Metz, R. B. *J. Phys. Chem. A* **2010**, *114*, 11322-11329.
26. Kocak, A.; Sallese, Z.; Johnston, M. D.; Metz, R. B. *J. Phys. Chem. A* **2014**, *118*, 3253-3265.
27. Wheeler, O. W.; Salem, M.; Gao, A.; Bakker, J. M.; Armentrout, P. B. *J. Phys. Chem. A* **2016**, *120*, 6216-6227.
28. Harding, D. J.; Kerpel, C.; Meijer, G.; Fielicke, A. *Angew. Chem. Int. Ed.* **2012**, *51*, 817-819.
29. Metz, R. B. *Int. Rev. Phys. Chem.* **2004**, *23*, 79-108.
30. Husband, J.; Aguirre, F.; Ferguson, P.; Metz, R. B. *J. Chem. Phys.* **1999**, *111*, 1433-1437.
31. Waller, S. E.; Mann, J. E.; Jarrold, C. C. *J. Phys. Chem. A* **2013**, *117*, 1765-1772.
32. Vučković, S.; Svanqvist, M.; Popok, V. N. *Rev. Sci. Instrum.* **2008**, *79*, 073303.
33. Aguirre, F.; Husband, J.; Thompson, C. J.; Stringer, K. L.; Metz, R. B. *J. Chem. Phys.* **2003**, *119*, 10194-10201.
34. Wiley, W. C.; McLaren, I. H. *Rev. Sci. Instrum.* **1955**, *26*, 1150-1157.
35. Altinay, G.; Metz, R. B. *J. Am. Soc. Mass Spectrom.* **2010**, *21*, 750-757.
36. Rothman, L. S.; Jacquemart, D.; Barbe, A.; Benner, D. C.; Birk, M.; Brown, L. R.; Carleer, M. R.; Chackerian, C.; Chance, K.; Coudert, L. H.; Dana, V.; Devi, V. M.; Flaud, J. M.; Gamache, R. R.; Goldman, A.; Hartmann, J. M.; Jucks, K. W.; Maki, A. G.; Mandin, J. Y.; Massie, S. T.; Orphal, J.; Perrin, A.; Rinsland, C. P.; Smith, M. A. H.; Tennyson, J.; Tolchenov, R. N.; Toth, R. A.; Vander Auwera, J.; Varanasi, P.; Wagner, G. *J. Quant. Spec. Radiat. Transfer* **2005**, *96*, 139-204.
37. Frisch, M. J.; Trucks, G. W.; Schlegel, H. B.; Scuseria, G. E.; Robb, M. A.; Cheeseman, J. R.; Scalmani, G.; Barone, V.; Mennucci, B.; Petersson, G. A.; Nakatsuji, H.; Caricato, M.; Li, X.; Hratchian, H. P.; Izmaylov, A. F.; Bloino, J.; Zheng, G.; Sonnenberg, J. L.; Hada, M.; Ehara, M.; Toyota, K.; Fukuda, R.; Hasegawa, J.; Ishida, M.; Nakajima, T.; Honda, Y.; Kitao, O.; Nakai, H.; Vreven, T.; Montgomery Jr., J. A.; Peralta, J. E.; Ogliaro, F.; Bearpark, M.; Heyd, J. J.; Brothers, E.; Kudin, K. N.; Staroverov, V. N.; Keith, T.; Kobayashi, R.; Normand, J.; Raghavachari, K.; Rendell, A.; Burant, J. C.; Iyengar, S. S.; Tomasi, J.; Cossi, M.; Rega, N.; Millam, J. M.; Klene, M.; Knox, J. E.; Cross, J. B.; Bakken, V.; Adamo, C.; Jaramillo, J.; Gomperts, R.; Stratmann, R. E.; Yazyev, O.; Austin, A. J.; Cammi, R.; Pomelli, C.; Ochterski, J. W.; Martin, R. L.; Morokuma, K.; Zakrzewski, V. G.; Voth, G. A.; Salvador, P.; Dannenberg, J. J.; Dapprich, S.; Daniels, A. D.;

Farkas, O.; Foresman, J. B.; Ortiz, J. V.; Cioslowski, J.; Fox, D. J. *Gaussian 09, Revision D.01*, Gaussian, Inc., Wallingford, CT: Pittsburgh PA, 2013.

38. Peverati, R.; Truhlar, D. G. *J. Phys. Chem. Lett.* **2012**, *3*, 117-124.
39. Ashraf, M. A.; Copeland, C. W.; Kocak, A.; McEnroe, A. R.; Metz, R. B. *Phys. Chem. Chem. Phys.* **2015**, *17*, 25700-25704.
40. Copeland, C. W.; Ashraf, M. A.; Boyle, E. M.; Metz, R. B. *J. Phys. Chem. A* **2017**, *121*, 2132-2137.
41. Kocak, A.; Ashraf, M. A.; Metz, R. B. *J. Phys. Chem. A* **2015**, *119*, 9653-9665.
42. Gutsev, G. L.; Weatherford, C. A.; Jena, P.; Johnson, E.; Ramachandran, B. R. *J. Phys. Chem. A* **2012**, *116*, 10218-10228.
43. Gutsev, G. L.; Bauschlicher, C. W., Jr. *J. Phys. Chem. A* **2003**, *107*, 7013-7023.
44. Chiodo, S.; Rivalta, I.; Michelini, M.; Russo, N.; Sicilia, E.; Ugalde, J. M. *J. Phys. Chem. A* **2006**, *110*, 12501-12511.
45. DiLabio, G.; Otero-de-la-Roza, A., Noncovalent Interactions in Density-Functional Theory. In *Reviews in Computational Chemistry*, Parrill, A.; Lipkowitz, K., Eds. John Wiley & Sons, Inc.: Hoboken, NJ, 2016; Vol. 29, pp 1-97.
46. Grimme, S.; Antony, J.; Ehrlich, S.; Krieg, H. *The Journal of Chemical Physics* **2010**, *132*, 154104.
47. Castro, M. *Chem. Phys. Lett.* **2007**, *446*, 333-338.

CHAPTER 5

EXTENSIONS AND FUTURE WORK

5.1 $M^+(H_2O)$ Systems

As discussed in Chapters 1 and 3, the importance of metal ion-water interactions in solvation, catalysis and biology has motivated/inspired many studies.

5.1.1 First-Row Transition Metal-Water Complexes

Our group has carried out electronic and vibrational spectroscopy studies on $Ni^+(H_2O)$,²⁸ $Co^+(H_2O)$,⁵³ and $Mn^+(H_2O)$.⁴⁶ The Duncan group has covered the vibrational spectroscopy of the remainder of the first-row transition metals using Ar tagging, including $Sc^+(H_2O)$ ¹⁵, $Ti^+(H_2O)$,¹⁰⁶ $V^+(H_2O)$,¹⁰² $Cr^+(H_2O)$,¹³ $Fe^+(H_2O)$,¹⁰⁴ $Cu^+(H_2O)$,¹⁶ and $Zn^+(H_2O)$.¹⁰ This covers all the first-row transition metals' vibrational studies, although excited states can still be looked at using electronic spectroscopy. When selecting candidates for electronic spectroscopy, the number and closeness of predicted excited states is crucial in deciding if spectroscopy is likely to give results with good structural information. A likely candidate for a future study would thus be $Fe^+(H_2O)$, although the spectrum may not be as sharp as that of $Mn^+(H_2O)$ presented here due to multiple excited states lying in close proximity.

5.1.2 Second-Row and Third-Row Transition Metal-Water Complexes

The next logical studies after first-row transition metal water complexes should consider comparisons of the first-row metal complexes to the second and third-row complexes of the same groups. An experiment that may now be possible that we tried previously is the photodissociation of $Au^+(H_2O)$ in the IR. In the past we tried to do electronic spectroscopy on $Au^+(H_2O)$ for a long period of time and found that we were unable to make the molecule dissociate. With the modifications carried out since the previous H_2O experiments we may be able to make more of the parent and better cancel noise, and so this may allow us to observe photodissociation even if the percent dissociation is small.

5.1.3 Metal Cluster Ion-Water Complexes

Cluster studies with multiple H₂O attached can be done for any of these complexes, but due to the likely complexity of the spectra and lack of information able to be gained from lack of sharpness due to many similar energy excited states, these studies should mostly be aimed in the IR region utilizing vibrational spectroscopy instead of electronic spectroscopy. A more productive route may be instead of looking at a metal with multiple waters M⁺(H₂O)_n one could instead look at multiple metal atoms with one ligand M_x⁺(H₂O). Like what was mentioned above, certain metals may be better candidates, due to having fewer excited states that are close in energy. A good first candidate for a metal cluster with one H₂O study would be Ni₂⁺ and Ni₃⁺, which have shown size dependent reactivity with alkanes.⁶²

5.2 M⁺(CH₄)

As discussed in Chapters 1 and 4, the activation of methane has been studied for several metal ions, it is worth extending this work to other transition metal ions since they may have interesting reactivity. Therefore, these studies can be extended in several directions, including most apparently to other metals and as performed in this work, to other metal cluster ions.

5.2.1 M_x⁺(CH₄)_n Clusters

The instrument modifications described in Chapter 4 allow us to produce complexes of metal cluster ions with methane. In addition to iron, cluster ions of several metals show interesting size-dependent reactivity^{24, 56, 62} and are thus good candidates for spectroscopic studies of their complexes with methane. Study of these molecules would offer insight into periodic trends and more specifically how different metal clusters reactivity and other characteristics change depending on the particular metal and the cluster size. These clusters could include Cu_x⁺(CH₄)_n, Ag_x⁺(CH₄)_n, Ni_x⁺(CH₄)_n, and Co_x⁺(CH₄)_n, which have been studied in the IR by our group in the single metal case.^{8, 25, 52, 54} Fe₄⁺(CH₄)_n (n=1-3) clusters could be revisited later if greater ion cluster creation is realized and mass gating serves to reduce noise.

5.2.2 First-Row Metal Methane Complexes

Thus far, half of the first-row transition metal-methane complexes have been studied in the IR. These are $\text{Mn}^+(\text{CH}_4)_n$,³¹ $\text{Fe}^+(\text{CH}_4)_n$,^{8, 25} $\text{Co}^+(\text{CH}_4)_n$,⁵⁴ $\text{Ni}^+(\text{CH}_4)_n$ ⁵⁴ and $\text{Cu}^+(\text{CH}_4)_n$.⁵² This leaves the early first-row transition metals as well as $\text{Zn}^+(\text{CH}_4)$ which have yet to be studied. The predicted reactivity is fairly low for the early metals, but studies should be able to be performed fairly easily for $\text{Sc}^+(\text{CH}_4)$, $\text{Ti}^+(\text{CH}_4)$, $\text{V}^+(\text{CH}_4)$ and $\text{Cr}^+(\text{CH}_4)$. The ability of the early metals to more readily accept electron donation into empty d orbitals may lead to stronger interactions with methane than the late metals. Some possible issues are that these metals may get an oxidized coating that will require ablating off over time, and the brittleness of the metals may cause issues with the rod. As for $\text{Zn}^+(\text{CH}_4)$, as it is $3d^{10}4s^1$ vs the $3d^{10}$ of $\text{Cu}^+(\text{CH}_4)$, it is predicted to be very similar but even less reactive.

5.2.3 Second-Row and Third-Row Metal Methane Complexes

These studies can of course be extended from the first-row transition metals to the second-row and third-row transition metals to examine/study periodic trends. This has been done in our group for $\text{Cu}^+(\text{CH}_4)_n$ vs $\text{Ag}^+(\text{CH}_4)_n$ ($n=1-6$).⁵² Although differences seen were mostly due to a difference in geometry as more methane were attached ($n>4$) with the different ionic radii of the metals being the cause, it may be interesting to see if this trend continues for other transition metal groups. Combining this direction with already studied first-row transition metals, the study of a group of transition metals, such as $\text{Cr}^+(\text{CH}_4)_n$, $\text{Mo}^+(\text{CH}_4)_n$, and $\text{W}^+(\text{CH}_4)_n$ may be of interest. Another similar option that also uses fairly cheap and accessible metals is the nearby trend of $\text{V}^+(\text{CH}_4)_n$, $\text{Nb}^+(\text{CH}_4)_n$ and $\text{Ta}^+(\text{CH}_4)_n$.

5.2.4 First-Row Metal-Alkane Complexes

Recently, we have attempted to study a series of alkanes bound to Al^+ . The spectra thus far are much more complicated, mostly owing to multiple geometry configurations that are similar in energy which are significantly populated, making the spectra a combination of two or more configurations, each with different peaks. Despite the rich spectrum, by using different functionals and adjustments to theory, and accounting for the varying composition due to different amounts of each isomer, the

spectrum can be simulated accurately. This bodes well for future studies of ethane with other metals, as well as eventually the increasingly complicated IR studies that would result from propane or larger alkanes. These studies can be extended to clusters of the alkane ligands as well, although this will also complicate the spectra and it may become too broad with too many configurations for a good analysis that yields substantial information. Metals that have one or few stable isotopes would be good choices for further studies with these complexes as it would not further complicate the spectra.

5.2.5 Metal-Methane Ar Tagging

Additionally, with the increased ability to generate clusters, provided enough signal can be produced, clusters can be Ar tagged to photodissociate molecules that may be too strongly bound. This is an alternative solution to having to photodissociate via IRMPD, which is typically very ineffective when compared to standard photodissociation yields (0.2 % vs. 12% for example in $\text{Fe}_3^+(\text{CH}_4)$ vs $\text{Fe}_3^+(\text{CH}_4)_{2,3}$).

5.3 TOFMS Instrument Modifications

To study the $\text{Fe}^+(\text{CH}_4)$ clusters as presented in this work, modifications to the instrument had to be made to produce a usable amount of signal (>100 mV). These alterations, as discussed previously, (Chapter 2) included the introduction of a second pulsed valve to introduce pure CH_4 just after ablation, and custom flight nozzles to induce collisions and make more of as well as new, larger clusters. Although these were effective in enabling the creation of the larger clusters in appreciable amounts, the mass spectrum becomes more and more congested at higher masses, due to a larger array of ions being available. An example if this would include small numbers of irons with large numbers of methanes arriving close in time to larger amounts of irons with fewer methanes attached. Partially because of this congestion, when we attempted to photodissociate $\text{Fe}_4^+(\text{CH}_4)_2$, which had ~60 mV of signal, no net fragment could be seen above the background due to similar massed parent ions.

5.3.1 Second Mass Gate Introduction

To solve this problem of noise and see whether an ion, for example $\text{Fe}_4^+(\text{CH}_4)_2$ as mentioned above is dissociating, there are a few options. One option is to produce enough of the ion that even a small amount of dissociation would be seen despite background. Another option is to find ways to reduce the background, such as changing conditions to try to only make larger ions or cooling ions to make the photodissociation spectrum sharper. These steps typically only help slightly. Therefore, aiming to reduce background is a lucrative option. The method of reducing background that was chosen was to introduce a second mass gate later in the flight tube, allowing another level of selectivity. By doing this, the region in the time of flight spectrum just before the ion of interest should be cleaner as ions not of interest that may interfere with fragment signal will be eliminated or reduced significantly. As the ions separate in time based on mass to charge ratio, we can pulse the mass gate to eliminate ions that are not at our mass of interest. The tradeoff here is that this can lower the signal of the parent ion we want to see in order to reduce the ions that we are trying to discriminate against, which limits the usefulness of the practice. By using two mass gates and allowing the ions to separate in time twice, we can eliminate more ions of similar mass without hurting the parent as much as we would need to in order to get the same result from just one mass gate. This can be vital in obtaining usable data from ions that we may not be producing enough of or that aren't dissociating with a high yield and thus are not being strongly observed above the background. The mass gate's ability to cancel noise is demonstrated using $\text{Cr}^+(\text{NH}_3)$ ion in **Figure 5.1**.

The mass gate was designed by combining elements of ones published by Kappes⁹⁴ and Enke.¹⁰⁰ It consists of two interleaved rows of thin, closely spaced wires. The underlying structure of the custom mass gate is shown in **Figure 5.2**, with the assembled product with fully tensioned wires in **Figure 5.3**. When the wires are at ground potential, ions pass freely between them. To remove ions in a particular mass range, the ions are deflected by pulsing one set of wires to a positive voltage, while the

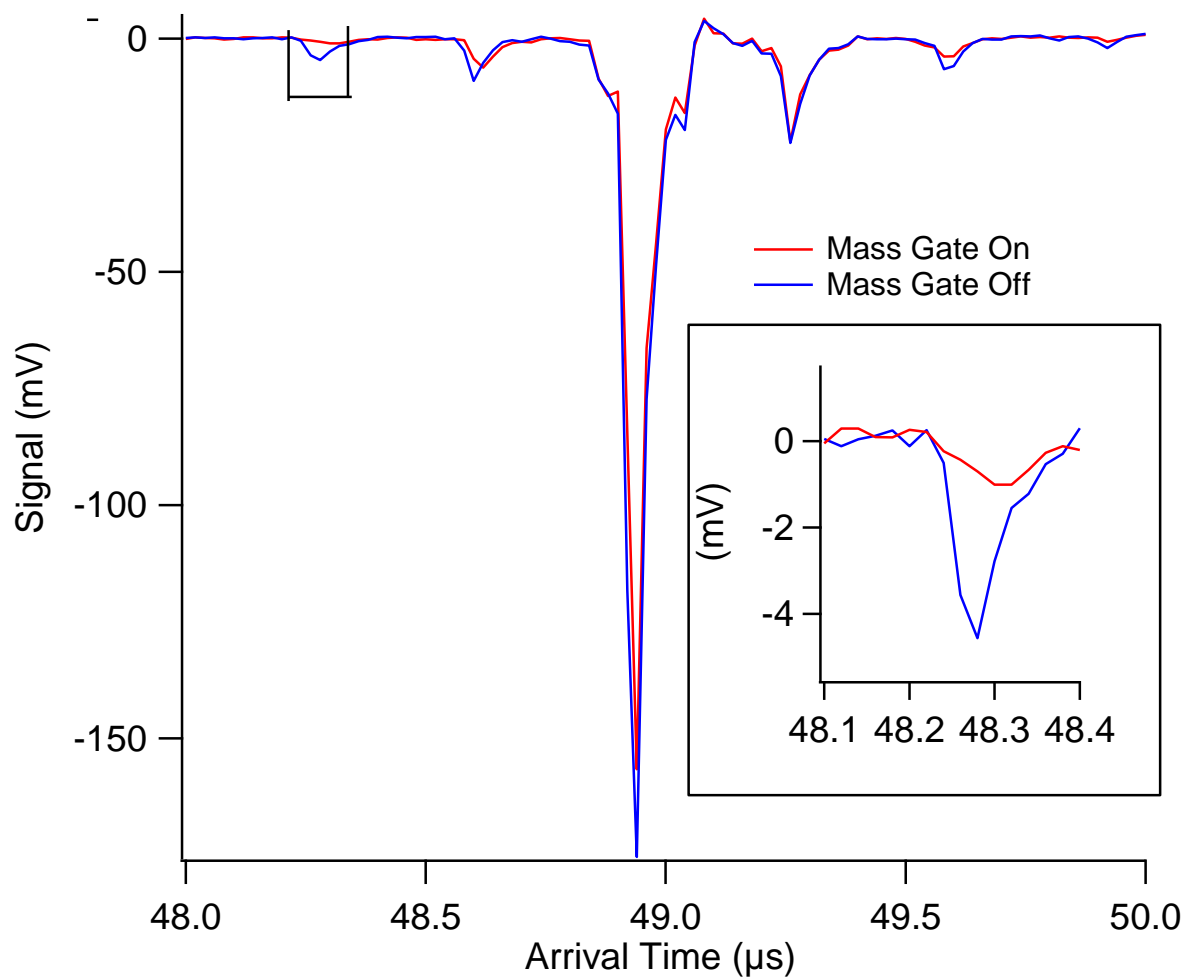


Figure 5.1: Mass spectrum of $\text{Cr}^+(\text{NH}_3)$. Here the difference between second mass gate turned off (blue) vs. turned on (red) is seen. The width of the high voltage pulse is 890 ns and the potentials are ± 100 V. When the mass gate is turned on background close to the parent (in this example ~ 0.6 μs away) can be eliminated. This allows photofragments that might otherwise be hidden under the (blue) background to be seen.



Figure 5.2: Custom mass gate structure before complete assembly. The wires are wrapped along metal and plastic screws to hold the lines in place as the mass gate will not function if they touch or are too close. The wires are ordered so that a positive pulse (coming from a wire that inserts between the nuts and the outer plastic for the metal rods) goes through the first wire on the left with the next wire having a negative pulse, and the wire after that again being positive and this pattern repeats across the lines. The main body is made from nylon, and the nuts can be adjusted to keep strong tension on the wires. In the photo, they are not yet fully tensioned.



Figure 5.3: Custom mass gate after complete assembly. In this photo, the structure seen in Figure 5.2 is fully assembled and the is mounted between two stainless steel plates kept at ground potential. The final mounting and tightening of the plates results in the wires being fully tensioned. The molecular beam passes through the gap in the middle but purposely goes wide of the device when returning from the reflectron before arriving at the detector.

other set is pulsed to the equivalent negative voltage. In **Figure 5.1** it is shown that background as close as 0.6 μs to the parent can be eliminated while having almost no impact on the parent ions' signal.

5.3.2 Modular Nozzle Assembly and Other Adjustments

Other things to consider when attempting to create a better system for making clusters are the sections immediately following ablation. Keeping the same internal diameter of exit nozzle on the faceplate as is used in the subsequent nozzle assembly has been seen to result in the most consistent ions and most stable signal. This is opposed to an assembly where the internal diameter between parts changes to create 'waiting rooms' for ions, which we found did not work well for our studies. From experiment, (Chapter 2) it was observed that the longer the nozzle section the larger and often more of the clusters that were produced. This makes sense, as these long nozzles allow more time for collisions to take place and large clusters to form. By altering the total length of the nozzle assembly, the relative size of the dominant clusters created can be controlled to a degree. As this is very beneficial, alterations should be attempted to see if more control over the cluster size distribution is possible. Conical nozzles of differing angles are used to complete the nozzle assembly in most setups. The implementation of conical nozzles with different angles could affect the distribution⁹⁵ or number of clusters substantially, and is probably worth investigating as the machining and swapping out process is simple.

The implementation and design of the nozzle system in collaboration with a second pulsed valve that introduces pure reactant has worked quite well as seen in Chapter 2 and 3. The valve itself seems to work well, and a better design to the valve or valve housing that links it to the modular nozzle assembly doesn't seem like a route that will significantly improve results. However, looking at the section after ablation but before the skimmer may give opportunities for improvement. In the past,

we attempted to reduce water contamination in the instrument by introducing a faceplate with a cooling channel through which liquid nitrogen flowed. This reduced the water background but when the water contamination was fixed this cooling system was removed, as it was deemed no longer necessary. With the introduction of new components to facilitate cluster formation, and the dependence seen on how large the clusters formed are as a function of nozzle length, new setups can be tried.

The simplest alteration to try is to simply pull the source block back further from the skimmer, to allow for space to increase the total nozzle assembly length further. The longer the nozzle section, the more time for ions to undergo collisions and the larger and more clusters we are likely to see. Another approach to try is to either machine a new faceplate that can have liquid nitrogen flowing through it, or to make nozzles that work with the liquid nitrogen cooled faceplate that already exists. It would be interesting to see if cooling the source with liquid nitrogen would strongly affect the clusters that are formed, or their vibrational temperature.

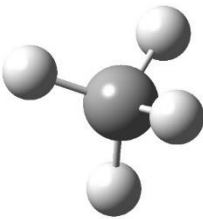
References


1. Daluz, J. S.; Kocak, A.; Metz, R. B. *J. Phys. Chem. A* **2012**, *116*, 1344-1352.
2. Kocak, A.; Geoff, A.; Pearson III, W.; Altinay, G.; Metz, R. *J. Phys. Chem. A* **2013**, *117*, 1254-1264
3. III, W. L. P.; Copeland, C.; Kocak, A.; Sallese, Z.; Metz, R. B. *J. Chem. Phys* **2014**, *141*, 204305.
4. Carnegie, P. D.; Bandyopadhyay, B.; Duncan, M. A. *J. Chem. Phys.* **2011**, *134*, 014302.
5. Ward, T. B.; Carnegie, P. D.; Duncan, M. A. *I. Chem. Phys. Lett.* **2016**, *654*, 1-5.
6. Walker, N. R.; Walters, R. S.; Pillai, E. D.; Duncan, M. A. *J. Chem. Phys.* **2003**, *119*, 10471-10474.
7. Carnegie, P. D.; Bandyopadhyay, B.; Duncan, M. A. *I. J. Phys. Chem. A* **2008**, *112*, 6237-6243.
8. Walters, R. S.; Duncan, M. A. *Aust. J. Chem.* **2004**, *57*, 1145-1148.
9. Carnegie, P. D.; McCoy, A. B.; Duncan, M. A. *J. Phys. Chem. A* **2009**, *113*, 4849-4854.
10. Bandyopadhyay, B.; Reishus, K. N.; Duncan, M. A. *J. Chem. Phys. A* **2013**, *117*, 7794-7803.
11. Liu, F. Y.; Zhang, X. G.; Liyanage, R.; Armentrout, P. B. *J. Chem. Phys.* **2004**, *121*, 10976-10990.
12. Citir, M.; Liu, F.; Armentrout, P. B. *J. Chem. Phys.* **2009**, *130*, 054309-16.
13. Kummerlowe, G.; Balteanu, I.; Sun, Z.; Balaj, O. P.; Bondybey, V. E.; Beyer, M. K. *Int. J. Mass Spectrom.* **2006**, *254*, 183-188.
14. Copeland, C. W.; Ashraf, M. A.; Boyle, E. M.; Metz, R. B. *J. Phys. Chem. A* **2017**, *121*, 2132-2137.
15. Ashraf, M. A.; Copeland, C. W.; Kocak, A.; McEnroe, A. R.; Metz, R. B. *Phys. Chem. Chem. Phys.* **2015**, *17*, 25700-25704.
16. Kocak, A.; Ashraf, M. A.; Metz, R. B. *J. Phys. Chem. A* **2015**, *119*, 9653-9665.
17. Kocak, A.; Sallese, Z.; Johnston, M. D.; Metz, R. B. *J. Phys. Chem. A* **2014**, *118*, 3253-3265.
18. Dryza, V.; Bieske, E. J. *Int. J. Mass Spectrom.* **2010**, *297*, 46-54.
19. Stoermer, C. W.; Gilb, S.; Friedrich, J.; Schooss, D.; Kappes, M. M. *Rev. Sci. Instrum.* **1998**, *69*, 1661-1664.
20. Vlasak, P. R.; Beussman, D. J.; Davenport, M. R.; Enke, C. G. *Rev. Sci. Instrum.* **1996**, 68-72.

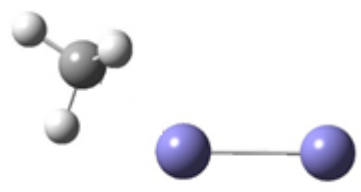
21. Stone, J. A.; Vukomanovic, D. *Int. J. Mass Spectrom.* **1999**, *185*, 227-229.

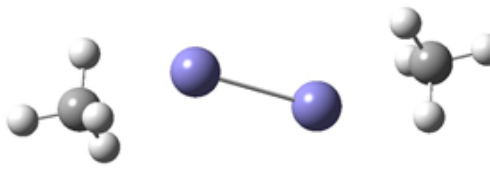
APPENDIX A
LOWEST ENERGY GEOMETRIES, ENERGIES, VIBRATIONAL FREQUENCIES
AND INTENSITIES CALCULATED AT THE M11L/6-311++G(3df,3pd) LEVEL

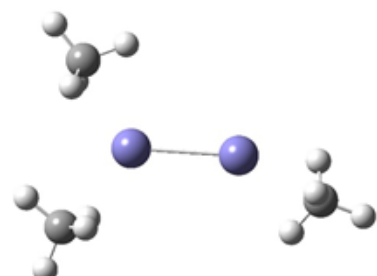
Table A1. Calculated M11L/6-311++G(3df,3pd) structures, vibrational frequencies and intensities for Fe_x^+ (CH_4)_n; x=2-4, n=1-3 using Gaussian09(RevE.01). Frequencies (in cm^{-1}) are unscaled (used 0.971 for M11L in previously detailed work); intensities are in km/mol .

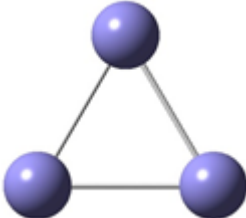
CH₄		
Multiplicity	E(no ZPE, Hartree)	E(w/ZPE,Hartree)
1	-40.525475	-40.481474
		

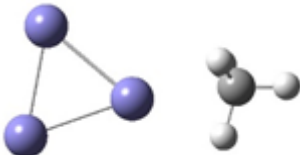
Fe₂⁺						
Multiplicity	E(no ZPE, Hartree)	E(w/ZPE,Hartree)	Fe	0	0	1.16642
			Fe	0	0	-1.16642
8	-2527.259065	-2527.258735				
						

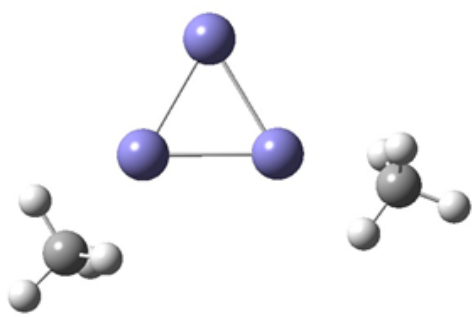
Fe₂⁺(CH₄)						
Multiplicity	E(no ZPE, Hartree)	E(w/ZPE, Hartree)				
8	-2567.810581	-2567.765204	Fe	-0.675702	-0.410218	0.000002
			Fe	1.727031	0.188387	0.000001
			C	-2.715312	0.572714	0.000011
			H	-2.792166	-0.530409	-0.00079
			H	-2.250195	0.971293	0.914058
			H	-3.750345	0.917956	0.000137
			H	-2.249974	0.972489	-0.91351
				H		
Frequency (Intensity) 49.2 (0.1), 62.1 (1.1), 148.3 (0.4), 206.7 (6.2), 236.4 (0.3), 320.2 (0.2), 1224.3 (73.6), 1285.1 (14.5), 1304.8 (17.3), 1496.1 (12.6), 1514.0 (16.7), 2859.7 (20.8), 3030.6 (4.5), 3063.4 (0.1), 3117.3 (4.3)						

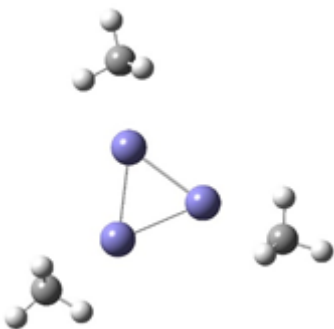
Fe₂⁺(CH₄)₂									
Multipl icity	E(no ZPE, Hartree)	E(w/ZPE, Hartree)	Fe	1.205822	-0.451764	0.023545			
			Fe	-1.205835	0.451811	0.023539			
8	-2608.35447	- 2608.2619 12	C	-3.337812	-0.422100	-0.06071			
			H	-3.190954	0.113517	0.892298			
			H	-3.152465	0.20508	-0.94907			
			H	-2.772142	-1.361782	-0.09549			
			H	-4.399968	-0.669678	-0.09557			
			H	2.772269	1.361729	-0.09513			
			C	3.337847	0.421978	-0.06071			
			H	4.400025	0.669461	-0.09559			
			Frequency (Intensity) 18.0 (1.6), 28.1 (0.6), 46.2 (0.0), 53.9 (0.2), 70.6 (0.0), 151.3 (0.0), 180.7 (16.5), 202.5 (0.0), 257.9 (1.0), 261.4 (0.0), 298.3 (0.0), 314.6 (0.1), 1228.2 (136.7), 1232.3 (0.1), 1284.5 (25.5), 1284.8 (0.0), 1305.0 (0.1), 1306.0 (38.3), 1504.2 (28.8), 1504.4 (0.1), 1510.6 (28.3), 1510.9 (0.1), 2867.3 (38.8), 2868.5 (0.1), 3033.2 (0.1), 3034.7 (0.6), 3071.5 (2.4), 3071.8 (0.0), 3119.5 (1.1), 3119.6 (0.0)						

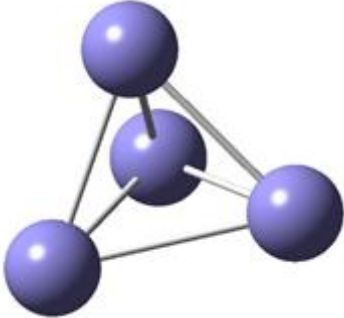
Fe ₂ ⁺ (CH ₄) ₃									
Multi plicity	E(no ZPE, Hartree)	E(w/ZPE,Hart ree)	Fe	1.51397	-0.307954	-0.14402			
8	-2648.890858	-2648.755087	Fe	-1.035949	0.010631	0.003697			
			H	3.39871	-0.3771	0.946069			
			C	3.623724	0.44287	0.242882			
			H	3.500303	0.155569	-0.81641			
			H	3.072108	1.35979	0.489406			
			H	4.687453	0.652579	0.363273			
			C	-2.334247	2.165989	0.000249			
			H	-2.534554	3.238297	-0.00266			
			H	-3.284021	1.628675	0.004176			
			H	-1.763244	1.962633	-0.91817			
			H	-1.759327	1.968252	0.917488			
			H	-2.68553	-1.294482	-0.82354			
			C	-2.536863	-1.842776	0.119597			
			H	-3.35829	-2.558126	0.186652			
			H	-2.623516	-1.200923	1.01079			
			H	-1.594306	-2.401253	0.114915			
			Frequency (Intensity) 70.8 (1.0), 25.8 (1.3), 41.0 (1.8), 52.6 (0.0), 59.2 (0.4), 75.2 (0.2), 87.1 (0.0), 102.7 (0.1), 116.1 (0.5), 136.8 (1.7), 170.7 (13.1), 173.9 (11.3), 192.5 (7.1), 231.5 (0.4), 250.4 (2.3), 296.2 (0.5), 313.8 (0.1), 323.6 (0.6), 1230.3 (42.4), 1233.8 (102.6), 1239.3 (17.8), 1282.1 (22.8), 1283.4 (12.6), 1286.7 (6.2), 1304.3 (15.8), 1308.0 (27.7), 1315.5 (16.0), 1502.9 (19.9), 1504.2 (9.6), 1510.5 (5.8), 1512.4 (12.9), 1513.0 (2.7), 1513.5 (21.4), 2858.4 (13.5), 2884.9 (25.5), 2898.3 (50.3), 3012.3 (10.1), 3052.2 (0.2), 3059.4 (0.4), 3064.6 (0.1), 3086.0 (0.0), 3102.3 (5.0), 3119.8 (0.2), 3123.3 (0.1), 3146.3 (0.4)						

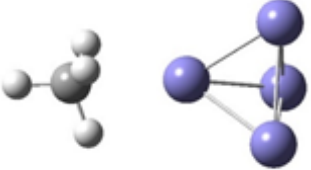
Fe₃⁺						
Multiplicity		E(no ZPE, Hartree)	E(w/ZPE,Hartree)	Fe		
10		-3791.084932	-3791.083739	0.000000	1.382244	0
				1.197079	-0.691129	0
				-1.197079	-0.691116	0
						

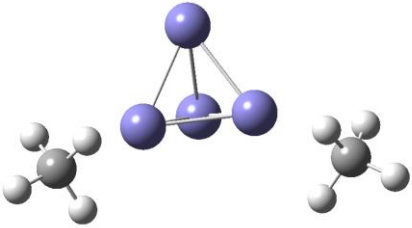
Fe₃⁺(CH₄)						
Multiplicity		E(no ZPE, Hartree)	E(w/ZPE,Hartree)	Fe		
10		-3831.627797	-3831.581571	0.974842	-0.253902	-0.06193
				-0.890585	1.313068	0.00749
				-1.336614	-1.059651	0.023894
				3.239619	0.002214	0.079252
				2.885792	0.550464	0.964394
				2.943032	0.495103	-0.85977
				2.96503000	-1.06686	0.107513
				4.329736	0.020646	0.106614
						
Frequency (Intensity) 40.9 (0.7), 47.4 (0.4), 54.4 (0.9), 146.9 (0.0), 159.0 (2.4), 178.4 (0.7), 198.9 (8.2), 233.0 (0.8), 307.6 (0.3), 1235.9 (64.2), 1286.3 (14.1), 1301.1 (15.9), 1503.1 (13.5), 1513.6 (18.3), 2864.9 (22.2), 3036.6 (0.7), 3061.0 (0.0), 3122.0 (1.7)						

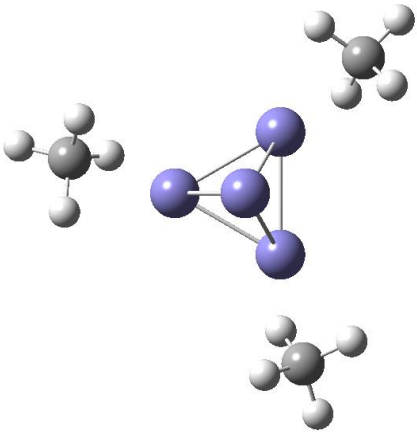
Fe ₃ ⁺ (CH ₄) ₂							
Multi plicity	E(no ZPE, Hartree)	E(w/ZPE,Hart ree)					
10	-3872.169787	-3872.078286	Fe	-1.354424	-0.06381	-0.00054	
			Fe	0.261997	1.770042	0.000871	
			Fe	1.077198	-0.521882	-0.00212	
			C	-3.108284	-1.546927	0.001766	
			H	-2.546488	-1.799011	-0.90984	
			H	-3.469714	-0.503891	0.000201	
			H	-2.545492	-1.79601	0.91360	
			H	-4.005984	-2.166216	0.003348	
			C	3.148867	-1.514891	0.002828	
			H	2.334666	-2.260174	-0.03336	
			H	3.175005	-0.875644	-0.89159	
			H	3.139461	-0.924024	0.930383	
			H	4.070991	-2.097235	0.006043	
	Frequency (Intensity) 31.9 (1.1), 40.3 (1.2), 42.8 (1.4), 63.4 (0.0), 65.1 (0.6), 77.1 (0.0), 146.7 (0.2), 151.0 (0.2), 175.2 (4.1), 198.9 (13.8), 208.1 (2.9), 215.4 (0.0), 251.4 (0.0), 306.5 (0.4), 315.4 (0.7), 1237.7 (90.9), 1240.4 (34.7), 1285.1 (16.6), 1286.6 (11.0), 1301.2 (19.9), 1301.4 (11.4), 1501.3 (24.3), 1503.8 (1.9), 1515.0 (21.8), 1516.8 (14.1), 2866.9 (25.4), 2867.7 (13.1), 3037.4 (0.7), 3039.8 (0.8), 3062.8 (0.0), 3066.5 (0.0), 3122.2 (0.3), 3122.5 (0.4)						

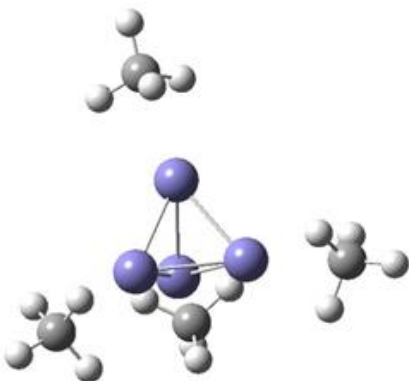
Fe ₃ ⁺ (CH ₄) ₃						
Multi plicity	E(no ZPE, Hartree)	E(w/ZPE,Hart ree)				
10	-3912.709924	-3912.57302	Fe	0.559229	1.304326	-0.0003
			Fe	0.849985	-1.13657	-0.00038
			Fe	-1.409345	-0.167866	-0.00108
			C	0.784093	3.620604	0.002117
			H	0.194857	3.420316	-0.90362
			H	1.757408	3.100152	-0.00696
			H	0.208846	3.414882	0.915686
			H	1.023336	4.684678	0.00366
			C	2.743834	-2.489012	0.001093
			H	2.854851	-1.886364	0.913385
			H	3.54619	-3.227744	0.00214
			H	1.806876	-3.072296	-0.00507
			H	2.862688	-1.880091	-0.906000
			C	-3.52755	-1.131306	0.001302
			H	-3.56374	-0.028228	-0.00735
			H	-3.059543	-1.541056	-0.90465
			H	-3.061894	-1.527049	0.914695
			H	-4.568722	-1.456081	0.002613
						
Frequency (Intensity) 32.6 (3.3), 43.2 (1.5), 44.0 (0.2), 44.3 (1.5), 52.3 (0.0), 60.5 (0.0), 73.3 (0.0), 74.4 (0.0), 75.6 (0.0), 149.5 (0.2), 149.6 (0.2), 154.0 (0.0), 186.8 (16.4), 186.9 (16.3), 210.6 (0.0), 219.9 (0.0), 247.7 (0.0), 250.0 (0.0), 309.6 (0.8), 312.2 (0.8), 321.1 (0.0), 1241.0 (91.1), 1242.1 (93.8), 1245.9 (1.9), 1285.3 (22.2), 1286.1 (12.0), 1286.6 (4.8), 1301.4 (19.6), 1301.7 (22.2), 1301.9 (5.2), 1502.3 (38.8), 1504.0 (0.2), 1504.6 (0.6), 1518.0 (25.9), 1518.1 (25.7), 1518.9 (0.2), 2872.9 (26.5), 2873.1 (26.9), 2874.0 (0.4), 3043.1 (0.6), 3043.4 (0.7), 3043.6 (0.1), 3072.8 (0.1), 3073.1 (0.0), 3073.4 (0.0), 3122.9 (0.1), 3122.9 (0.1), 3123.1 (0.0)						

Fe ₄ ⁺					
Multiplicity	E(no ZPE, Hartree)	E(w/ZPE, Hartree)	Fe		
			Fe	0.050285	1.166062 0.775852
			Fe	-0.050285	-1.166067 0.775845
12	-5054.889958	-5054.887404	Fe	1.214021	-0.048296 -0.77585
			Fe	-1.214022	0.048301 -0.77585
					

Fe ₄ ⁺ (CH ₄)					
Multiplicity	E(no ZPE, Hartree)	E(w/ZPE, Hartree)	Fe		
			Fe	-0.679058	-1.228611 -0.70125
			Fe	1.068717	0.090822 0.020055
12	-5095.430743	-5095.383071	Fe	-0.866019	-0.081581 1.28011
			Fe	-0.836665	1.21516 -0.62480
			C	3.399168	0.01066 0.066731
			H	3.048864	-0.882468 0.603552
			H	3.091561	0.942543 0.564528
			H	3.114843	-0.004413 -0.99534
			H	4.488391	-0.010166 0.099793
			Frequency (Intensity) 39.0 (1.2), 42.6 (0.5), 44.8 (1.1), 120.1 (2.9), 150.4 (0.1), 165.7 (3.4), 175.9 (0.7), 205.5 (6.9), 218.0 (15.5), 229.1 (0.0), 237.0 (0.4), 305.0 (1.0), 1236.3 (75.5), 1292.0 (15.9), 1295.4 (18.0), 1508.7 (16.0), 1511.2 (17.1), 2885.3 (23.6), 3063.1 (0.1), 3069.7 (0.1), 3131.0 (1.9)		

Fe₄⁺(CH₄)₂						
Multipl icity	E(no ZPE, Hartree)	E(w/ZPE,Hart ree)				
12	- 5135.9718606 8	-5135.879203	Fe	-1.153736	0.435471	0.128792
			Fe	1.153772	0.435429	-0.128713
			Fe	-0.131841	-1.142184	-1.214053
			Fe	0.131797	-1.142327	1.213960
			C	3.051132	1.829178	-0.008980
			H	2.513662	2.058265	-0.941275
			H	2.448191	2.053835	0.881667
			H	3.434283	0.799497	0.002264
			H	3.917293	2.490231	0.016917
			C	-3.051116	1.829183	0.009024
			H	-3.917156	2.490388	-0.017040
			H	-2.448405	2.053221	-0.881944
			H	-3.434422	0.799554	-0.001490
			H	-2.513336	2.058742	0.941025
						
Frequency (Intensity) 30.7 (0.6), 34.2 (1.7), 35.6 (0.1), 36.3 (0.3), 40.2 (0.5), 42.3 (1.8), 136.0 (1.7), 141.4 (0.2), 150.2 (0.1), 170.8 (2.6), 183.1 (5.4), 203.7 (6.3), 222.1 (5.0), 224.4 (0.0), 226.1 (15.9), 234.2 (0.3), 234.3 (2.7), 304.1 (1.9), 1238.0 (101.0), 1240.8 (50.0), 1292.6 (12.5), 1292.9 (14.9), 1294.3 (5.0), 1294.4 (34.7), 1508.4 (14.7), 1509.2 (12.4), 1512.7 (25.7), 1512.9 (9.0), 2889.2 (28.4), 2890.1 (16.4), 3065.4 (0.1), 3065.6 (0.1), 3076.0 (0.0), 3076.1 (0.1), 3131.8 (0.7), 3131.9 (0.4)						

Fe₄⁺(CH₄)₃						
Multipl icity	E(no ZPE, Hartree)	E(w/ZPE,Hart ree)				
12	-5176.512500	-5176.374823	Fe	0.674648	1.164780	-0.181207
			Fe	-1.345996	0.001750	-0.181468
			Fe	-0.000443	0.000360	1.802409
			Fe	0.671514	-1.166639	-0.180770
			C	-3.361173	0.665465	-1.085417
			H	-3.177525	1.408673	-0.297196
			H	-2.610555	0.722924	-1.888430
			H	-3.456906	-0.354549	-0.677712
			H	-4.324770	0.899141	-1.537998
			C	2.257520	2.577481	-1.085132
			H	2.941786	3.294926	-1.537914
			H	1.419921	3.170286	-0.681580
			H	2.807997	2.050124	-0.293771
			H	1.935405	1.895715	-1.886992
			C	1.104356	-3.243598	-1.084845
			H	2.035303	-2.817126	-0.675843
			H	0.368008	-3.456463	-0.297547
			H	0.680366	-2.621547	-1.887878
			H	1.383928	-4.194695	-1.537855
			Frequency (Intensity) 31.3 (0.1), 40.5 (1.2), 41.2 (2.2), 41.6 (1.2), 49.5 (1.0), 50.8 (0.9), 58.4 (0.0), 61.4 (0.0), 72.6 (0.0), 126.8 (0.8), 128.2 (0.7), 154.4 (0.3), 154.5 (0.3), 165.2 (0.4), 182.0 (7.5), 200.3 (12.4), 200.8 (12.3), 232.1 (1.3), 239.0 (1.0), 240.9 (0.8), 258.2 (0.9), 272.7 (0.8), 274.4 (0.5), 278.9 (0.4), 1244.9 (84.3), 1245.5 (83.2), 1249.0 (27.2), 1287.2 (16.6), 1288.3 (13.6), 1288.9 (14.9), 1291.6 (15.1), 1292.9 (15.6), 1294.2 (17.8), 1505.7 (18.8), 1506.7 (18.8), 1506.8 (15.8), 1512.5 (17.4), 1512.8 (15.6), 1513.7 (13.8), 2872.8 (13.9), 2872.9 (13.8), 2873.2 (3.9), 3044.2 (0.7), 3044.3 (0.7), 3044.5 (0.2), 3066.1 (0.0), 3066.2 (0.0), 3066.4 (0.1), 3128.5 (0.3), 3128.7 (0.3), 3128.8 (0.3)			

Fe ⁺ (CH ₄) ₄					
Multiplicity	E(no ZPE, Hartree)	E(w/ZPE, Hartree)			
12	-5217.050765	-5216.867692	Fe 1.026206	0.610681	-0.7943
			Fe -0.610551	1.026321	0.794257
			Fe 0.610807	-1.02635	0.794003
			Fe -1.026499	-0.610684	-0.79398
			C -1.066289	2.972689	2.066838
			H -0.021484	2.758149	2.322618
			H -1.178814	3.242269	1.007256
			H -1.38366	3.836054	2.651702
			H -1.735121	2.146458	2.355197
			H 3.242145	1.179123	-1.00763
			C 2.972367	1.066623	-2.06716
			H 3.835603	1.384008	-2.6522
			H 2.757802	0.021817	-2.32292
			H 2.146071	1.735447	-2.35534
			H -2.760081	-0.021141	-2.32048
			C -2.973036	-1.066648	-2.06628
			H -2.146144	-1.733894	-2.3564
			H -3.241623	-1.18129	-1.00667
			H -3.836454	-1.384197	-2.65096
			H 0.021944	-2.758845	2.321882
			C 1.067052	-2.97258	2.066651
			H 1.180379	-3.241837	1.007072
			H 1.735135	-2.145935	2.355586
			H 1.384702	-3.835856	2.651493
					
Frequency (Intensity) 35.1 (2.6), 35.1 (0.0), 38.5 (0.1), 39.1 (3.1), 39.1 (3.1), 57.5 (0.0), 57.5 (0.0), 60.3 (0.0), 62.4 (0.0), 64.2 (0.0), 64.4 (0.0), 65.4 (0.0), 110.1 (0.8), 142.6 (0.0), 147.1 (1.1), 147.1 (1.1), 161.3 (0.0), 169.2 (2.5), 192.2 (6.7), 208.1 (1.5), 208.1 (1.5), 213.8 (3.4), 216.8 (0.0), 218.9 (15.9), 218.9 (15.9), 260.1 (0.0), 260.5 (0.8), 260.5 (0.8), 262.9 (1.8), 280.7 (0.0), 1246.6 (84.6), 1246.8 (99.7), 1246.8 (99.7), 1252.0 (0.0), 1289.5 (3.1), 1289.5 (20.2), 1289.5 (17.8), 1289.9 (14.3), 1294.6 (0.1), 1294.6 (18.4), 1294.7 (18.5), 1294.8 (34.7), 1506.8 (23.8), 1506.8 (23.8), 1507.0 (14.6), 1507.5 (0.0), 1516.8 (17.7), 1516.8 (17.6), 1517.0 (0.1), 1517.1 (23.8), 2887.5 (19.2), 2887.6 (19.2), 2888.1 (17.9), 2888.4 (0.0), 3057.1 (0.2), 3057.2 (0.3), 3057.2 (0.3), 3057.2 (0.2), 3083.6 (0.1), 3083.6 (0.0), 3083.6 (0.4), 3083.6 (0.4), 3130.5 (0.3), 3130.5 (0.3), 3130.5 (0.3), 3130.6 (0.0)					

APPENDIX B

COMPARISON OF B3LYP SIMULATIONS WITH AND WITHOUT EMPIRICAL DISPERSION FOR MONOLAYER COMPLEXES CALCULATED AT THE M11L/6-311++G(3df,3pd) LEVEL

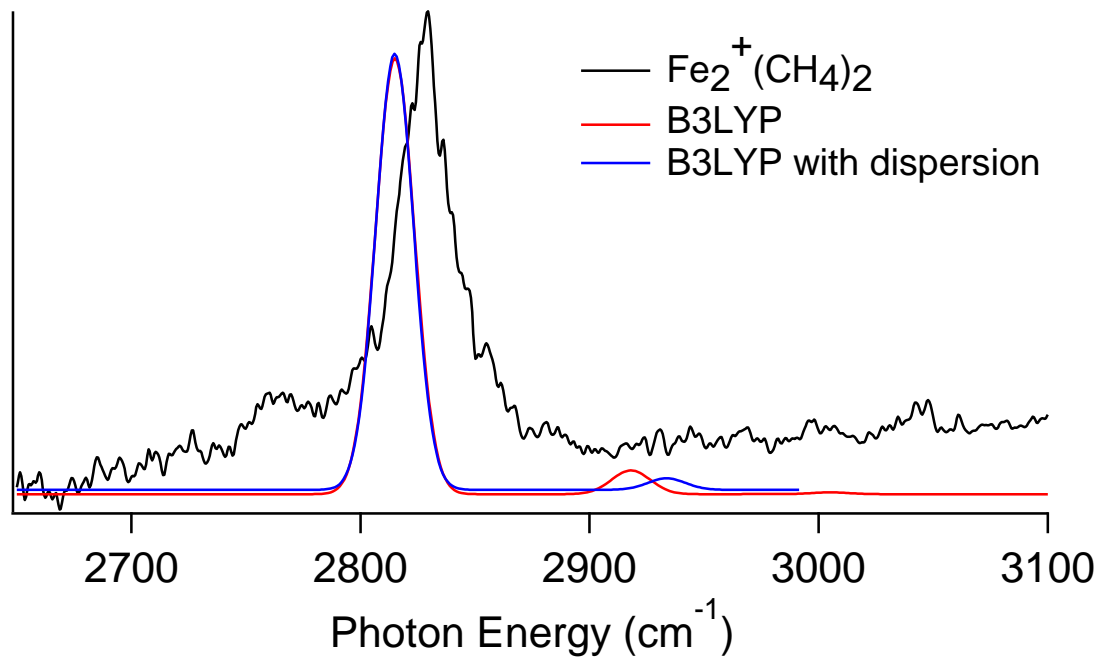


Figure B.1 Experimental IR photodissociation spectrum of $\text{Fe}_2^+(\text{CH}_4)_2$ along with simulated spectra using B3LYP and B3LYP-GD3 and 6-311++G(3df,3pd) basis set.

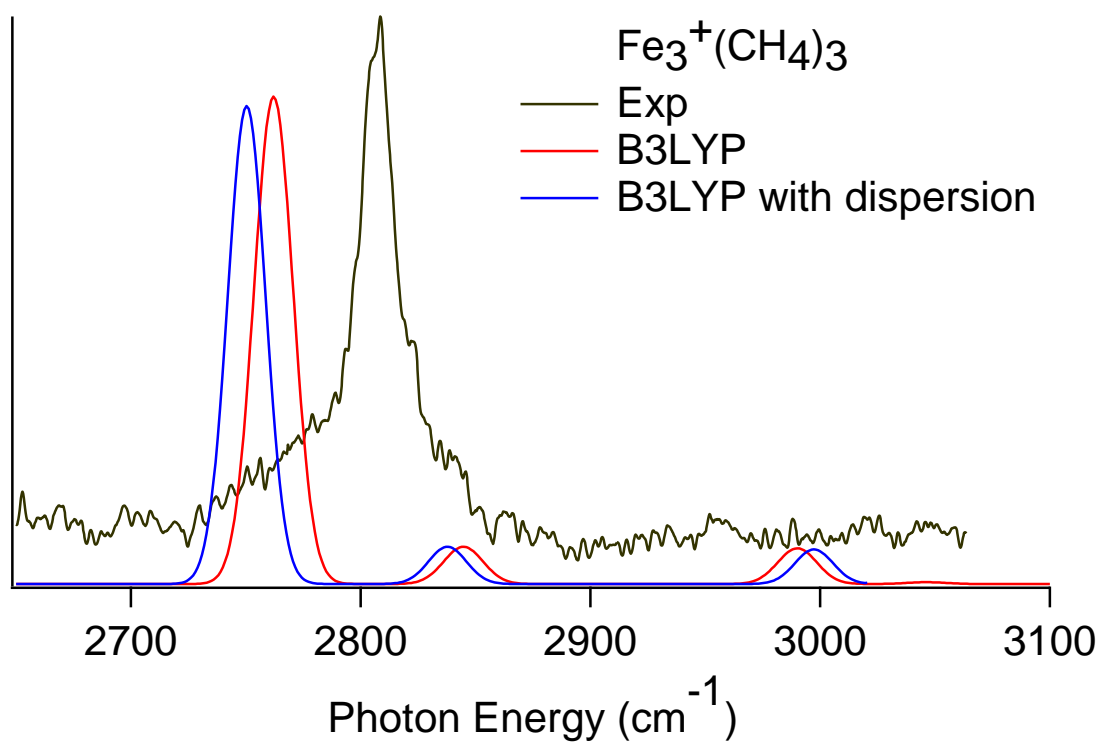


Figure B.2 Experimental IR photodissociation spectrum of $\text{Fe}_3^+(\text{CH}_4)_3$ along with simulated spectra using B3LYP and B3LYP-GD3 and 6-311++G(3df,3pd) basis set.

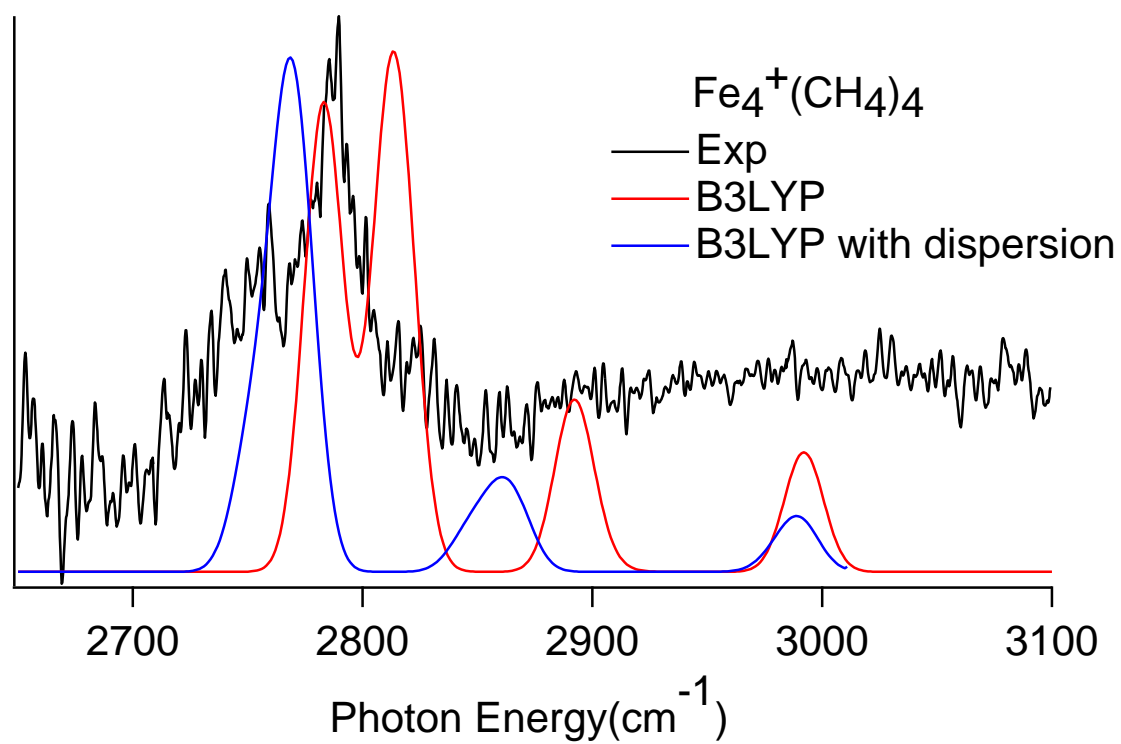


Figure B.3 Experimental IR photodissociation spectrum of $\text{Fe}_4^+(\text{CH}_4)_4$ along with simulated spectra using B3LYP and B3LYP-GD3 and 6-311++G(3df,3pd) basis set.

BIBLIOGRAPHY

- Abate, Y.; Kleiber, P. D. *J. Chem. Phys.* **2005**, *122*, 084305.
- Aguirre, F.; Husband, J.; Thompson, C. J.; Stringer, K. L.; Metz, R. B. *J. Chem. Phys.* **2003**, *119*, 10194-10201.
- Albert, G.; Berg, C.; Beyer, M.; Achatz, U.; Joos, S.; Niedner-Schatteburg, G.; Bondybey, V. E. *Chem. Phys. Lett.* **1997**, *268*, 235-241.
- Altinay, G.; Citir, M.; Metz, R. B. *J. Phys. Chem. A* **2010**, *114*, 5104-5112.
- Altinay, G.; Metz, R. B. *J. Am. Soc. Mass Spectrom.* **2010**, *21*, 750-757.
- Alvarez-Galvan, M. C.; Mota, N.; Ojeda, M.; Rojas, S.; Navarro, R. M.; Fierro, J. L. G. *Catal. Today* **2011**, *171*, 15-23.
- Armentrout, P. B. *Catal. Sci. Tech.* **2014**, *4*, 2741-2755.
- Ashraf, M. A.; Copeland, C. W.; Kocak, A.; McEnroe, A. R.; Metz, R. B. *Phys. Chem. Chem. Phys.* **2015**, *17*, 25700-25704.
- Bandyopadhyay, B.; Duncan, M. A. *Chem. Phys. Lett.* **2012**, *530*, 10-15.
- Bandyopadhyay, B.; Reishus, K. N.; Duncan, M. A. *J. Chem. Phys. A* **2013**, *117*, 7794-7803.
- Beyer, M. K. *Mass Spectrom. Rev.* **2007**, *26*, 517-541.
- Brown, J. M.; Sears, T. J. *J. Mol. Spectrosc.* **1979**, *75*, 111-133.
- Carnegie, P. D.; Bandyopadhyay, B.; Duncan, M. A. *J. Phys. Chem. A* **2008**, *112*, 6237-6243.
- Carnegie, P. D.; Bandyopadhyay, B.; Duncan, M. A. *J. Phys. Chem. A* **2011**, *115*, 7602-7609.
- Carnegie, P. D.; Bandyopadhyay, B.; Duncan, M. A. *J. Chem. Phys.* **2011**, *134*, 014302.
- Carnegie, P. D.; McCoy, A. B.; Duncan, M. A. *J. Phys. Chem. A* **2009**, *113*, 4849-4854.
- Castro, M. *Chem. Phys. Lett.* **2007**, *446*, 333-338.
- Chen, Y. M.; Armentrout, P. B. *J. Phys. Chem.* **1995**, *99*, 10775-10779.
- Chiodo, S.; Rivalta, I.; Michelini, M.; Russo, N.; Sicilia, E.; Ugalde, J. M. *J. Phys. Chem. A* **2006**, *110*, 12501-12511.
- Chrétien, S.; Salahub, D. R. *J. Chem. Phys.* **2003**, *119*, 12279-12290.
- Chrétien, S.; Salahub, D. R. *J. Chem. Phys.* **2003**, *119*, 12291-12300.
- Citir, M.; Altinay, G.; Austein-Miller, G.; Metz, R. B. *J. Phys. Chem. A* **2010**, *114*, 11322-11329.
- Citir, M.; Altinay, G.; Metz, R. B. *J. Phys. Chem. A* **2006**, *110*, 5051-5057.

- Citir, M.; Liu, F.; Armentrout, P. B. *J. Chem. Phys.* **2009**, *130*, 054309-16.
- Copeland, C. W.; Ashraf, M. A.; Boyle, E. M.; Metz, R. B. *J. Phys. Chem. A* **2017**, *121*, 2132-2137.
- Corcelli, S. A.; Kelley, J. A.; Tully, J. C.; Johnson, M. A. *J. Phys. Chem. A* **2002**, *106*, 4872-4879.
- Dalleska, N. F.; Honma, K.; Sunderlin, L. S.; Armentrout, P. B. *J. Am. Chem. Soc.* **1994**, *116*, 3519-3528.
- Daluz, J. S.; Kocak, A.; Metz, R. B. *J. Phys. Chem. A* **2012**, *116*, 1344-1352.
- DiLabio, G.; Otero-de-la-Roza, A. *Rev. Comp. Ch.* Parrill, A.; Lipkowitz, K., Eds. John Wiley & Sons, Inc.: Hoboken, NJ, 2016; Vol. 29, pp 1-97.
- Donnelly, S. G.; Schmuttenmaer, C. A.; Qian, J.; Farrar, J. M. *J. Chem. Soc.-Faraday Trans.* **1993**, *89*, 1457-1465.
- Dryza, V.; Bieske, E. J. *Int. J. Mass Spectrom.* **2010**, *297*, 46-54.
- Duncan, M. A. *Int. J. Mass Spectrom.* **2000**, *200*, 545-569.
- Duncan, M. A. *Int. Rev. Phys. Chem.* **2003**, *22*, 407-435.
- Frisch, M. J.; Trucks, G. W.; Schlegel, H. B.; Scuseria, G. E.; Robb, M. A.; Cheeseman, J. R.; Scalmani, G.; Barone, V.; Mennucci, B.; Petersson, G. A.; Nakatsuji, H.; Caricato, M.; Li, X.; Hratchian, H. P.; Izmaylov, A. F.; Bloino, J.; Zheng, G.; Sonnenberg, J. L.; Hada, M.; Ehara, M.; Toyota, K.; Fukuda, R.; Hasegawa, J.; Ishida, M.; Nakajima, T.; Honda, Y.; Kitao, O.; Nakai, H.; Vreven, T.; Montgomery Jr., J. A.; Peralta, J. E.; Ogliaro, F.; Bearpark, M.; Heyd, J. J.; Brothers, E.; Kudin, K. N.; Staroverov, V. N.; Keith, T.; Kobayashi, R.; Normand, J.; Raghavachari, K.; Rendell, A.; Burant, J. C.; Iyengar, S. S.; Tomasi, J.; Cossi, M.; Rega, N.; Millam, J. M.; Klene, M.; Knox, J. E.; Cross, J. B.; Bakken, V.; Adamo, C.; Jaramillo, J.; Gomperts, R.; Stratmann, R. E.; Yazyev, O.; Austin, A. J.; Cammi, R.; Pomelli, C.; Ochterski, J. W.; Martin, R. L.; Morokuma, K.; Zakrzewski, V. G.; Voth, G. A.; Salvador, P.; Dannenberg, J. J.; Dapprich, S.; Daniels, A. D.; Farkas, O.; Foresman, J. B.; Ortiz, J. V.; Cioslowski, J.; Fox, D. J. *Gaussian 09, Revision D.01*, Gaussian, Inc., Wallingford, CT: Pittsburgh PA, 2013.
- Furukawa, K.; Ohashi, K.; Koga, N.; Imamura, T.; Judai, K.; Nishi, N.; Sekiya, H. *Chem. Phys. Lett.* **2011**, *508*, 202-206.
- Gallagher, J. W.; Brion, C. E.; Samson, J. A. R.; Langhoff, P. W. *Journal of Physical and Chemical Reference Data* **1988**, *17*, 9-153.
- Gehret, O.; Irion, M. P. *Chem. Phys. Lett.* **1996**, *254*, 379-383.
- Grimme, S.; Antony, J.; Ehrlich, S.; Krieg, H. *The Journal of Chemical Physics* **2010**, *132*, 154104.
- Gutsev, G. L.; Bauschlicher, C. W., Jr. *J. Phys. Chem. A* **2003**, *107*, 7013-7023.
- Gutsev, G. L.; Weatherford, C. A.; Jena, P.; Johnson, E.; Ramachandran, B. R. *J. Phys. Chem. A* **2012**, *116*, 10218-10228.

Harding, D. J.; Kerpel, C.; Meijer, G.; Fielicke, A. *Angew. Chem. Int. Ed.* **2012**, *51*, 817-819.

Hofstetter, T. E.; Armentrout, P. B. *J. Chem. Phys. A* **2013**, *117*, 1110-1123.

Husband, J.; Aguirre, F.; Ferguson, P.; Metz, R. B. *J. Chem. Phys.* **1999**, *111*, 1433-1437.

Husband, J.; Aguirre, F.; Thompson, C. J.; Metz, R. B. *Chem. Phys. Lett.* **2001**, *342*, 75-84.

Ichihashi, M.; Hanmura, T.; Kondow, T. *J. Chem. Phys.* **2006**, *125*, 133404.

III, W. L. P.; Copeland, C.; Kocak, A.; Sallese, Z.; Metz, R. B. *J. Chem. Phys.* **2014**, *141*, 204305.

Iino, T.; Ohashi, K.; Inoue, K.; Judai, K.; Nishi, N.; Sekiya, H. *J. Chem. Phys.* **2007**, *126*, 11.

Irigoras, A.; Fowler, J. E.; Ugalde, J. M. *J. Am. Chem. Soc.* **1999**, *121*, 8549-8558.

Irikura, K. K.; Beauchamp, J. L. *J. Phys. Chem.* **1991**, *95*, 8344-8351.

Ishikawa, H.; Nakano, T.; Eguchi, T.; Shibukawa, T.; Fuke, K. *Chem. Phys. Lett.* **2011**, *514*, 234-238.

Kocak, A. Ph.D., University of Massachusetts. 2014.

Kocak, A.; Ashraf, M. A.; Metz, R. B. *J. Phys. Chem. A* **2015**, *119*, 9653-9665.

Kocak, A.; Geoff, A.; Pearson III, W.; Altinay, G.; Metz, R. *J. Phys. Chem. A* **2013**, *117*, 1254-1264

Kocak, A.; Sallese, Z.; Johnston, M. D.; Metz, R. B. *J. Phys. Chem. A* **2014**, *118*, 3253-3265.

Kramida, A.; Ralchenko, Y.; Reader, J.; NIST ASD Team, National Institute of Standards and Technology: Gaithersburg, MD, 2012.

Kummerlowe, G.; Balteanu, I.; Sun, Z.; Balaj, O. P.; Bondybey, V. E.; Beyer, M. K. *Int. J. Mass Spectrom.* **2006**, *254*, 183-188.

Lang, S. M.; Bernhardt, T. M.; Barnett, R. N.; Landman, U. *Angew. Chem. Int. Ed.* **2010**, *49*, 980-983.

Lang, S. M.; Bernhardt, T. M.; Barnett, R. N.; Landman, U. *ChemPhysChem* **2010**, *11*, 1570-1577.

Lang, S. M.; Bernhardt, T. M.; Barnett, R. N.; Landman, U. *J. Phys. Chem. C* **2011**, *115*, 6788-6795.

Lessen, D. E.; Asher, R. L.; Brucat, P. J. *J. Chem. Phys.* **1990**, *93*, 6102-6103.

Li, Y. Z.; Wang, G. J.; Wang, C. X.; Zhou, M. F. *J. Phys. Chem. A* **2012**, *116*, 10793-10801.

Liu, F. Y.; Zhang, X. G.; Liyanage, R.; Armentrout, P. B. *J. Chem. Phys.* **2004**, *121*, 10976-10990.

Liyanage, R.; Zhang, X.-G.; Armentrout, P. B. *J. Chem. Phys.* **2001**, *115*, 9747-9763.

Magnera, T. F.; David, D. E.; Michl, J. *J. Am. Chem. Soc.* **1989**, *111*, 4100-4101.

Marinelli, P. J.; Squires, R. R. *J. Am. Chem. Soc.* **1989**, *111*, 4101-4103.

- Metz, R. B. *Int. Rev. Phys. Chem.* **2004**, *23*, 79-108.
- Metz, R. B. *Adv. Chem. Phys.* **2008**, *138*, 331-373.
- Misaizu, F.; Sanekata, M.; Tsukamoto, K.; Fuke, K.; Iwata, S. *J. Phys. Chem.* **1992**, *96*, 8259-8264.
- Mosley, J. D.; Cheng, T. C.; Hasbrouck, S. D.; Ricks, A. M.; Duncan, M. A. *J. Chem. Phys.* **2011**, *135*, 104309-6.
- O'Brien, J. T.; Williams, E. R. *J. Phys. Chem. A* **2011**, *115*, 14612-14619.
- O'Hair, R. A. J. *Int. J. Mass Spectrom.* **2015**, *377*, 121-129.
- Okumura, M.; Yeh, L. I.; Meyers, J. D.; Lee, Y. T. *J. Chem. Phys.* **1986**, *85*, 2328-2329.
- Peverati, R.; Truhlar, D. G. *J. Phys. Chem. Lett.* **2012**, *3*, 117-124.
- Pickett, H. M. *J. Mol. Spectrosc.* **1991**, *148*, 371-377.
- Poad, B. L. J.; Thompson, C. D.; Bieske, E. J. *Chem. Phys.* **2008**, *346*, 176-181.
- Proch, D.; Trickl, T. *Rev. Sci. Instrum.* **1989**, *60*, 713-716.
- Rodriguez, O.; Lisy, J. M. *Chem. Phys. Lett.* **2011**, *502*, 145-149.
- Roithova, J. *Chem. Soc. Rev.* **2012**, *41*, 547-559.
- Roithova, J.; Schröder, D. *Chem. Rev.* **2010**, *110*, 1170-1211.
- Rosenwaks, S. Roy. Soc. Ch.: Cambridge, UK, 2009; p 204.
- Rosi, M.; Bauschlicher, C. W., Jr. *J. Chem. Phys.* **1989**, *90*, 7264-7272.
- Rothman, L. S.; Jacquemart, D.; Barbe, A.; Benner, D. C.; Birk, M.; Brown, L. R.; Carleer, M. R.; Chackerian, C.; Chance, K.; Coudert, L. H.; Dana, V.; Devi, V. M.; Flaud, J. M.; Gamache, R. R.; Goldman, A.; Hartmann, J. M.; Jucks, K. W.; Maki, A. G.; Mandin, J. Y.; Massie, S. T.; Orphal, J.; Perrin, A.; Rinsland, C. P.; Smith, M. A. H.; Tennyson, J.; Tolchenov, R. N.; Toth, R. A.; Vander Auwera, J.; Varanasi, P.; Wagner, G. *J. Quant. Spec. Radiat. Transfer* **2005**, *96*, 139-204.
- Sasaki, J.; Ohashi, K.; Inoue, K.; Imamura, T.; Judai, K.; Nishi, N.; Sekiya, H. *Chem. Phys. Lett.* **2009**, *474*, 36-40.
- Scharfschwerdt, B.; van der Linde, C.; Balaj, O. P.; Herber, I.; Schutze, D.; Beyer, M. K. *Low Temp. Phys.* **2012**, *38*, 717-722.
- Schlangen, M.; Schwarz, H. *Catal. Lett.* **2012**, *142*, 1265-1278.
- Schnabel, P.; Irion, M. P. *Ber. Bunsen-Ges. Phys. Chem. Chem. Phys.* **1992**, *96*, 1101-1103.
- Schnabel, P.; Irion, M. P.; Weil, K. G. *J. Phys. Chem.* **1991**, *95*, 9688-9694.

Schröder, D.; Schwarz, H.; Hrusák, J.; Pyykkö, P. *Inorg. Chem.* **1998**, *37*, 624-632.

Schwarz, H. *Angew. Chem. Int. Ed. Engl.* **1991**, *30*, 820-821.

Schwarz, H. *Angew. Chem. Intl. Ed.* **2011**, *50*, 10096-10115.

Schwarz, H. *Isr. J. Chem.* **2014**, *54*, 1413-1431.

Scurlock, C. T.; Pullins, S. H.; Reddic, J. E.; Duncan, M. A. *J. Chem. Phys.* **1996**, *104*, 4591-4599.

Shayesteh, A.; Lavrov, V. V.; Koyanagi, G. K.; Bohme, D. K. *J. Phys. Chem. A* **2009**, *113*, 5602-5611.

Stoermer, C. W.; Gilb, S.; Friedrich, J.; Schooss, D.; Kappes, M. M. *Rev. Sci. Instrum.* **1998**, *69*, 1661-1664.

Stone, J. A.; Vukomanovic, D. *Int. J. Mass Spectrom.* **1999**, *185*, 227-229.

Tarczay, G.; Gopalakrishnan, S.; Miller, T. A. *J. Mol. Spectrosc.* **2003**, *220*, 276-290.

Tonkyn, R.; Ronan, M.; Weisshaar, J. C. *J. Phys. Chem.* **1988**, *92*, 92.

Trachtman, M.; Markham, G. D.; Glusker, J. P.; George, P.; Bock, C. W. *Inorg. Chem.* **1998**, *37*, 4421-4431.

van der Linde, C.; Beyer, M. K. *J. Phys. Chem. A* **2012**, *116*, 10676-10682.

Vlasak, P. R.; Beussman, D. J.; Davenport, M. R.; Enke, C. G. *Rev. Sci. Instrum.* **1996**, *67*, 68-72.

Vučković, S.; Svanqvist, M.; Popok, V. N. *Rev. Sci. Instrum.* **2008**, *79*, 073303.

Walker, N. R.; Walters, R. S.; Pillai, E. D.; Duncan, M. A. *J. Chem. Phys.* **2003**, *119*, 10471-10474.

Waller, S. E.; Mann, J. E.; Jarrold, C. C. *J. Phys. Chem. A* **2013**, *117*, 1765-1772.

Walters, R. S.; Duncan, M. A. *Aust. J. Chem.* **2004**, *57*, 1145-1148.

Walters, R. S.; Pillai, E. D.; Duncan, M. A. *J. Am. Chem. Soc.* **2005**, *127*, 16599-16610.

Ward, T. B.; Carnegie, P. D.; Duncan, M. A. *Chem. Phys. Lett.* **2016**, *654*, 1-5.

Watanabe, H.; Iwata, S.; Hashimoto, K.; Misaizu, F.; Fuke, K. *J. Am. Chem. Soc.* **1995**, *117*, 755-763.

Weis, P.; Kemper, P. R.; Bowers, M. T. *J. Phys. Chem. A* **1997**, *101*, 2809-2816.

Wheeler, O. W.; Salem, M.; Gao, A.; Bakker, J. M.; Armentrout, P. B. *J. Phys. Chem. A* **2016**, *120*, 6216-6227.

Whitham, C. J.; Jungen, C. *J. Chem. Phys.* **1990**, *93*, 1001-1008.

Wiley, W. C.; McLaren, I. H. *Rev. Sci. Instrum.* **1955**, *26*, 1150-1157.

Willey, K. F.; Yeh, C. S.; Robbins, D. L.; Pilgrim, J. S.; Duncan, M. A. *J. Chem. Phys.* **1992**, *97*, 8886-8895.

Zhu, X.; Nur, A. H.; Misra, P. *J. Quant. Spectrosc. Rad. Trans.* **1994**, *52*, 167-177.